Nanoparticles Based MIL-100(Fe) MOFs Composites for Loading and Release of Doxorubicin Hydrochloride

Abhik Bhattacharjee

Nanoparticles Based MIL-100(Fe) MOFs Composites for Loading and Release of Doxorubicin Hydrochloride

Thesis submitted in partial fulfillment of the requirement for the degree of

Doctor of Philosophy

By

Abhik Bhattacharjee

Roll No.: 126107019

Department of Chemical Engineering

Indian Institute of Technology Guwahati, Assam 781039

March 2021

Dedicated to my Parents and the Almighty. Their Uncountable Blessings and Support has Helped Me to be the Better Person that I am Today.

Department of Chemical Engineering
Indian Institute of Technology Guwahati
Guwahati 781039, India

CERTIFICATE

It is certified that the work contained in the thesis entitled "**Nanoparticles based MIL-100(Fe) MOFs composites for loading and release of doxorubicin hydrochloride**", submitted by **Mr. Abhik Bhattacharjee**, has been carried out under our supervision. The work documented in this thesis has not been submitted to any other University or Institute for the award of any degree or diploma.

Dr. Mihir Kumar Purkait
Professor
Department of Chemical Engineering
Indian Institute of Technology Guwahati
Guwahati 781039 (India)
Date : 15th March 2021

Dr. Sasidhar Gumma
Professor
Department of Chemical Engineering
Indian Institute of Technology Tirupati
Tirupati 517506 (India)
Date : 15th March 2021

Acknowledgements

It is my great pleasure to thank each and every one who helped directly or indirectly to complete my research work and made this thesis possible. I owe my deepest gratitude to all of them.

I would first like to acknowledge my supervisors Prof. Sasidhar Gumma (IIT Tirupati) and Prof. Mihir Kumar Purkait for their immense guidance throughout the research work. I am thankful for their encouragement, patience towards research and support, which enabled me to develop a better understanding of the subject leading to the present thesis. I would also like to acknowledge my sincere gratitude to my doctoral committee members, Prof. G. Pugazhenthi, Prof. Vaibhav V. Goud and Prof. Tharmalingam Punniyamurthy (Department of Chemistry), for their advice and suggestions throughout my research work.

I am also thankful to Prof. Bishnupada Mandal and Prof. Prabirkumar Saha for providing me the lab facilities during this research work. My sincere thanks go to the faculty members of Department of Chemical Engineering, IIT Guwahati, for their continuous suggestions and inspirations.

I would also like to extend my sincere gratitude to the technical officers of my Department specially, Mrs. Ritumoni Kalita, Mr. Harsaraj Biswanath and Mr. Pankaj Kumar, senior technical superintendent Dr. Lukumoni Borah and Mr. Dipak K. Barman, technical superintendent Dr. Kaustavmoni Deka, Mr. Debajit Borah, Mr. Jayanta K. Mout, Mr. Prasun K. Bhattacharjee, junior technical superintendents Mr. Balen C. Mahanta, Mr. Pankaj S. Baruah, Mr. Ariful Hoque and Mr. Saiful Alam, junior technician Mr. Wasim Akram, Ms. Jyoti K. Mahato and the office staff, Mr. Sailen Das, Mr. Deep J. Sinha and Mr. Bhagya Boro. The experimental works presented in this thesis as well as all the official paper work would never have been possible without the help of these proficient technicians.

Acknowledgements

I would like to thank the Central Instruments Facility and Analytical Lab Facility, Department of Chemical Engineering of IIT Guwahati for providing the facilities to carry out BET, TGA, FTIR, FESEM, FETEM, UV spectroscopy, Delsa Nano and XRD analysis. I am thankful to

I would also like to thank the Department of Physics, IIT Guwahati to carry out XRD analysis during the early stages of this research work.

I am thankful to my seniors and lab mates Dr. Prashant Mishra, Dr. Debjyoti Sahu, Dr. L. Shravanti, Dr. Rupak Kishor, Dr. Manish Sinha, Dr. Vikrant Volli, Dr. Satyannarayana Edubilli, Dr. Pradip Das, Dr. Murchana Changmai, Dr. Randeep Singh, Dr. Dibyajyoti Haldar, Mr. Ramesh Tellagorla, Mr. Prudhviraj Medikonda, Mr. Piyal Mandal, Mr. Pranjal Pratim Das, Mr. Ankush Sontakke, Mrs. Deepti Nair, Mr. Anweshan, Ms. Baite, Mr. Prangan Duarah and Mr. Mukesh Sharma.

I cannot forget to thank my friends and batch mates here at IITG: Dr. Supriyo Kumar Mandal, Dr. Himadri Sahu, Dr. Rahul Ramteke, Dr. Saptak Rarotra, Dr. Amit Badghare, Dr. Rahul Patwa, Dr. Prodyut Dhar, Dr. Suman Saha, Dr.Bhsakar Medhi, Dr. Jay Bhasarkar, Dr. Sankar Chakma, Dr. Debashis Kundu, Dr. Abir Ghosh, Dr. Mitradip Bhattacharjee, Dr. K. Suresh, Dr. Manish Kamal, Dr. Kishant Kumar, Dr. Babul Prasad, Dr. Rajashree Borgohain, Dr. Sohanbir Singh, Dr. Shailesh Varade, Mr. Jitendra Rawat, Mr. Atanu Paul, Mr. Abhradip Pal and Mrs. Soumi Sarkar for their support in making my stay at IIT Guwahati memorable.

I am grateful to Mrs. Pallabita B. Chodhury and Dr. M. Chakraborty for their valuable suggestions during my hard time in IIT Guwahati.

Last but not the least; I would like to thank my father Mr. Nirmalendu Bhattacharjee and my mother Mrs. Tulsi Bhattacharjee for supporting me to do my Ph.D. My parents have been a moral support during my emotional breakdowns and I could not thank God enough for

bestowing me with such a supportive family. Their love, affection, blessings and sacrifices made me stronger to overcome my huddles and achieve my target.

Abhik Bhattacharjee

Abstract

The major challenges in the drug delivery system (DDS) is the controlled release of desired drugs to targeted location by responding to the external/environmental stimulus. Porous materials based DDSs have got more attentions in recent times owing to their high surface area, large pore volume and tunable pore size. Metal organic frameworks (MOFs), a new class of porous material that are being widely investigated for drug delivery applications. This thesis focusses on the synthesis of iron based metal organic framework (MOF) MIL-100(Fe) and its composites with Iron oxide (Fe_3O_4), Zinc oxide (ZnO) and Cerium oxide (CeO_2) nanoparticles. Doxorubicin hydrochloride (DOX) was considered as an anticancer drug for the present study. MIL-100(Fe) were synthesized with the addition of HF and without HF acid. It was observed that HF played an important role in synthesis procedure of MIL-100(Fe). HF significantly affected its porosity and thereby its drug loading capacity. MIL-100(Fe) prepared without HF as the mineralizing agent yielded MOF with higher mesopore volume. In addition, DOX loading capacity was the highest (~ 234 mg/g) for MIL-100 possess maximum mesopore volume among pure MOFs.

Composites of Fe_3O_4 and MIL-100(Fe) were synthesized by adding different amount of nanoparticles to the solvent mixture used for synthesis of the MIL-100. The composites were further characterized by various techniques like BET, XRD, TEM, FESEM, VSM (for magnetic particles) and TGA etc. The presence of Fe_3O_4 NPs enhanced the DOX loading capacity initially; when the MIL-100 possesses lower mesopore volume. This enhancement was more than 76% and 81% as compare to pure Fe_3O_4 and MIL-100(Fe), respectively. However, the

loading capacity was decreased after an optimal point with further addition of NPs as MOFs pores might be blocked due to agglomerated NPs.

ZnO@MIL-100(Fe) composites were synthesized in presence and in absence of HF, respectively. ZnO nanoparticles enhanced the drug loading capacity in HF route of composite synthesis. The maximum DOX loading was found as 189 mg/g. Similar DOX loading pattern was observed for Fe_3O_4@MIL-100(Fe) composites; although both the NPs were different in physically and chemically. In case of composites synthesis in absence of HF (contain higher mesopore volume in pure MOF), inclusion of nanoparticles decreased the drug loading capacity. The nanoparticles in the mesopores possibly block its adsorption sites, which resulted in a net decrease in DOX loading capacity.

The size and morphology of the CeO_2 nanoparticles were reformed during composite synthesis in presence of HF. Thus, no further enhancement in DOX loading capacity was observed. This was possibly due to blocking of pores by newly shaped particles. The size and physical shape of CeO_2 was intact in absence of HF during CeO_2@MIL-100 composite synthesis. However, DOX loading capacity was not increased in this case also due to possible blockage of adsorption sites in mesopores. In overall, no further improvement in DOX loading capacity was seen in case of CeO_2@MIL-100(Fe) composites by either of two routes. The DOX released patterns form all the MOFs and its composites were highly controlled and sustained over 20 days.

Research Publications

Published

1. **A. Bhattacharjee**, S. Gumma and M.K. Purkait, "Fe_3O_4 promoted metal organic framework MIL-100(Fe) for the controlled release of doxorubicin hydrochloride" Microporous and Mesoporous Materials 259 (2018) 203-210.
2. **A. Bhattacharjee**, M.K. Purkait and S. Gumma "Doxorubicin loading capacity of MIL-100(Fe): Effect of synthesis conditions" Journal of Inorganic and Organometallic Polymers and Materials 30 (2020) 2366-2375.
3. **A. Bhattacharjee**, M.K. Purkait and S. Gumma, "Loading and release of doxorubicin hydrochloride from iron(III) trimesate MOF and zinc oxide nanoparticle composites" Dalton Transactions 49 (2020) 8755-8763.

Conferences/ Seminars or workshops

1. A. Bhattacharjee and S. Gumma, "Porous materials as a potential carrier for drug delivery" 68th Annual Session of Indian Institute of Chemical Engineers (**CHEMCON-2015)**, 27 -30 December 2015, **Indian Institute of Technology Guwahati**.
2. A. Bhattacharjee and S. Gumma, "Fe_3O_4 promoted metal organic framework MIL-100(Fe): Can be a promising candidate as a drug carrier" National Workshop on Advanced Probing Techniques in TEM **(APTTEM-2016)**, 15-16 February 2016, **Indian Institute of Technology Guwahati.**

3. A. Bhattacharjee and S. Gumma, "Synthesis of Fe_3O_4 promoted MIL-100 (Fe) for drug delivery", 3rd International Symposium on Advances in Sustainable Polymers **(ASP-16)**, 4-6 August 2016, **Kyoto Institute of Technology Japan.**

4. A. Bhattacharjee and S. Gumma, "Fe_3O_4 promoted metal organic framework MIL-100(Fe): Can be a promising candidate as a drug carrier", **16 AIChE Annual Meeting**, 13-18 November 2016, **San Francisco**, **USA.**

5. A. Bhattacharjee and S. Gumma, "Synthesis of Fe_3O_4@MIL-100 composites by 'layer-by-layer' strategy for drug delivery" **7**th National Level Annual Research symposium of Chemical Engineering Research Scholars **(ChEmference 2016)**, 3-4 December 2016, **Indian Institute of Technology Gandhinagar**.

6. A. Bhattacharjee, S. Gumma and M.K. Purkait, "Magnetic nanomaterial based porous materials for doxorubicin delivery" International Conference on Emerging Trends in Nanomaterials Science and Technology **(ICETNMST-2017)**, 4-6 January 2017, **National Institute of Technology Nagaland**.

7. A. Bhattacharjee, S. Gumma and M.K. Purkait, "Synthesis of Fe_3O_4 @MIL-100 composites" International Conference on Sophisticated Instruments in Modern Research (**ICSIMR-2017)**, 27-30 December 2017, **Indian Institute of Technology Guwahati.**

8. A. Bhattacharjee, S. Gumma and M.K. Purkait, "Metal oxide promoted porous materials for drug delivery" **Research Conclave'18**, 8-11 March 2018, **Indian Institute of Technology Guwahati.**

CONTENTS

CONTENTS

CONTENTS

LIST OF FIGURES

LIST OF TABLES

Nomenclature

Notations

a_m	Surface coverage by molecule
A	Absorbance
c	Concentration of absorbing molecule in Beer-Lambart law
C	BET constant
d	Inter planer spacing
E	Heat of adsorption
F	Fe_3O_4 particles
H	Magnetic field
I	Intensity of transmitted light
I_0	Intensity of incident light
L	Path length
m_{ads}	Mass of dried carrier
m_f	Mass of DOX in final supernatant
m_0	Initial amount of DOX
m_r	Specific DOX released in PBS
MF	First variant of MIL-100 prepared with HF
MNF1	Second variant of MIL-100 prepared without HF
MNF2	Third variant of MIL-100 prepared without HF
n	Order of diffraction
N_a	Avogadro's number
P	Equilibrium pressure
P_0	Saturation pressure
q	Drug loading capacity

q_{mix}	Drug loading capacity of the physical mixture
q_{MOF}	Drug loading capacity of pure MIL-100(Fe)
q_{ZnO}	Drug loading capacity of pure ZnO
q'	Specific drug release capacity of the carrier
S_{BET}	Surface area calculated by BET method
S_{EXT}	External surface area
t	Statistical film thickness
V	Volume of gas adsorbed at STP
V_m	Monolayer adsorbed quantity
V_{meso}	Mesopore volume
V_{micro}	Micropore volume
V_t	Total pore volume
x	Mass fraction of nanoparticles
Z	ZnO particles
σ	Film thickness of one layer
ε	Molar absorptivity
λ	Wavelength of X-ray beam
θ	Angle between incident beam and the crystallographic plane

Abbreviations

BET	Brunauer–Emmett–Teller
BDC	Benezene-1,4-dicarboxylic acid
BSA	Bovine serum albumin
BTC	Benzene-1,3,5-tricarboxylic acid
Cu	Copper

DDS	Drug delivery system
DOX	Doxorubicin hydrochloride
DRS	Diffuse reflectance spectroscopy
DUT	Dresden University of Technology
EDX	Energy-dispersive X-ray spectroscopy
FDA	Food and Drug Administration
FESEM	Field emission scanning electron microscope
FETEM	Field emission transmission electron microscope
FTIR	Fourier transform infrared
GRAS	Generally recognized as safe
HF	Hydrofluoric acid
HKUST	Hong Kong University of Science and Technology
KBr	Potassium bromide
MCF-7	Michigan cancer foundation-7
MCM-41	Mobil composition of matter no 41
MIL	Materials of Institute Lavoisier
MNP	Magnetic nanoparticle
MOF	Metal organic framework
NPs	Nanoparticles
PBS	Phosphate buffer saline
PCN	Porous coordination network
PMO	Periodic mesoporous silica
SAED	Selected area electron diffraction
SBA-15	Santa Barbara amorphous type material
STP	Standard temperature and pressure

TEM	Transmission electron microscopy
TGA	Thermogravimetric analysis
UiO	Universitetet i Oslo
UV-Vis	Ultraviolet-visible spectrophotometry
VSM	Vibrating sample magnetometer
XRD	X-ray diffraction analysis
ZIF	Zeolitic imidazolate framework

Chapter 1
Introduction

Chapter 1

Introduction

Over the decades, a number of different nanoparticle based approaches have been developed to improve the efficacy of conventional drug delivery. Among them porous metal organic frameworks (MOFs) are emerged as promising candidates as a drug carrier. Although pure MOFs as a carrier is well established, still these materials present few challenges in terms of improvement in drug loading capacity. This chapter highlights the overview of drug delivery system and different drug carriers including MOFs. The chapter subsequently presents the literature review and research objectives of the thesis.

1.1 Overview of drug delivery

A drug is a chemical substance that has known biological effects on humans and other animals. In medical science, drug is a chemical substance used in the treatment, cure, prevention, or diagnosis of disease. Drug is required to correct imbalances caused by genetic predispositions, injury, ageing, and external invasion. In ancient times, human civilizations have utilized plant-based products as medicines against diseases. Natural substances taken from plant are tested and used to treat impairment of physiological life processes, pain and discomfort. With the advancement of science and engineering, the active ingredients/components of these materials, the drugs, are identified and isolated. New drug candidates are tested even today in the pursuit of effective tools against diseases.[1, 2] In conventional process, drug is administered in the body by the following routes like oral, parenteral, transnasal, transmucosal, pulmonary, transdermal way, etc. The choice of the route of drug administration depend on the disease, the effect desired

and the availability of the said medicine. A drug activity is a result of molecular interactions to certain cells, so it is required for a drug to reach the site of action by any administration route at sufficient concentration. The scientific field dealing with this issue is known as drug delivery and has essentially the following objectives: to deliver the drug or therapeutic agent at the right place, with desired concentration periodically without any partial degradation of the drugs. When it is impossible by simply selecting an administrative route or if such administration causes patient discomfort or pain, strategies based on the formulation of the drug with a carrier (drug delivery system-DDS) are an alternative way. [3, 4]

In general, a drug delivery system is an interface between the patient and the drug. It focuses on the development of technologies to deliver biomolecules or drugs to the disease site at a desired concentration, with minimalize side effects and enhance patient compliance. The major issue of this kind of system lies on the complexity associated with the path, which through drug molecules reached to preferred tissues, cells or organs. Free drugs, tends to reduce the actual concentration due to exposure of various metabolic processes once entered into the bloodstream or body fluid. These causes the reduction of drug concentration at the preferred cells or organs and may responsible for unwanted side effects. The best examples are chemotherapeutic medicines suffering from these limitations. To overcome these limitations, emphasis is given to design or fabricate different drug carriers. These carriers should perform multiple tasks including high drug loading capacity, controlled release, overcome of biological barriers etc.[3,5,6]

1.2 Controlled drug release system

Controlled release system is defined as slow release of drug over an extended period of time with some control. It helps to deliver the drug to desired site of action with minimizing drug exposure elsewhere in the body.[4] In traditional way, once the drug or medicine is injected in the body, the drug level rises in the blood in each administration and then further decreases until next administration. The key point for any drug administration is that the concentration level of that medicine should lies between a maximum (representation of toxic level in blood plasma) and a minimal, below which the medical drug is no longer effective. In controlled drug release system, the level of concentration follows a steady profile in between desired maximum and minimum for a longer period of time shown in **Figure 1.1**. [4,7]

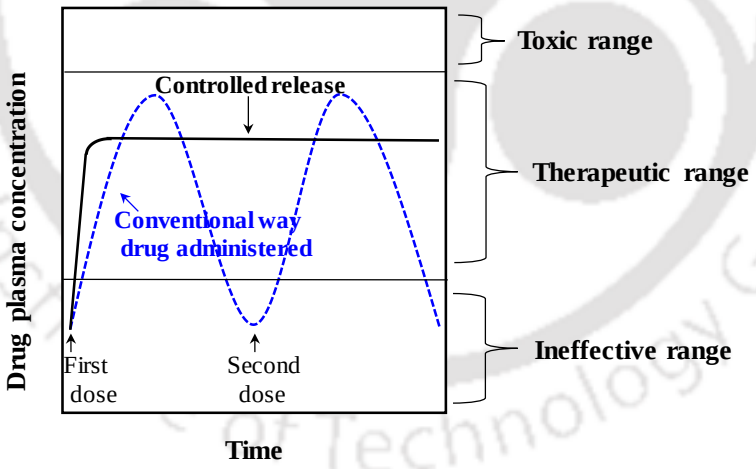

Figure 1.1: Concentration profiles for drug delivered by tablets and controlled release device [Ref. 4, 7]

Controlled release of any therapeutic drug is required for following few occasions where oral or injectable drug formulations cannot be used. [8] These are as follows:

I. Situation requiring slow release of water soluble drugs.

II. Fast release of low-solubility drugs.

III. Drug delivery by nanoparticulate system.

IV. Delivery to specific sites.

V. Delivery of two or more drugs/agents with the same formulation.

1.3 Carriers for drug delivery

Various types of carriers like liposomes [9-11], micelles [12-14], dendrimers [15-17], inorganic nanoparticles [18-20], protein [21-23], polymer nanoparticles [24-26], carbon nanostructures [27-29], porous materials [30-33] and quantum dots [34-36] are used as drug carriers until now. An ideal carrier should have following characteristics. [37-38]

a) High drug loading capacity.

b) Sustained/controlled release of drug.

c) Stability of carriers in different pH conditions.

d) Targeted delivery can be readily achieved by active targeting or passive targeting.

e) Reduce toxicity of the drug in non-targeted areas.

f) It should be in suitable size-range (micro/nano) for easy penetration to biological cell membranes.

g) The carrier must be non-cytotoxic and biocompatible.

h) Carriers shall be used to improve the stability of the drugs. Molecular level isolation and protection of the drug against inactivation during the passage of journey to target cells.

i) It must have appropriate cellular adhesion, endocytosis, intracellular trafficking to allow therapeutic delivery

j) Ease of consistent, reproducible, clinical-grade synthesis.

k) Helps to maintain other biological activity.

The schematic of few carriers are described in **Figure 1.2**. [32,39,40]

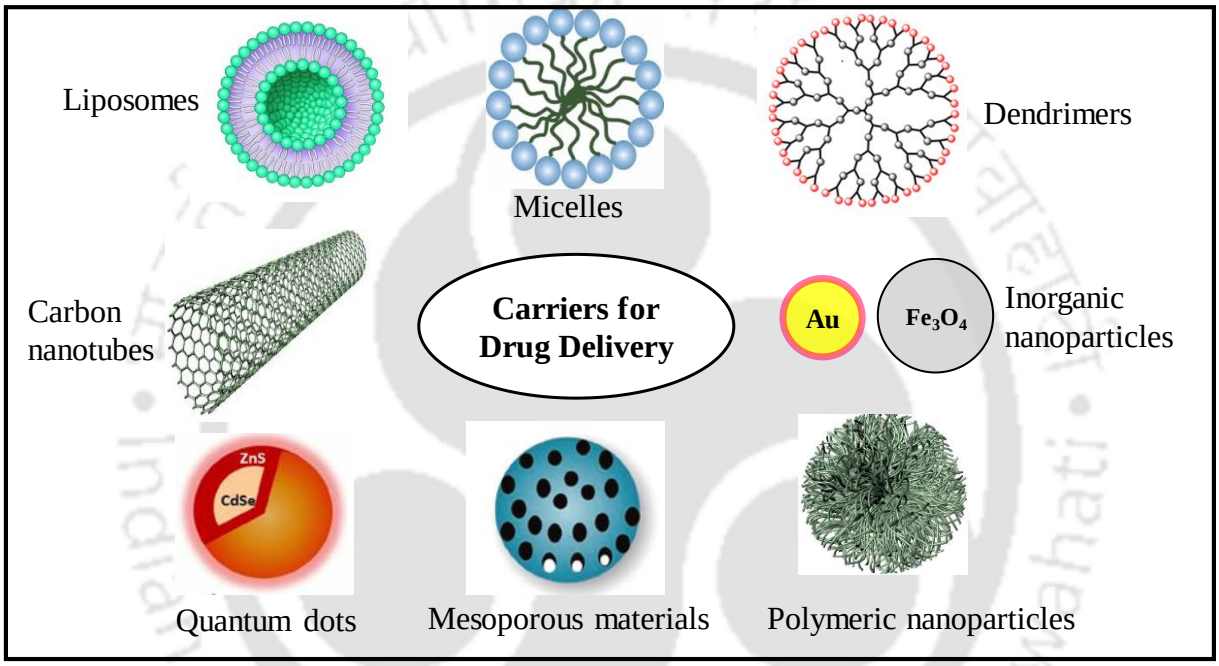

Figure 1.2: Examples of various carriers used for drug delivery

1.4 Porous materials as drug carriers

Porous materials gained more attentions as drug carriers owing to its large surface area, high porosity, stable uniform porous structure, tunable pore sizes with narrow distribution, well defined inner and outer surface properties. [41] The word pore comes from the Greek word *'πορος'*, and it means passage. A pore is a passage between external and internal surfaces of solid. It allows materials or drug to pass into, through or out of the material. [42] In general,

IUPAC classified porous materials according to pore diameter into three categories: microporous (pore diameter < 2 nm), mesoporous (2-50 nm) and macroporous (> 50 nm).[43] In addition, porous materials are also classified as per the build-up frameworks projected in **Figure 1.3**. [44]

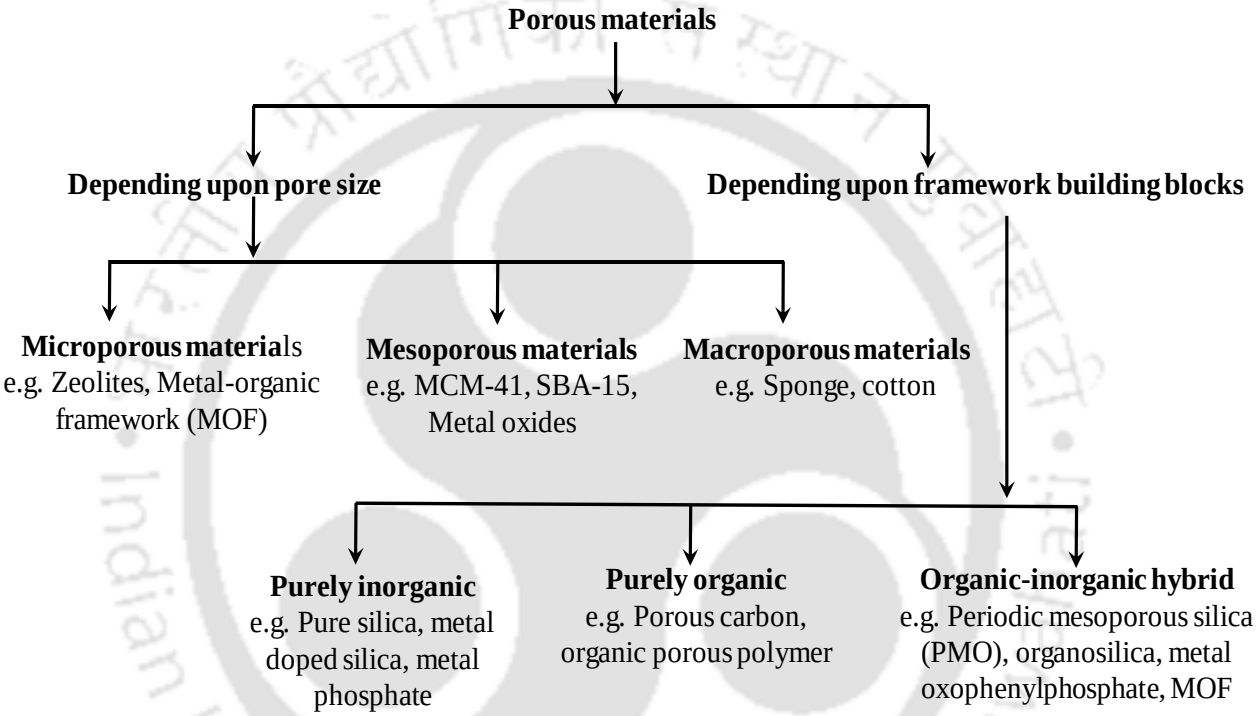

Figure 1.3: Schematic representation of classification of porous materials

Porous materials are extensively used as carriers for gastrointestinal drug, intravenous drug delivery systems, and pulmonary delivery systems. These include small molecule drugs, macromolecular proteins and, polypeptides drugs.[45-47] In addition, porous materials are also investigated as carrier for anticancer medicines and gene therapy.[48-50] Among them metal-organic frameworks (MOFs) have been emerged in biomedical applications such as drug storage and its delivery due to their physical and chemical characteristics.[51]

1.5 Metal organic frameworks (MOFs)

The term "metal-organic frameworks" is first ascribed by Omar Yaghi in the year of 1995.[52-55] Metal-organic frameworks (MOFs) a class of porous materials are comprising of metal ions and organic linkers. A variety of MOFs can be designed by changing the organic linkers, metal ions and reaction conditions.[56-58] The resulting MOF structure can be categorized into four dimensionalities. These are zero-dimensional (0D) such as hollow capsules or microspheres, one-dimensional (1D) such as nanorods or nanofibers, two-dimensional (2D) such as thin films, membranes etc. and three-dimensional (3D) architectures that consists of continues and extended system.[59] A general scheme of three-dimensional metal-organic framework (MOF) construction is shown in **Figure 1.4**.

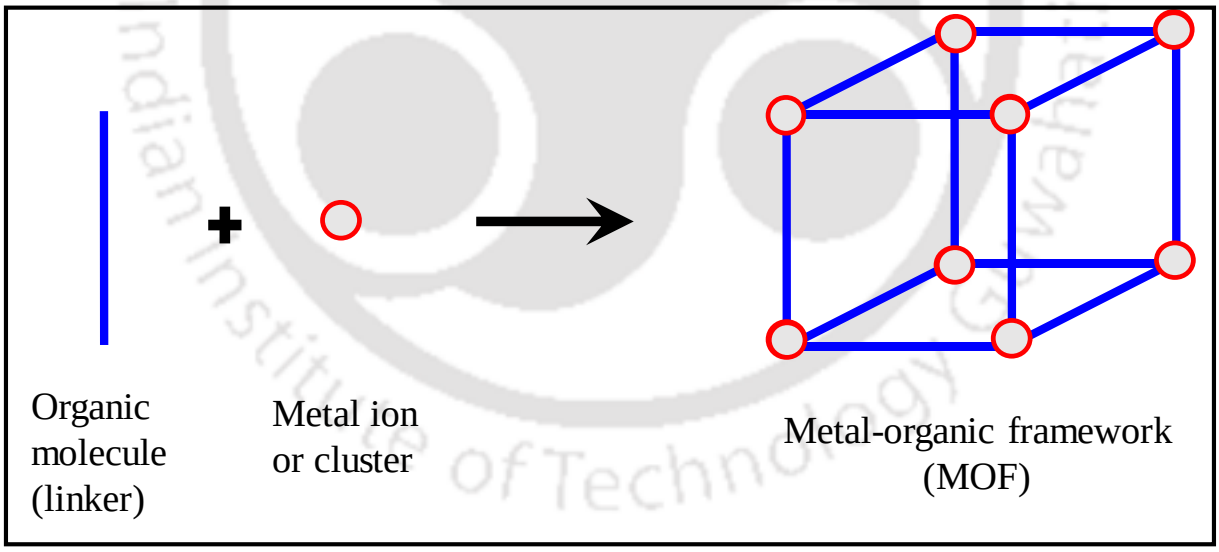

Figure 1.4: A general scheme of three-dimensional MOF construction [57, 58]

1.6 Synthesis of MOFs

There are many synthesis methods for MOF synthesis are reported till date like solvothermal method (conventional approach),[60] microwave,[61] sonochemical,[62] mechanochemical approach,[63] etc. The selection of suitable method for MOF synthesis is an important aspect. As the chosen synthesis method affects the size and morphology of MOF structure with its efficiency (in terms of % yield). Mostly, the syntheses are performed in liquid phase; as solid-phase synthesis always faces difficulty to obtain single crystals and thus the product structure.[64] A summary of various synthesis approaches is given in **Figure 1.5**.

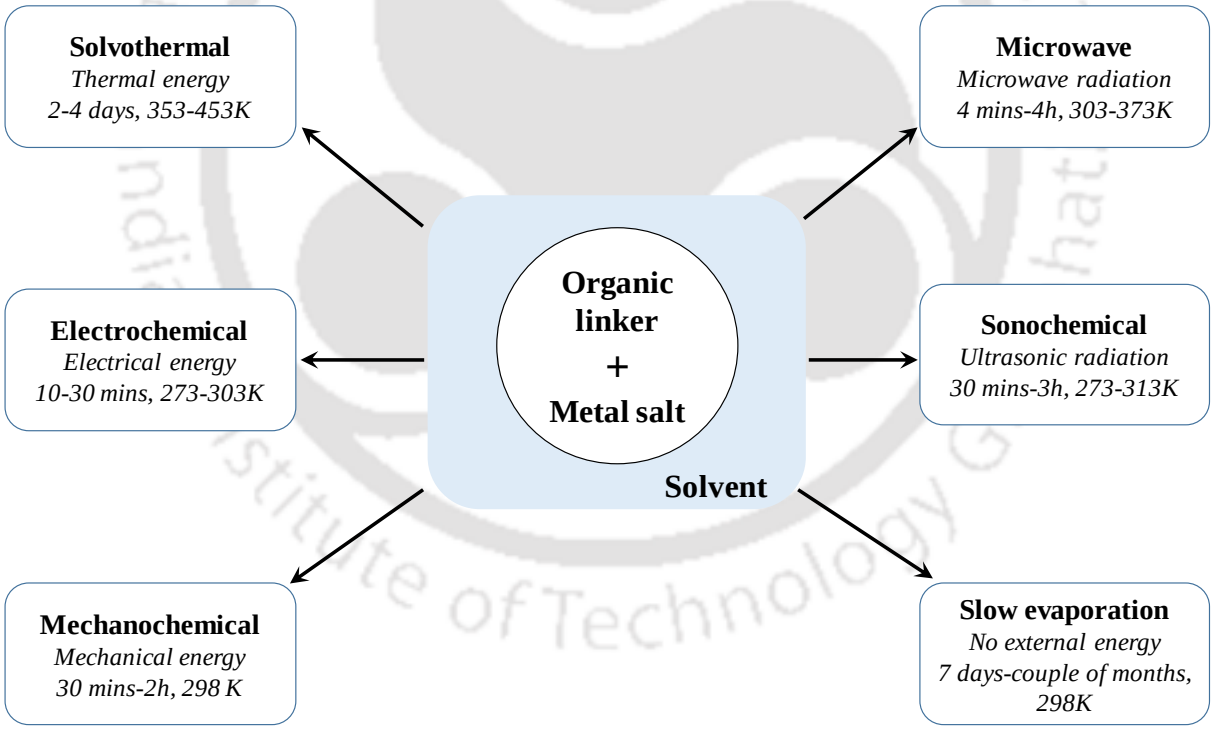

Figure 1.5: Synthesis methods used in MOF synthesis [64, 65]

Among all the methods, solvothermal method is the most popular due to resultant formation of stable MOF structure. In addition, other synthesis methods are just emerging; reliability and reproducibility of those processes yet to established.[65, 66] Solvothermal synthesis also includes hydrothermal (water is used as solvent)[67] and ionothermal (ionic liquid as solvent)[68] processes. Hydrothermal synthesis of MOFs offers number of advantages over other synthetic methods. In this route, the reaction is carried out in a closed system at higher temperature (more than 100 °C) and above one atmosphere pressure. It leads to development of large MOF crystals with high purity due to high solubility of the reactants in such elevated temperature and pressure. Hydrothermal synthesis is necessary when the organic linkers used in the raw precursors are not completely soluble in ordinary conditions.[69] The most common solvents for solvothermal process are water, alcohols, acetone, acetonitrile or dialkyl formamides etc. In addition, mixtures of solvents are also employed in few cases to avoid the problem of differing the solubility of various starting materials[64] and to explore the various topologies of the MOF networks.[70] The reaction mixture is heated in sealed vessels such as Teflon-lined stainless steel bombs or glass vials, generating autogenous pressure. In few synthesis, modulators or mineralizers are often used to affect the crystal size in MOF structure. Typically, mineralizers are weak acids which can help to solubilizing the starting materials, stabilizing or inhibiting transient structures, thus increase the crystallinity and crystal growth of the final product.[66] In case of carboxylate-based MOFs with trivalent metal ions for example Cr-MIL-53,[71] MIL-71,[72] MIL-96, MIL-100,[73] Cr-MIL-101[74] MOFs, fluoride was used to improve the crystallinity. Similarly, in case of UiO-66 (Zr-BDC MOF), benzoic acid was added to regulate the MOF crystallinity. [75]

Table 1.1: Some commonly used organic linkers in MOF synthesis

Organic Linker		MOF	Ref.
Name	**Structure**		
Benzene 1,4-dicarboxylic acid (BDC)	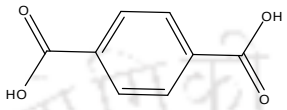	UiO-66 MIL-53 MIL-101 M2(BDC)2 DABCO (M: Zn, Ni)	[76] [77] [78] [79]
2-amino, benzene 1,4-dicarboxylic acid	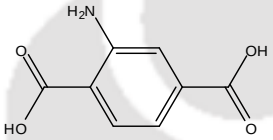	NH_2-MIL-53 IRMOF-3	[80] [81]
Benzene 1,3,5-tricarboxylic acid (BTC)	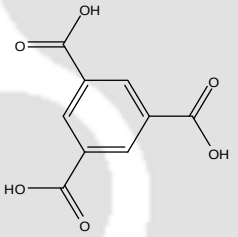	Cu-BTC or HKUST MIL-100	[82] [83]
2,5-dihydroxy, benzene 1,4-dicarboxylic acid	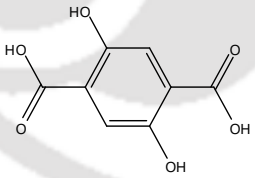	MOF-74 or M-DOBDC (M = Mg, Zn, Mn etc.)	[84,85]
Tetrakis (4-carboxyphenyl) porphyrin (TCPP)	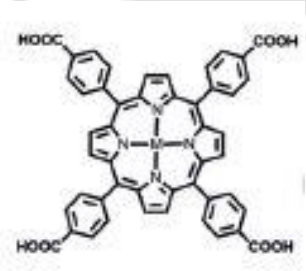	PCN-222 (M: Fe, Zn, Mn, Ni etc.)	[86]

1.7 MOF families and classifications

There are different kind of MOF series have been emerged with time since its first reported by Yaghi et. al.[52] The naming of these different classes or families of MOF are done in following aspects such as (a) material composition; (b) function; (c) structure and (d) laboratory/institution name.[87]

Table 1.2: Classifications, abbreviations and full names of MOF families

Classifications	Abbreviations	Full names	Ref.
Material composition	MOF-n	Metal-organic Framework	[54]
	MPF-n	Metal Peptide Framework	[88]
	CD-MOF-n	Cyclodextrin-based Metal-organic Framework	[89]
	Bio-MOF-n	Bio-metal-organic Framework	[90]
Function	IRMOF-n	Isoreticular Metal-organic Framework	[55]
	MTV-MOF-n	Multivariate Metal-organic Framework	[91]
Structure	ZMOF-n	Zeolite-like Metal-organic Framework	[92]
	ZIF-n	Zeolitic Imidazolate Framework	[93]
	PCN-n	Porous Coordination Network	[94]
Laboratory or institution	CPO-n	Coordination Polymer of Oslo	[95]
	CAU-n	Christian-Albrechts-University	[96]
	NU-n	Northwestern University	[97]
	NOTT-n	University of Nottingham	[98]
	HKUST-n	Hong Kong University of Science and Technology	[99]
	MIL-n	Materials of Institute Lavoisier	[100]
	DUT-n	Dresden University of Technology	[101]
	UTSA-n	University of Texas U.S.A	[102]
	FJI-n	Fujian Institute of Research on the Structure of Matter	[103]

So, naming of the MOFs has no certain rule until now. In general, the MOF families prepared by same synthetic method are entitled in same letters in front with different last numbers.

For example, Yaghi and co-workers are renowned for preparation of isoreticular MOF (IRMOF).[55] Here, "IR" stands for isoreticular and the MOF family is abbreviated as "IRMOF-n".[55] So, the naming of this MOF is based on function and number "n" is the serial order of the occurrence of each MOF in the family. However, in other cases, the naming is not the same as in case of "IRMOF-n". For example, in case of "MIL-n" family, the "MIL" stands for "Materials of Institute Lavoisier" and "n" represents the serial number.[87] The systematic classifications of different MOF families are given in **Table 1.2**.

1.8 Metal organic frameworks as drug carriers

Metal organic frameworks (MOFs) have received tremendous attention in recent years due to its ultra-high porosity, enormous surface areas and tunable structural and chemical properties. These properties along with amazing variability of inorganic and organic components of their structures, make MOFs as a suitable candidate for gas separation, clean energy, adsorption, catalysis and biomedical applications. [51,104] MOFs has been accepted as a good candidate for drug loading and controlled delivery owing to its porosity, tunable structures and sufficient stability under physiological conditions. [104,105] The applications of MOFs or MOFs based carriers in the field of drug encapsulation and biomedical field have grown in enormous rate in last decade (**Figure 1.6**). Among them few MOFs based drug carriers with applications are shown in **Table 1.3**.

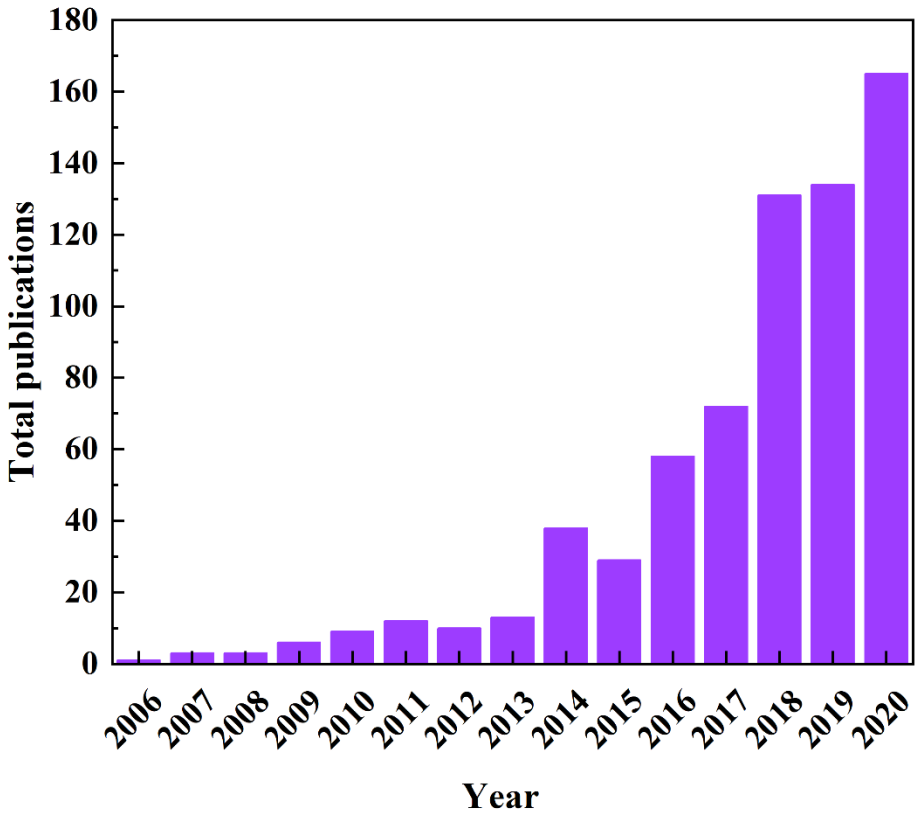

Figure 1.6: Number of publications containing the key word "Metal Organic frameworks in the field of drug delivery and biomedical applications" in the past 15 years (Source: SciFinder Scholar, accessed on 10/02/2021)

Among all the diseases, Cancer causes millions of death annually.[106] Chemotherapy is a dominant treatment method for cancer therapy in worldwide; however chemotherapeutic drugs possess several limitations to the patients like poor bio-distribution, undesirable side effects and poor pharmacokinetics.[107]

Table 1.3: Different MOFs based drug carriers and their applications

MOFs	Metal ions	Organic linkers	Loaded drug	Applications	Ref.
MIL-53	Cr^{3+}, Fe^{3+}	BDC	Ibuprofen (IBU)	Analgesic and anti-inflammatory	[108]
ZIF-8	Zn^{2+}	2-Methylimidazole	5-Fluorouracil (5-fu)	Treatment of breast, head, neck cancer	[109]
ZIF-8	Zn^{2+}	2-Methylimidazole	Camptothecin (CPT)	MCF-7 breast cancer cells treatment	[110]
MIL-100	Fe^{3+}	BTC	Cidofovir (CDV)	Cure viral infections	[111]
HKUST-1	Cu^{2+}	BTC	Nitric oxide (NO)	Antithrombotic therapy	[112]
Fe_3O_4@HKUST-1	Cu^{2+}	BTC	Nimesulid (NIM)	Treatment of pancreatic cancer	[113]
γ-CD-MOFs	K^+	γ-Cyclodextrin (γ-CD)	Fenbufen (FBF)	Analgesic and anti-inflammatory	[114]
MIL-101	Fe^{3+}	BDC	Cisplatin	Treatment of therioma	[115]
UiO-66	Zr^{4+}	BDC	Alendronate (AL)	Extra-skeletal malignancies remedy	[116]
Fe_3O_4@UiO-66	Zr^{4+}	BDC	Doxorubicin (DOX)	Cure breast cancer	[117]
UiO-67	Zr^{4+}	4,4'-Biphenyldicarboxylic acid	Brimonidine tartrate	Chronic glaucoma therapy	[118]

Thus various efforts have been made to develop the carriers for controllable chemotherapeutic drug release to reduce unwanted side effects and increase therapeutic efficiency. These carriers are mesoporous silica, quantum dots, metal nanoparticles, liposomes,

micelles.[37] However, all these carriers have certain limitations related to loading capacities, undesirable toxicity and poor degradability or unwanted release of drug in the physiological conditions. [107,119]

In recent years, MOFs have received significant attentions in the field of anticancer drug delivery due to its versatile structure with diverse morphologies, compositions, sizes, chemical properties with multi functionality.[107] These characteristics of MOFs endow them for controlled drug release and thus contribute to the efficiency of the treatment.[58,107] In addition, it is reported that modification of these materials does not alter the physiochemical properties in the parent MOF i.e., MOF-based materials still remain their size, shape and uniformity.[120]

1.9 Nanoparticles based MOFs composites

Composites based on nanoparticles and MOFs are the new class of hybrid porous materials. Among those, metal oxide nanoparticles based MOFs composites are emerged recently. It combines the porosity of MOFs with versatile functionality of the nanoparticles. [121] These composites can be prepared by several techniques such as chemical vapor infiltration, solution impregnation, solid grinding etc. [121, 122] Alternatively, an 'one-pot' approach can be applied for composite synthesis, where MOF is crystallized in the presence of preformed nanoparticles. Thus, MOFs encapsulates the nanoparticles in the resulting composites. The synthesis conditions applied in this route do not affect the composition, structure and morphology of the preformed nanoparticles. [121, 123] The existence of nanoparticles can provide some additional features in MOFs morphology or structure. In addition, structure of the MOFs can restrict the uncontrolled release of drug/cargo which is prominent in case of bare nanoparticles.[124]

1.10 State of the art

With a brief overview of the contemporary research, this section outlines the research outcome of various literatures so as to identify few promising areas of research that needs to be addressed here. The state of the art has been presented for iron carboxylates MIL-100(Fe) MOF and its nanoparticles composites for drug loading and release applications.

1.10.1 Development of mesoporous iron(III) trimesate MIL-100 MOF and its application as a drug carrier

In general, a drug delivery system (DDS) delivers the drug at a desired concentration and rate to the preferred tissues, organs or cells in the human body.[125] In addition, it improves the drug delivery efficiency and reduce undesirable side effects. [126,127] Various systems such as polymeric nanoparticles, micelles, liposomes, emulsions etc. have been used for controlled and targeted delivery.[128-131] In addition, porous materials also have significant potential as drug delivery systems. Several mesoporous materials with high surface area, pore volume and tunable pore sizes have been developed for these applications.[132-134]

MCM-41, a mesoporous material was first reported as a carrier for anti-inflammatory drug ibuprofen.[135, 136] Other mesoporous materials such as carbon, hydroxyapatite, metal oxides, metal doped nanoparticles, hydrogels were also investigated for delivery of a variety of drugs.[137] These materials were used as carriers to host the drugs that are used in the treatment of Parkinson's disease, hyperlipidemia, diabetes, inflammation, cancer, etc. [137]

Metal-Organic frameworks (MOFs) are identified as new generation materials in healthcare system, owing to their open crystalline structures, remarkable porosity, functionality, chemical and thermal stability. [58,133] MOFs are made by coordinative bonding of metal ions

with suitable organic linkers to form a highly porous structure. They are widely studied in applications such as drug delivery systems (DDS), gas storage, catalysis, adsorptive separations etc. [58, 138-141]

MOFs offer many advantages over existing DDS (inorganic or organic drug carriers) due to their higher payloads and biocompatibility. A significant amount of work has been reported on development of MOFs as a drug carrier in recent years.[142, 143] MIL-101(Cr) and MIL-100(Fe) are the hybrid porous solids first described by Férey et al. and Horcajada et al. in the year 2005 and 2007 respectively.[74, 144] MIL-101(Cr) was studied as a carrier for ibuprofen by Horcajada et al.[145] Later, the same research group explored MIL-100(Fe) for anticancer drug and a controlled drug release profile was observed without any undesirable (initial) burst release. [109] Iron based MOFs are probably most widely studied in biomedical applications due to their higher drug loading capabilities, less toxicity and biodegradability. [105,109,146]

MIL-100(Fe) is formed by connection of Fe metal trimers with an organic linker viz. 1, 3, 5-benzene tricarboxylic acid or trimesic acid. It is originally synthesized via hydrothermal route using hydrofluoric (HF) acid as a crystalizing agent.[144] Chang et al. later synthesized MIL-100(Fe) without the use of HF and it was reported to be suitable for large scale production. [147]

Possible scope for further research

From the synthesis process of MIL-100(Fe), it may be observed that HF plays an important role in the MOF structure formation. So, without HF, less crystalline MIL-100(Fe) may be produced. In addition, some other features like mesopore volume[147] in MIL-100(Fe) might be effected without HF in raw precursors. Therefore, there is enough scope to investigate the effect of various conditions during MIL-100(Fe) synthesis and the drug release application thereon. One of the objective of this work was to study the synthesized MOFs and its use for drug loading

applications. 'Doxorubicin hydrochloride' (DOX) a model anticancer drug was chosen for experiments here.

1.10.2 Development of magnetic iron oxide based MIL-100(Fe) and its application as anticancer drug carrier

There have been continuous attempts made by the researchers to overcome the challenge of controlled drug delivery in the body by some carriers. Cancer has a high mortality rate worldwide, which is initiated by uncontrolled growth and spread of abnormal cells. Conventional anticancer medicines cannot discriminate between tumorous and normal cells. It leads to several adverse side effects and collateral damage to patients in cancer treatments. According to GLOB-CAN 2012 estimates, worldwide there were almost 14.1 million new cancer cases, 8.2 million cancer deaths and 32.6 million people living with cancer (within 5 years of diagnosis).[148-151] Different classes of drug delivery systems (DDS) have been explored to address those issues by enhance the drug delivery efficiency and reduce side effects. In past few decades, nanomaterials and nanotechnology showed great potential in drug delivery, disease therapy particularly in the battle field of cancer. Magnetic nanomaterials are one class of materials that have the potential for biomedical applications such as drug delivery, magnetic resonance imaging (MRI), and hyperthermia. Fe_3O_4 magnetic nanoparticles, have fascinated great attention in the biomedical applications due to their biocompatible, biodegradable, potentially non-cytotoxic and interesting superparamagnetic properties.[152-154] In addition, iron oxide nanoparticles are the only nanoparticles approved for clinical practice by the U.S. Food and Drug Administration.[155] Fe_3O_4 nanoparticles with negative surface charge (citrate stabilized

MNP) can bind to the positively charged drug molecule through electrostatic interactions and can applicable for drug delivery and magnetic hyperthermia applications.[156]

Metal-Organic frameworks (MOFs) are a new class of porous material combined by coordinative bonding of metal ions with suitable organic linker. MOFs have attracted considerable attention due to their high surface areas, crystalline open structures, tunable pore size and functionality. These topographies consider them for gas storage, catalysis, separation and drug delivery applications.[138-140, 145] Férey's group first demonstrated MIL-100(Fe) and MIL-101(Cr) (MIL: Materials of Institut Lavoisier) metal-organic frameworks as drug carrier for ibuprofen delivery. Later, the same group investigated MIL-100 as a potential carrier for anticancer drug doxorubicin. MIL-100 is built up from trimers of metal 'Fe' octahedral and 1,3,5-benzene tricarboxylic acid (BTC) or trimesic acid with possessing high surface area (~ 2000 m^2g^{-1}) and huge pore volume (~ 1.0 cm^3g^{-1}). According to a previous study, a controlled release pattern of drug from porous MIL-100 was seen without any burst effect.[109]

Possible scope for further research

From the above literatures it is envisaged that no study on the use of Fe_3O_4 nanoparticle incorporated MIL-100(Fe) as a carrier for anticancer drug delivery is reported. By incorporating Fe_3O_4 nanoparticles into the MOF structure, it is believed that loading capacity as well as the release profile of said nanoparticles loaded MOF will be significantly influenced. Again, MOF is also likely to exhibit enhanced magnetic properties useful in biomedical applications. The aim of the present work is projected in a way to incorporate Fe_3O_4 nanoparticles into porous MIL-100 structure for better loading efficiencies and with controlled release capabilities. Again, porous coordination network of MIL-100 will also act as a coating material for bare

magnetic nanoparticles (MNPs) to prevent dissolution of ions. Anticancer drug DOX is chosen as model drug. In this work, a facile one-pot method to synthesize Fe_3O_4@MIL-100 composites is reported. To the best of my knowledge, no such literature is available for direct in situ crystallization to Fe_3O_4@MIL-100 composite preparation via hydrothermal route. The synthesis of the composites was done in conventional HF route.

1.10.3 Investigation of drug loading phenomena on nanoparticle incorporated micro and mesoporous iron(III) trimesate MIL-100

In general, a drug delivery system (DDS) focuses both on the target and the carrier, that allows for a controlled release of the drug.[157, 158] A vast amount of research is available for achieving drug delivery at controlled (and desired) delivery rate, to the desired target site while attempting to improve the efficiency, and minimize undesirable side effects.[126,127] Nanoparticles are promising candidates both for diagnosis and treatment of various diseases including cancer.[159] Several types of nanomaterials such as polymers, dendrimers, micelles, liposome-based, silica/carbon- based, metal-based have been widely studied as drug delivery vehicles.[128,129,130,160,161] ZnO nanoparticles and nanostructures are widely used in biomedical applications such as in biosensors, tissue engineering, drug delivery and cancer diagnostics.[162-164] In addition, ZnO is considered to be 'GRAS' (Generally Recognized As Safe) substance by the US Food and Drug Administration (FDA).[165] ZnO nanoparticles were also found to be entirely nontoxic during in vivo animal injection tests.[166]

Metal-Organic frameworks (MOFs) are advanced porous materials formed by coordinated bonding of metal ions and organic linkers. MOFs possess interesting characteristics such as high porosity, open crystalline structures, functionalization as well as good chemical

and thermal stability.[58, 133] In recent years, a vast amount of work was done to develop MOFs as drug carriers. [109,142,143,145] In particular, iron based MOFs are preferred owing to their lower toxicity, higher drug loading capacity and biodegradability. [105,109,146] MIL-100(Fe) is an iron based MOF is built with Fe metal trimers; it may be synthesized by hydrothermal route both in the presence and in the absence of crystalizing agent (HF acid). MIL-100(Fe) synthesized by HF free route is known to have a larger mesoporous volume fraction.[147] In addition, The MTT assay of two cell on MIL-100(Fe) MOF and other studies indicate that its toxicity is low and comparable to other currently commercially available systems. [167-169] So, cytotoxicity studies on both ZnO[15] and MIL-100(Fe)[28-30] were favorable for drug delivery applications.

Possible scope for further research

From the literatures, it is envisaged that no study on the use of ZnO nanoparticle incorporated MIL-100(Fe) as a carrier for anticancer drug delivery is reported. In addition, pure ZnO has higher uptake of DOX (~23 wt%).[170] So, by incorporating ZnO nanoparticles into the MIL-100(Fe) structure, it is believed that loading capacity as well as the release profile of said nanoparticles loaded MOF will be significantly influenced. The synthesis of the composites may be explored in two routes viz. a conventional HF route (in the presence of HF as crystallizing agent) and another in the absence of HF.

1.10.4 Synthesis of nano ceria promoted iron(III) trimesate MIL-100 as a drug carrier

Cancer has the high mortality rate in worldwide and still suffers from appropriate treatment methods.[171] Chemotherapeutic drugs (such as cisplatin, doxorubicin, and methotrexate) are one

of the treatment options for cancer.[172] However, in chemotherapy treatment, a major issue is failure to accumulate and retain desired drug concentration in target site (tumor site). In addition, these drugs suffer to discriminate between tumorous and normal cells; thus increase the nonselective toxicity.[173] Nanoparticles based therapy may be one possible way to minimize above problems and can deliver the therapeutic drugs to the desired site.[174] Various types of nanoparticles (NPs) including liposomes, polymer particles, micelles, dendrimers, quantum dots, gold NPs and carbon nanotubes have been used for therapeutic applications including anticancer drug delivery.[174] Cerium oxide or nano ceria (CeO_2) , a rare-earth metal oxide have gained enormous potential as an antioxidant and radioprotective agents for cancer therapy.[175-177] It is reported that nano ceria's antioxidant properties change with pH; as it can switch from Ce^{3+} to Ce^{4+}. The optimal antioxidant properties for CeO_2 have been reported in acidic pH condition; which is more tumor like envioronment.[178-179] This property of nano ceria may be utilized for protection towards healthy cells and selective killing agent for cancer cells in acidic pH conditions.[180] Furthermore, nano ceria can be helpful to reduce reactive oxygen species (ROS) which is responsible for cancer development and progression.[180-181] Recently, Das et al. reported high DOX loading capacity (22 wt %) for ceria nanoparticles.[182]

Possible scope for further research

From the literatures, it is found that nano ceria (CeO_2) can be utilized as an anticancer drug carrier and as well as to treat the cancer cells. Pure CeO_2 has higher uptake of DOX (22 wt%).[182] Similarly, iron based MOF (MIL-100) are also preferred as carriers owing to their lower toxicity, higher drug loading capacity and biodegradability. [105,109,146] So, there is a scope for further research to develop composites of MIL-100(Fe) and cerium oxide for loading of anticancer drug DOX. Therefore, by incorporating NPs into the MIL-100(Fe) structure, the

DOX loading capacity as well as the release profile can be improved. To the best of my knowledge, no study is reported on the use of CeO_2 nanoparticles promoted MIL-100(Fe) composites as an anticancer drug carrier.

1.11 Objectives and scope of work

In the past decade, MOF materials emerged as new and promising materials for anticancer drug delivery. However, scientific work based on nanoparticles@MOFs composites specially for Iron-carboxylates MOFs for MIL-100 are limited. So, in this work, much emphasizes are given in to develop nanoparticles@MOFs composites as a carrier for anticancer drug "doxorubicin hydrochloride". Iron oxide (Fe_3O_4), zinc oxide (ZnO) and cerium oxide (CeO_2) are chosen as nanoparticles. These above described nanoparticles are widely used in the field of biomedical applications and also approved by several federal agencies.

The main objectives of the thesis are

1. To synthesis of MIL-100(Fe) and investigating its loading and release capacity of doxorubicin hydrochloride.
2. To synthesis Fe_3O_4 promoted MIL-100(Fe) for the controlled release of doxorubicin hydrochloride
3. To synthesis of iron(III) trimesate MOF and ZnO nanoparticle composites for loading and release of doxorubicin hydrochloride
4. To synthesis CeO_2 promoted MIL-100(Fe) for the controlled release of doxorubicin hydrochloride

1.12 Organization of the thesis

In order to fulfil the above objectives, the thesis is organized in seven chapters. The content of each chapter is given below.

Chapter 1 addresses the state of the art, research motivation of present work, possible scope, objectives and organization of the thesis. **Chapter 2** includes protocols about various experiments performed in this thesis. The synthesis procedures for MOFs and different nanoparticles are included. The details about all the material characterization techniques are explained. The protocol related to drug loading and released study are also given in this chapter. **Chapter 3** discusses the details about drug loading and its subsequent release experiments on MIL-100(Fe). The role of mesoporosity and amorphous nature of MOF (in case of MIL-100(Fe)) on drug loading and release are also discussed. **Chapters 4, 5** and **6** compile the results of nanoparticles (Fe_3O_4, ZnO and CeO_2) based MOFs composites synthesis, characterizations and their applications as drug carriers. **Chapter 4** discusses on Fe_3O_4 nanoparticles based MIL-100(Fe) composites prepared by conventional HF route and its drug loading applications. C**hapters 5** and **6** described the composites synthesis in presence and in absence of HF, respectively. **Chapter 7** outlines conclusions of all chapters and some suggestions towards scope for future work.

References

1. J. K. Patra, G. Das, L. F.Fraceto, E. V. R. Campos, M. P. Rodriguez-Torres , L. S. Acosta-Torres, L. A. Diaz-Torres, R. Grillo, M. K. Swamy, S. Sharma , S. Habtemariam and H-S. Shin, *J Nanobiotechnol*., 2018, **16**, 71-103.
2. H. Kubinyi, *Wiley Handbook of current and Emerging Drug Therapies*, 2007, volume **1**, John Wiley & Sons, USA.
3. K. K. Jain, *Drug delivery systems*, 2008, series **437**, Springer publications.
4. J. Siepmann, R. A. Siegel and M.J. Rathbone, *Fundamentals and applications of controlled release drug delivery*, 2012, Springer publications, London.
5. S. Mitragotri and J. Lahann, *Adv. Mater*., 2012, **24**, 3717-3723.
6. N. Doshi and S. Mitragotri, *Adv. Funct. Mater*., 2009, **19**, 3843-3854.
7. E. M. Martín del Valle, M. A. Galán and R. G. Carbonell, *Ind. Eng. Chem. Res*., 2009, **48**, 2475-2486.
8. N.A. Peppas and L. Brannon-Peppas, Drug delivery biomaterials, *Encyclopedia of Materials: Science and Technology (second edition)*, 2001, 2351-2355.
9. R. R. Sawant and V. P. Torchilin, *Soft Matter*, 2010, **6**, 4026-4044.
10. L. Li, X. An and X. Yan, *Colloids Surf. B*, 2015, **134**, 235-239.
11. S. Z. Vahed, R. Salehi, S. Davaran and S. Sharif, *Mater. Sci. Eng. C*, 2017, **71**, 1327-1341.
12. W. Cao, J. Zhou, A. Mann, Y. Wang and L. Zhu, *Biomacromolecules*, 2011, **12**, 2697-2707.
13. S. Pearson, D. Vitucci, Y. Y Khine, A. Dag, H. Lu, M. Save, L. Billon and M. H. Stenzel, *Eur. Polym. J*., 2015, **69**, 616-627.

14. P. Xie and P. Liu, *Int. J. Biol. Macromol*., 2019, **141**, 161-170.

15. H. Yuan, K. Luo, Y. Lai, Y. Pu, B. He, G. Wang, Y. Wu and Z. Gu, *Mol. Pharm*., 2010, **7**, 953-962.

16. T. Wang, Y. Zhang, L. Wei, Y. G. Teng, T. Honda and I. Ojima, *ACS Omega*, 2018, **3**, 3717-3736.

17. D. Huang and D. Wu, *Mater. Sci. Eng. C*, 2018, **90**, 713-727.

18. M. Liong, J. Lu, M. Kovochich, T. Xia, S. G. Ruehm, A. E. Nel, F. Tamanoi and J.I. Zink, *ACS Nano*, 2008, **2**, 889-886.

19.R. Ischakov, L. Adler-Abramovich, L. Buzhansky, T. Shekhter and E. Gazit, *Bioorg. Med. Chem*., 2013, **21**, 3517-3522.

20. Z. Rahiminezhad, A. M. Tamaddon, S. Borandeh and S. S. Abolmaali, *Appl. Mater. Today*, 2020, **18**, 100513.

21. W. Kim, J. Xiao and E. L. Chaikof, *Langmuir*, 2011, **27,** 14329-14334.

22. A. Jain, S. K. Singh, S.K. Arya, S. C. Kundu and S. Kapoor, *ACS Biomater. Sci. Eng*., 2018, **4**, 3939-3961.

23. M. T. de Melo, H. L. Piva and A. C. Tedesco, *Mater. Sci. Eng. C*, 2020, **110**, 110638.

24. J. Nicolas, S. Mura, D. Brambilla, N. Mackiewicz and P. Couvreur, *Chem. Soc. Rev*., 2013, **42**, 1147-1235.

25. A. P. P. Kröger, N. M. Hamelmann, A. Juan, S. Lindhoud and J. M. J. Paulusse, *ACS Appl. Mater. Interfaces*, 2018, **10**, 30946-30951.

26. A. Pourjavadi, M. Kohestanian and C. Streb, *Mater. Sci. Eng. C*, 2020, **108**, 110418.

27. P. Liu, *Ind. Eng. Chem. Res*., 2013, **52**, 13517-13527.

28. R. G. Mendes, A. Bachmatiuk, B.Büchner, G. Cuniberti and M. H. Rummeli, *J. Mater. Chem. B*, 2013, **1**, 401-428.

29. H. Li, X. Sun, Y. Li, B. Li, C. Liang and H. Wang, *Mater. Sci. Eng. C*, 2019, **97**, 222-229.

30. Y. Chen, X. Zheng, H. Qian, Z. Mao, D. Ding and X. Jiang, *ACS Appl. Mater. Interfaces*, 2010, **02**, 3532-3538.

31. J. Gordon, H. Kazemian and S. Rohan, *Mater. Sci. Eng. C*, 2015, **47**, 172-179.

32. J. Florek, R. Caillard and F. Kleitz, *Nanoscale*, 2017, **9**, 15252-15277.

33. B. Lei, M. Wang, Z. Jiang, W. Qi, R. Su and Z. He, *ACS Appl. Mater. Interfaces*, 2018, **10**, 16698-.16706.

34. S. Majumdar, G. Krishnatreya, N. Gogoi, D. Thakur and D. Chowdhury, *ACS Appl. Mater. Interfaces*, 2016, **08**, 34179-34184.

35.A. Sangtani, E. Petryayeva, M. Wu, K. Susumu, E. Oh, A. L. Huston, G. Lasarte-Aragones, I. L. Medintz, W. R. Algar and J. B. Delehanty, *Bioconjugate Chem*., 2018, **29**, 136-148.

36. L. Ruiyi, L. Zaijun, S. Xiulan, J. Jan, L. Lin, G. Zhiguo and W. Guangli, *Chem. Eng. J*., 2020, **382**, 122992.

37. K. Cho, X. Wang, S. Nie, Z. Chen and D. M. Shin, *Clin. Cancer Res*., 2008, **14**, 1310-1316.

38. K. Srikanth, V. R. M. Gupta, S. R. Manvi and N. Devanna, *Int. Res. J. Pharm*., 2012, **3**, 22-26.

39. A. P. Singh, A. Biswas, A. Shukla and P. Maiti, *Signal Transduct. Target. Ther*., 2019, **4**, 33.

40. D. J. Mc Carthy, M. Malhotra, A. M. O'Mahony, J. F. Cryan and C. M. O'Driscoll, *Pharm.Res*., 2015, **32**, 1161-1185.

41. M. Zhou, L. Shen, X. Lin, Y. Hong and Y. Feng, *RSC Adv*., 2017, **07**, 39490-39501.

42. G. Ahuja and K. Pathak, *Indian J. Pharm. Sci*., 2009, **71**, 599-607.

43. X. Du and J. He, *Langmuir*, 2010, **26**, 10057–10062.

44. N. Pal and A. Bhaumik, *Adv. Colloid Interface Sci*., 2013, **189**, 21-41.

45. L. M. Bimbo, M. Sarparanta, H. A. Santos, A. J. Airaksinen, E. Mäkilä, T. Laaksonen, L. Peltonen, V-P. Lehto, J. Hirvonen and J. Salonen, *ACS Nano*, 2010, 4, 3023–3032.

46. S. S. Y. Leung, J. Wong, H. V. Guerra, K. Samnick, R. K. Pruďhomme and H-K. Chan, *AAPS J*., 2017, **19**, 578–586.

47. L. Sun, S. Zhou, W. Wang, X. Li, J. Wang and J. Weng, *Colloids Surf. A*, 2009, **345**, 173–181.

48. K. Tamarov, W. Xu, L. Osminkina, S. Zinovyev, P. Soininen, A. Kudryavtsev, M. Gongalsky, A. Gaydarova, A. Närvänen and V. Timoshenko, *J. Control. Release*, 2016, **241**, 220–228.

49. B. Xia, B. Wang, J. Shi, Y. Zhang, Q. Zhang, Z. Chen and J. Li, *Acta Biomater*., 2017, **51**, 197–208.

50. M. H. Teplensky, M. Fantham, C.Poudel, C. Hockings, M. Lu, A.Guna, M.Aragones-Anglada, P. Z. Moghadam, P. Li, O. K. Farha, S. Fernández, F. M. Richards, D.I. Jodrell, G. K. Schierle, C. F. Kaminski and D. Fairen-Jimenez, *Chem*, 2019, **5**, 2926-2941.

51. I. Erucar and S. Keskin, *J. Mater. Chem. B*, 2017, **5**, 7342-7351.

52. O. M. Yaghi, G. Li and H. Li, *Nature*, 1995, **378**, 703-706.

53. O. M. Yaghi and H. Li, *J. Am. Chem. Soc.*, 1995, **117**, 10401-10402.

54. H. Li, M. Eddaoudi, M. O'Keeffe and O. M. Yaghi, *Nature*, 1999, **402**, 276-279.

55. M. Eddaoudi, J. Kim, N. Rosi, D. Vodak, J. Wachter, M. O'Keeffe, and O. M. Yaghi, *Science*, 2002, **295**, 469-472.

56. O. M. Yaghi, M. O'Keeffe, N. W. Ockwig, H. K. Chae, M. Eddaoudi and J. Kim, *Nature*, 2003, **423**, 705–714.

57. V. Borokov, *Front. Chem*., 2015, **3**, article 50.

58. S. Keskin and S. Kızılel, *Ind. Eng. Chem. Res*., 2011, **50**, 1799-1812.

59. S. Furukawa, J. Reboul, S. Diring, K. Sumida and S. Kitagawa, *Chem. Soc. Rev*., 2014, **43**, 5700-5734.

60. R. Canioni, C. Roch-Marchal, F. Sécheresse, P. Horcajada, C. Serre, M. Hardi-Dan, G. Férey, J-M. Grenèche, F. Lefebvre, J-S. Chang, Y-K. Hwang, O. Lebedev, S. Turner and G.V. Tendeloo, *J. Mater. Chem*., 2011, **21**, 1226-1233.

61. J. Klinowski, F. A. A. Paz, P. Silva and Joao Rocha, *Dalton Trans*., 2011, **40**, 321-330.

62. D-W. Jung, D. Yang, J. Kim, J. Kim and W-S. Ahn, *Dalton Trans*., 2010, **39**, 2883-2887.

63. A. Pichon and S. L. James, *CrystEngComm*, 2008, **10**, 1839-1847.

64. C. Dey, T. Kundu, B. P. Biswal, A. Mallick and R. Banerjee, *Acta Cryst. B*, 2014, **70**, 3-10.

65. I. Kurzydym and I. Czekaj, *Technical Transactions*, 2020, e2020012 (doi.org/ 10.37705/TechTrans/e2020012).

66. N. Stock and S. Biswas, *Chem. Rev*., 2012, **112**, 933-969.

67. Y. Qi, F. Luo, Y. Che, and J. Zheng, *CrystEngComm*, 2008, **8**, 606-611.

68. R. E. Morris, *Chem. Commun*., 2009, **21**, 2990-2998.

69. R. Seetharaj, P.V. Vandana, P. Arya and S. Mathew, *Arab. J. Chem*., 2019, **12**, 295-315.

70. D. Banerjee, J. Finkelstein, A. Smirnov, P. M. Forster, L. A. Borkowski, S. J. Teat and J. B. Parise, *Cryst. Growth Des*., 2011, **11**, 2572-2579.

71. C. Serre, F. Millange, C. Thouvenot, M. Noguès, G. Marsolier, D. Louër, and G. Férey, *J. Am. Chem. Soc.*, 2002, **124**, 13519-13526.

72. K. Barthelet, K. Adil, F. Millange, C. Serre, D. Riou and G. Férey, *J. Mater. Chem*., 2003, **13**, 2208-2212.

73. P. Long, H. Wu, Q. Zhao, Y. Wang, J. Dong and J. Li, *Microporous Mesoporous Mater*., 2011, **142**, 489-493

74. G. Férey, C. Mellot-Draznieks, C. Serre, F. Millange, J. Dutour, S. surblé and I. Margiolaki, *Science*, 2005, **309**, 2040-2042.

75. A. Schaate, P. Roy, A. Godt, J. Lippke, F.Waltz, M. Wiebcke and P. Behrens, *Chem. Eur. J*., 2011. **17**, 6643-51.

76. Y. Cao, Y. Zhao, Z. Lv, F. Song and Q. Zhong, *J. Ind. Eng. Chem.*, 2015, **27**, 102–107.

77. T. Loiseau, C. Serre, C. Hugueanrd, G. Fink, F. Taulelle, M. Henry, T. Bataille and G. Férey, *Chem. Eur. J*., 2004, **10,** 1373–1382.

78. P. Chowdhury, C. Bikkina and S. Gumma, *J. Phys. Chem. C*., 2009, **113**, 6616–6621.

79. Z. Liang, Z. M. Marshall and A. L. Chaffee, *Microporous Mesoporous Mater*., 2010, **132**, 305–310.

80. B. Arstad, H. Fjellvåg, K. O. Kongshaug, O. Swang and R. Blom, *Adsorption.* 2008, **14**, 755–762.

81. A. R. Millward and O. M. Yaghi, *J. Am. Chem. Soc.* 2005, **127**, 17998–17999.

82. P. Chowdhury, C. Bikkina, D. Meister, F. Dreisbach and S. Gumma, *Microporous Mesoporous Mater*., 2009, **117**, 406–413.

83. Y. Georgiou, J. A. Perman, A. B. Bourlinos and Y. Deligiannakis, *J. Phys. Chem. C.* 2018, **122**, 4859-4869.

84. Z. R. Herm, J. A. Swisher, B. Smit, R. Krishna and J. R. Long, *J. Am. Chem. Soc.* 2011, **133**, 5664-5667.

85. H. Wu, W. Zhou and T. Yildirim, *J. Am. Chem. Soc.* 2009, **131**, 4995-5000.

86. X. Yang, S. Yuan, L. Zou, H. Drake, Y. Zhang, J. Qin, A. Alsalme and H-C. Zhou, *Angew. Chem. Int. Ed.*, 2018, **57**, 3927-3932.

87. Y. Wang, J. Yan, N. Wen, H. Xiong, S. Cai, Q. He, Y. Hu, D. Peng, Z. Liu and Y. Liu, *Biomaterials*, 2020, **230**, 119619.

88. M. Shahabi and H. Raissi, *J. Mol. Model*., 2019, **25**, article 304.

89. F. Ke, M. Zhang, N. Qin, G. Zhao, J. Chu and X. Wan, *J. Mater. Sci*., 2019, **54**, 10420-10429.

90. J. An, S. J. Geib and N. L. Rosi, *J. Am. Chem. Soc.* 2009, **131**, 8376-8377.

91. L. Feng, K-Y. Wang, X-L. Lv, J. A. Powell, T-H. Yan, J. Willman and H-C. Zhou, *J. Am. Chem. Soc.* 2019, **141**, 14524-14529.

92. O. Shekhah, A. Cadiau and M. Eddaoudi, *CrystEngComm*, 2015, **17**, 290-294.

93. K.S. Park, Z. Ni, A.P. Côté, J.Y. Choi, R. Huang, F.J. Uribe-Romo, H.K. Chae, M. O'Keeffe and O.M. Yaghi, *Proc. Natl. Acad. Sci. U.S.A.*, 2006, **103**, 10186-10191.

94. X. Lian, D. Feng, Y-P. Chen, T-F. Liu, X. Wang and H-C. Zhou, *Chem. Sci*., 2015, **6**, 7044-7048.

95. K. O. Kongshaug and H. Fjellvåg, *Solid State Sci*., 2002, **4**, 443-447.

96. T. Ahnfeldt, N. Guillou, D. Gunzelmann, I. Margiolaki, T. Loiseau, G. Férey, J. Senker and N. Stock, *Angew. Chem. Int. Ed.*, 2009, **48**, 5163-5166.

97. O.K. Farha, I. Eryazici, N.C. Jeong, B.G. Hauser, C.E. Wilmer, A.A. Sarjeant, R.Q. Snurr, S.T. Nguyen, A.O. Yazaydin and J.T. Hupp, *J. Am. Chem. Soc.*, 2012, **134**, 15016-15021.

98. S. Yang, J. Sun, A.J. Ramirez-Cuesta, S.K. Callear, W.I. F. David, D.P. Anderson, R. Newby, A.J. Blake, J.E. Parker, C.C. Tang and M. Schröder, *Nat. Chem*., 2012, **4**, 887-894.

99. S.S. Chui, S.M. Lo, J.P. H. Charmant, A.G. Orpen and I.D. Williams, *Science*, 1999, **283**, 1148-1150.

100. G. Férey, C. Serre, C. Mellot-Draznieks, F. Millange, S. Surblé, J. Dutour and I. Margiolaki, *Angew. Chem. Int. Ed.*, 2004, **43**, 6296-6301.

101. R. Grünker, V. Bon, P. Müller, U. Stoeck, S. Krause, U. Mueller, I. Senkovska and S. Kaskel, *Chem. Commun*., 2014, **50**, 3450-3452.

102. R-B. hu, L. Li, H-L. Zhou, H. Wu, C. He, S. Li, R. Krishna, J. Li, W. Zhou and B. Chen, *Nat. Chem*., 2018, **17**, 1128-1133.

103. P. Huang, C. Chen, M. Wu, F. Jiang and M. Hong, *Dalton Trans*., 2019, **48**, 5527-5533.

104. H-C Zhou, J. R. Long and O. M. Yaghi, *Chem. Rev*., 2012, **112**, 673-674.

105. S. Rojas, T. Devic and P. Horcajada, *J. Mater. Chem. B*, 2017, 5, 2560–2573.

106. N. G. Zaorsky, T. M. Churilla, B. L. Egleston. S. G. Fisher, J. A. Ridge, E. M. Horwitz and J. E. Meyer, *Ann. Oncol.*, 2017, **28**, 400-407.

107. M-X. Wu and Y-W. Yang, *Adv. Mater*., 2017, **29**, 1606134.

108. P. Horcajada, C. Serre, G. Maurin, N. A. Ramsahye, F. Balas, M. Vallet-Regí, M. Sebban, F. Taulelle, G. Férey, *J. Am. Chem. Soc.*, 2008, **130**, 6774-6780.

109. C. Y. Sun, C. Qin, X. L. Wang, G. S. Yang, K. Z. Shao, Y. Q. Lan, Z. M. Su, P. Huang, C. G. Wang and E. B. Wang, *Dalton Trans*., 2012, **41**, 6906–6909.

110. J. Zhuang, C. H. Kuo, L. Y. Chou, D. Y. Liu, E. Weerapana and C. K. Tsung, *ACS Nano*, 2014, **8**, 2812–2819.

111. P. Horcajada, T.Chalati, C. Serre, B. Gillet, C. Sebrie, T.Baati, J. Eubank, D.Heurtaux, P. Clayette, C. Kreuz, J. Chang, Y. Hwang, V. Marsaud, P. Bories, L. Cynober, S. Gil, G. Férey, P. Couvreur and R. Gref, *Nat. Mater*., 2010, **09**, 172-178.

112. B. Xiao, P. S. Wheatley, X. B. Zhao, A. J. Fletcher, S. Fox, A. G. Rossi, I. L. Megson, S. Bordiga, L. Regli, K. M. Thomas and R. E. Morris, *J. Am. Chem. Soc*., 2007, **129**, 1203–1209.

113. F. Ke, Y. P. Yuan, L. G. Qiu, Y. H. Shen, A. J. Xie, J. F. Zhu, X. Y. Tian and L. D. Zhang, *J. Mater. Chem*., 2011, **21**, 3843–3848.

114. B. T. Liu, Y. P. He, L. P. Han, V. Singh, X. N. Xu, T. Guo, F. Y. Meng, X. Xu, P. York, Z. X. Liu and J. W. Zhang, *Cryst. Growth Des*., 2017, **17**, 1654–1660.

115. K. M. L. Taylor-Pashow, J. D. Rocca, Z. G. Xie, S. Tran and W. B. Lin, *J. Am. Chem. Soc*., 2009, **131**, 14261–14263.

116. X. Y. Zhu, J. L. Gu, Y. Wang, B. Li, Y. S. Li, W. R. Zhao and J. L. Shi, *Chem. Commun*., 2014, **50**, 8779–8782.

117. H. X. Zhao, Q. Zou, S. K. Sun, C. S. Yu, X. J. Zhang, R. J. Li and Y. Y. Fu, *Chem. Sci*., 2016, **7**, 5294–5301.

118. J. Gandara-Loe, I. Ortuño-Lizarán, L. Fernández-Sanchez, J. L. Alió, N. Cuenca, A. V. Estrada and J. Silvestre-Albero, *ACS Appl. Mater. Interfaces*, 2019, **11**, 1924–1931.

119. R. Tong and J. Cheng, *Angew. Chem.* 2008, **120**, 4908 –4912.

120. Q. Wang, Y. Sun, S. Li, P. Zhang and Q. Yao, *RSC Adv.*, 2020, **10**, 37600-37620.

121. P. Falcaro, R. Riccoa, A. Yazdi, I. Imaz, S. Furukawa, D. Maspoch, R. Ameloot, J. D. Evans and C. J. Doonan, *Coord. Chem. Rev*., 2016, **307**, 237-254.

122. C. Rösler and R. A. Fischer, *CrystEngComm*, 2015, **17**, 199-217.

123. C.M. Doherty, D. Buso, A.J. Hill, S. Furukawa, S. Kitagawa and P. Falcaro, *Acc. Chem. Res.*, 2014, **47**, 396-405

124. J. Yoo and Y-Y. Won, *ACS Biomater. Sci. Eng*., 2020, **6**, 6053-6062.

125. C. Li, J. Wang, Y. Wang, H. Gao, G. Wei, Y. Huang, H. Yu, Y. Gan, Y. Wang, L. Mei, H. Chen, H. Hu, Z. Zhang and Y. Jin, *Acta Pharm. Sin. B*, 2019, **9**, 1145- 1162.

126. I. A. Lázaro and R. S. Forgan, *Coord. Chem. Rev*., 2019, **380**, 230-259.

127.S. Javanbakht, M. Pooresmaeil, H. Hashemi and H. Namazi, *Int. J. Biol. Macromol*., 2018, **119**, 588-596.

128. M. E. Peralta, S. A. Jadhav, G. Magnacca, D. Scalarone, D. O. Mártire, M. E. Parolo and L. Carlos, *J. Colloid Interface Sci*., 2019, **544**,198-205.

129. S. Buwalda, B. Nottelet, A. Bethry, R. J. Kok, N. Sijbrandi and J. Coudane, *J. Colloid Interface Sci*., 2019, **535**, 505-515.

130. R. Negrini and R. Mezzenga, *Langmuir*, 2011, **27**, 5296-5303.

131. F. Buyukozturk, J. C. Benneyan and R. L. Carrier, *J. Control. Release*, 2010, **142**, 22-30.

132. M. S. Moorthy, S. Bharathiraja, P. Manivasagan, Y. Oh, B. Jang, T. T. V. Phan and J. Oh, *J Porous Mater*., 2018, **25**, 119-128.

133. M. E. Davis, *Nature*, 2002, **417**, 813-821.

134. H.A. Santos, J. Salonen, L.M. Bimbo, V.-P. Lehto, L. Peltonen and J. Hirvonen, *J. Drug Del. Sci. Tech*., 2011, **21**, 139-155.

135. M. Manzano and M. Vallet-Regí, *J. Mater. Chem*., 2010, **20**, 5593-5604.

136. M. Vallet-Regí, A. Rámila, R. P. del Real and J. Pérez-Pariente, *Chem. Mater*., 2001, **13**, 308-311.

137. P. Singh and K. Sen, *J Porous Mater*., 2018, **25**, 965-987.

138. I. Y. Skobelev, A. B. Sorokin, K. A. Kovalenko, V.P. Fedin and O. A. Kholdeeva, *J. Catal*., 2013, **298**, 61-69.

139. P. Mishra, S. Edubilli, H, P. Uppara, B. Mandal and S. Gumma, *Langmuir*, 2013, **29**, 12162-12167.

140. D. Sahu, P. Mishra, S. Edubilli, A.Verma and S. Gumma, *J. Chem. Eng. Data*, 2013, **58**, 3096-3101.

141. L. He, Y. Dong, Y. Zheng, Q. Jia, S. Shan and Y. Zhang, *J. Hazard. Mater.*, 2019, **361**, 85-94.

142. M. Lismont, L. Dreesen and S. Wuttke, *Adv. Funct. Mater*., 2017, **27**, 1606314.

143.C. Doonan, R. Riccò, K. Liang, D. Bradshaw and P. Falcaro, *Acc. Chem. Res*., 2017, **50**, 1423-1432.

144. P. Horcajada, S. Surblé, C. Serre, D-Y. Hong, Y-K. Seo, J-S. Chang, J-M. Greanèche, I. Margiolaki and G. Férey, *ChemComm*, 2007, **27**, 2820-2822.

145. P. Horcajada, C. Serre, M. Vallet-Regí, M. Sebban, F. Taulelle and G. Férey, *Angew. Chem. Int. Ed*., 2006, **45**, 5974-5978.

146. A.C. McKinlay, R.E. Morris, P. Horcajada, G. Férey, R. Gref, P. Couvreur and C. Serre, *Angew. Chem. Int. Ed*., 2010, **49**, 6260-6266.

147. Y-K Seo, J. W. Yoon, J. S. Lee, U-H Lee, Y. K. Hwang, C-H. Jun, P. Horcajada, C. Serre and J-S. Chang, *Microporous Mesoporous Mater.*, 2012, **157**, 137-145.

148. L. Wu and X. Qu, *Chem. Soc. Rev*., 2015, **44,** 2963–2997**.**

149. D. Zhu, H-M. Wen, W. Li, X-B Cui, L. Ma and A. Kang, *RSC Adv*., 2014, **4** 33391–33398.

150. M. J. Vicent and R. Duncan, *Trends in Biotechnol*., 2006, **24**, 39–47.

151. L. A. Torre, F. Bray, R. L. Siegel, J. Ferlay, J. Lortet-Tieulent and A. Jemal, *Ca Cancer J. Clin*., 2015, **65**, 87-108.

152. G. Wang, L. Jin, Y. Dong, L. Niu, Y. Liu, F. Ren and X. Su, *New J. Chem*., 2014, **38**, 700–708.

153. L. Hajba and A. Guttman, *Biotechnol. Adv*., 2016, **34**, 354–361.

154.Y. Ding, S. Z. Shen, H. Sun, K. Sun, F. Liu, Y. Qi and J. Yan, *Mater. Sci. Eng. C*, 2015, **48**, 487–498.

155. A. Z. Wilczewska, K. Niemirowicz, K.H. Markiewicz and H. Car, *Pharmacol. Rep*., 2012, **64** ,1020–1037.

156. S. Nigam, K.C. Barick, D. Bahadur, *J. Magn. Magn. Mater*., 2011, **323**, 237–243.

157. E. B. Lavik, B. D. Kuppermann and M. S. Humayun, *Chapter 38- Drug Delivery, Retina (fifth edition)*, 2013, **1**, 734-745.

158. CC. Wang, C. He, Z. Tong, X. Liu, B. Ren and F. Zeng, *Int. J. Pharm*., 2006, **308**, 160-167.

159. S. Raj, S. Khurana, R. Choudhuri, K. K. Kesari, M. A. Kamal, N. Garg, J. Ruokolainen, B. C. Das and D. Kumar, *Semin.Cancer.Biol*., 2021, **69**, 166-177.

160. S. Palanisamya and Y-M. Wang, *Dalton Trans*., 2019, **48**, 9490-9515.

161. Z. Mirza and S. Karim, *Semin.Cancer.Biol*., 2021, **69**, 226-237.

162. N. P. Shetti, S.D. Bukkitgar, K. R. Reddy, Ch. V. Reddy and T. M. Aminabhavi, *Biosens. Bioelectron*., 2019,**141**, article 111417.

163. S. Sruthi, J. Ashtami and P.V. Mohanan, *Mater. Today Chem*., 2018, **10**, 175-186.

164. S.S. Bhat, A. Qurashi and F. A. Khanday, *Trend Anal. Chem*., 2017, **86**, 1-13.

165. J. W. Rasmussen, E. Martinez, P. Louka and D. G Wingett, *Expert Opin. Drug Deliv*., 2010, **7**, 1063-1077.

166. H-M. Xiong, *Adv. Mater*., 2013, **25**, 5329–5335.

167. C. Tamames-Tabar, D. Cunha. E. Imbuluzqueta, F. Ragon, C. Serre, M. J. Blanco-Prieto and P. Horcajada, *J. Mater. Chem. B*, 2014, **2**, 262-271.

168. M. Rezaei, A. Abbasi, R. Varshochian, R. Dinarvand and M. Jeddi-Tehrani, *Artif. Cells Nanomed. Biotechnol*., 2018, **46**, 1390-1401.

169. A. Ruyra, A. Yazdi, J. Espin, A. Carné-Sánchez, N. Roher, J. Lorenzo, I. Imaz, and D. Maspoch, *Chem. Eur. J*., 2015, **21**, 2508-2518.

170. Y. Deng and H. Zhang, *Int. J Nanomed*., 2013, **8**,1835-1841.

171. R. Siegel, J. Ma, Z. Zou and A. Jemal, *Ca-Cancer J. Clin*., 2014, **64**, 9−29.

172. S. S. Dhule, P. Penfornis, J. He, M. R. Harris, T. Terry, V. John and R. Pochampally, *Mol. Pharmaceutics* 2014, **11**, 417−427.

173. B. Chertok, B. A. Moffat, A. E. David, F. Yu, C. Bergemann, B. D. Ross and V. C. Yang, *Biomaterials*, 2008, **29**, 487-496.

174. S. Barua and S. Mitragotri, *Nano Today*, 2014, **9**, 223-243.

175. C. Bouzigues, T. Gacoin, and A. Alexandrou, *ACS Nano*, 2011, **5**, 8488-8505.

176. A.S. Karakoti, N.A. Monteiro-Riviere, R. Aggarwal, J.P. Davis, R.J. Narayan, W.T. Self, J. McGinnis and S. Seal, *JOM*, 2008, **60**, 33-37.

177. M. Sack, L. Alili, E. Karaman, S. Das, A. Gupta, S. Seal and P. Brenneisen, *Mol. Cancer Ther*. 2014, **13**, 1740−1749.

178. J. M. Dowding, S. Das, A. Kumar, T. Dosani, R. McCormack, A. Gupta, T. X. T. Sayle, D. C. Sayle, L. Kalm, S. Seal and W. T. Self, *ACS Nano*, 2013, **7**, 4855-4868.

179. A. Asati, S. Santra, C. Kaittanis, S. Nath, and J. M. Perez, *Angew. Chem. Int. Ed*., 2009, **48**, 2308 –231.

180. E. Alpaslan, H. Yazici, N. H. Golshan, K. S. Ziemer and T. J. Webster, *ACS Biomater. Sci. Eng*., 2015, **1**, 1096-1103.

181. M.S. Wason and J. Zhao, *Am. J. Transl. Res*., 2013, **5**, 126-131.

182. J. Das, Y-J. Choi, J. W. Han, A. M. M. T. Reza and J-H. Kim, *Sci. Rep*., 2017, **7**, 9513.

Chapter 2
Experimental

Experimental

This chapter presents the details about raw materials and procedures used for various experiments performed in this thesis. The synthesis measures for MOFs and different nanoparticles synthesis are included. The details about all the material characterization techniques are explained. The protocol related to drug loading and released study are also given in this chapter.

2.1 Chemicals and reagents

The chemicals and regents used to conduct experiments for fulfilling the objectives for this thesis are presented in **Table 2.1**.

Table 2.1: Details of all the chemicals and reagents

Sr. No.	Chemicals/solvents/drug	Make	Purity/ concentration
01	Iron powder	Loba Chemie, India	99.5%
02	Iron(III) nitrate, nonahydrate ($Fe(NO_3)_3.9H_2O$)	Merck, India	98%
03	Iron(III) chloride, hexahydrate ($FeCl_3.6H_2O$)	Himedia, India	99%
04	Iron(II) chloride, tetrahydrate ($FeCl_2.4H_2O$)	Sigma-aldrich	99%
05	Zinc acetate dehydrate ($Zn(CH_3CO_2)_2.2H_2O$)	Merck, India	98%
06	Cerium nitrate hexahydrate ($CeNO_3.6H_2O$)	Sigma-aldrich	99%
07	Sodium hydroxide (NaOH)	Merck, India	97%
08	Sodium chloride (NaCl)	Merck, India	99%
09	Potassium chloride (KCl)	Merck, India	99%
10	di-sodium phosphate (Na_2HPO_4)	Merck, India	99%

11	Potassium dihydrogen phosphate (KH_2PO_4)	Merck, India	98%
12	Trimesic acid/BTC ($C_9H_6O_6$)	Sigma-aldrich	95%
13	Ammonium hydroxide (NH_4OH)	Merck, India	25%
14	Dimethylformamide (DMF)	Merck, India	99%
15	Methanol (CH_3OH)	Merck, India	99%
16	Ethanol (C_2H_5OH)	Merck, India	99.9%
17	2-propanol ($(CH_3)_2CHOH$)	Merck, India	99%
18	Acetone ($(CH_3)_2CO$)	Merck, India	99%
19	Hydrofluoric acid (HF)	Merck, India	48%
20	Nitric acid (HNO_3)	Merck, India	69%
21	Hydrochloric acid (HCl)	Merck, India	35%
22	Dextran (T-10)	SRL, India	----------
23	Doxorubicin hydrochloride ($C_{27}H_{29}NO_{11}.HCl$)	Fresenius Kabi Oncology Ltd., India	2 mg/ml

2.2 Synthesis

The various routes available for metal-organic framework synthesis are solvothermal/hydrothermal, microwave assisted, sonochemical, electrochemical and mechanochemical, etc.[1] Among these, solvothermal route is quite known in the field of material science as described in previous chapter. In solvothermal process, chemical reactions are performed in sealed vessel in presence of solvents. In addition, temperature of the solvents can be brought to their critical point by heating and autogenous pressure. The process is called hydrothermal when water is used as a solvent. In most of the cases, a sealed reactor is used which is also called autoclave or high-pressure bomb. These autoclaves have further linings with Teflon or other alloy materials to protect the autoclave body from the solvent at elevated

temperature and pressure. [2] A Teflon lined stainless steel autoclave is shown in **Figure 2.1** and used for synthesis of pure MOF and MOF-nanoparticles composites.

Figure 2.1: Autoclave reactor for MOF and MOF-nanoparticle synthesis

2.2.1 Synthesis of MIL-100 (Fe)

MIL-100(Fe) was prepared through HF route by hydrothermal reaction of iron powder, trimesic acid (BTC), HF, HNO_3 and water with slight modifications to the procedure reported earlier.[3,4] Typically, 0.27 g of iron metal powder and 0.68 g of BTC, 0.17 ml of HF, 0.13 ml of HNO_3 and 24 ml of water were mixed and sonicated for 1 h. The reaction mixture was then transferred into a Teflon lined autoclave and heated for 12 h at 150 °C. The product was cooled to room temperature was separated from the mother liquor by centrifugation. In the purification step, about 1 g of the separated product was boiled in about 500 ml of hot water at 90 °C for 15 h under continuous stirring (the water was replaced after every 5 h). The MOFs was then filtered off while the solution was hot. In the subsequent step, the product was boiled in about 100 ml of hot ethanol at 80 °C for about 12 h under continuous stirring. The solid product was removed from hot ethanol by centrifugation. Finally, the material was dried overnight at 150 °C.

HF free synthesis: MIL-100(Fe) was also prepared without the use of mineralizing agent i.e. HF.[4] In this case, $Fe(NO_3)_3.9H_2O$ was used as metal source. Typically, 8.08 g of $Fe(NO_3)_3.9H_2O$ was dissolved in 20 ml of water and then 2.7 g BTC was added to that solution. The mixture was stirred continuously for 1 h at room temperature and then loaded into a Teflon lined autoclave. The reaction was allowed to proceed under autogenous pressure for 12 h at 150°C. Subsequent purification steps were same as in the case of MIL-100(Fe) by HF route.

2.2.2 Synthesis of Fe_3O_4 nanoparticles

Fe_3O_4 was prepared by chemical co-precipitation method using of Fe^{2+} and Fe^{3+} salts in aqueous ammonia solution discussed elsewhere. [5-9] In a typical synthesis, about 80 ml of water was taken into a conical flask and deoxygenated by subjecting it to several alternate cycles of sonication and bubbling of nitrogen gas (N_2). Under this non-oxidizing environment, 2.72 g of $FeCl_3.6H_2O$ and 0.99 g of $FeCl_2.4H_2O$ (molar ratio of Fe^{+2} Fe^{+3} = 1:2) were dissolved in water with vigorous stirring (1000 rpm). The solution was then heated to 80 °C at a rate of about 5 °C/min. Simultaneously; NH_4OH (about 10 ml) was added dropwise to this solution until the resulting pH reaches 10. The reaction was allowed to progress for another 30 min under N_2 blanket at 80 °C with vigorous stirring. The solution was cooled to room temperature and the resultant black particles were washed with water several times to remove all the unreacted species. Finally, the wet particles were dried overnight under vacuum at 70 °C.

2.2.3 Synthesis of ZnO nanoparticles

ZnO nanoparticles were prepared by wet chemical method using of zinc acetate salt in methanol solution discussed elsewhere. [10] In a typical synthesis, about 3.96 g of zinc acetate dehydrate

($Zn(CH_3CO_2)_2$, $2H_2O$) in 80 ml of methanol was taken into a round bottom flask. The solution was refluxed at 60 °C for about 15-20 minutes. Then, 2 ml of water is added to that solution, followed by dropwise addition of 60 ml of methanol solution containing 1.44 g of NaOH. The solution was kept under stirring at a temperature of 60°C for another 30 minutes, and was cooled down subsequently to room temperature to yield a white precipitate of ZnO nanoparticles. They were separated by high-speed centrifugation and were washed thoroughly three times with ethanol and then with acetone. The final product was dried in vacuum at room temperature.

2.2.4 Synthesis of CeO_2 nanoparticles

CeO_2 nanoparticles were synthesized according to following procedure with slight modification. [11,12] Briefly, 7.6 mL of an aqueous solution containing 3.26 g of cerium nitrate hexahydrate and 15 ml aqueous solution of 1.5 g dextran (T-10) were mixed. The prepared solution was added dropwise to 54 mL of NH_4OH solution while stirring for 24 h at 25 °C. After 24 h, particles were centrifuged at 10000 rpm for 10 min to remove any impurities as well as unattached dextran. The particles were further washed three times with water and ethanol. The final product was dried by freeze drying (at -70 °C) for 12 h.

2.3 Material characterization techniques

Several experimental tools used to analyze the characteristic properties of pure MOF and different nanoparticle-MOF composites are summarized below.

2.3.1 Powder X-ray diffraction

Powder X-ray diffraction (PXRD) is a powerful tool for a crystalline material as this technique provides information on phase, purity and structure of a material. A powder may be composed of many small and finely ground crystals, known as crystallites. These crystallites are randomly oriented to one another. All atoms in crystalline materials are considered as sets of parallel crystallographic planes which are characterized by Miller indices (h k l). The X-ray diffraction occurs when the crystallographic planes fulfill conditions for constructive interference and provided by Bragg's law. [13, 14]

$$2dsin\theta = n\lambda \quad ----------2.1$$

Where λ is the wavelength of X-ray beam, *d* is inter planer spacing between two successive crystal planes, θ is the angle between incident beam and the crystallographic plane, and *n* is order of diffraction. In general *n*=1, for first order diffraction as second order peaks are mostly difficult to detect experimentally. X-ray tube is the source of the X-ray beam. The diffracted X-rays are detected by a detector. X-ray tube, detector and the sample are located on the focusing circle. The X-ray tube and detector are placed at the equidistance from the sample holder. The X-ray tube is fixed, and the detector moves along the goniometer circle with an angular speed. During the XRD analysis the detector is always at 2θ angle and the sample surface is always at θ angle with respect to the incident beam. The detector scans around the sample in the

specified 2θ intervals and records the angle and the intensity of diffracted radiation. When θ is changed, maximum intensity peaks are observed if different planes are exposed, otherwise no peak is observed.

Powder X-ray diffraction (PXRD) patterns of all samples prepared in this work were measured at room temperature on Bruker D8 advance and Rigaku (Model: Smart Lab) XRD analyzer using Cu Kα (λ = 1.5406 Å) radiation. Bruker D8 advance was operated at 40 kV and 40 mA and Rigaku analyzer was operated at 45 kV and 112 mA.

2.3.2 Field emission scanning electron microscopy (FESEM)

The FESEM is a scanning electron microscope based technique which employs a highly energetic electron beam to study surface morphology, fractured components, foreign particles etc. In scanning electron microscope (SEM), thermionic emitter is used as electron emission source. In this kind of emitter, filament is heated by electric current and when sufficient amount of heat is generated to overcome the work function of filament material, the electrons are generated. thermionic sources have relatively low brightness and thermal drift may occur during operation. [13] To overcome this problems, Field emission (FE) sources as an election emmision are used in FESEM technique. It is basically a cathode filed emitter placed in large electrical potential gradient to discharge the electrons. The electrons are liberated from FE sources under high vacuum column and accelerated in a high electrical field gradient. The acceleration voltage between cathode (electron gun) and anode is commonly in order of magnitude between 0.5 to 30 kV. In high vacuum column, the electrons are moved without scattering called primary electrons. These primary electrons are focused and deflected by electromagnetic lenses to produce a narrow scan beam that bombards the object. As a result, secondary electrons are

emitted from each spot on the object. The angle and velocity of these secondary electrons relates to the surface structure of the object. An electron detector catches these secondary electrons and produces an electronic signal. This signal is amplified and transformed to a video scan-image that can be seen on a monitor or to a digital image that can be saved and processed further. [13]

The morphologies of synthesized materials in this work were characterized by a FESEM (Make: Zeiss, Model: Sigma) instrument at an accelerating voltage of 2-5 kV. The powder sample was first dispersed in ethanol and then dropped on an aluminum foil, dried under vacuum overnight. The samples were placed on an aluminium stub containing carbon tape and coated with conducting layer of gold using a sputtering unit for 120 seconds before the analysis.

2.3.3 Energy dispersive X-ray spectroscopy (EDX)

EDX is used for elemental analysis or chemical characterization of the sample. The equipment is attached to the FESEM to gather elemental information about the specimen under investigation. It is based on the fact that each element has a unique atomic structure, which emits its unique characteristic X-ray. To stimulate the emission of characteristic X-ray, a high energy beam of electrons or protons is focused on the sample. At rest, an atom of the specimen sample contains ground state electrons in distinct energy levels. The incident beam may excite an electron from inner shell and it results in an electron vacancy in the shell. An electron from outer higher-energy shell fills that vacancy or hole and the difference in energy in between higher energy shell and lower energy shell is released in the form of an X-ray. The atoms of every element releases X-rays with distinctive amount of energy during this process. Thus, by measuring the value of this energy, atoms present in the sample can be identified. In output, an

EDX spectrum is received and can be seen on a monitor or to a digital image. An EDX spectrum shows the peaks corresponding to energy levels for which X-rays has been received. Each of those peak corresponds to an atom and therefore resembles to single specific element. The intensity of those peaks depends on the concentration of the elements present in the specimen. This technique is useful for composition as well as elemental mapping.

In the present thesis, EDX mapping of the samples were done by using FESEM instrument (Make: Zeiss, Model: Sigma) equipped with Oxford Instruments UK, at an accelerating voltage of 20 kV using Aztec software.

2.3.4 Transmission electron microscopy (TEM)

TEM is one of the best characterization tools for nanomaterials in which structural information can be gathered with the help of high resolution imaging and electron diffraction. The high resolution TEM or HRTEM is known for lattice imaging. It provides structural information, crystal defects or dislocations about the sample. Selected area electron diffraction (SAED) provides information about crystal structure (cubic, hexagonal, tetragonal etc.) and crystallinity (like single crystalline, polycrystalline or amorphous). TEM works on the principle of optical projection; when an object is placed in front of a light source, its image is enlarged and the shadow is created on the screens far behind from the object. The TEM consists of an emission source commonly made of tungsten filament or lanthanum hexaboride (LaB_6) crystal. The electron source is connected to a high voltage source. TEM consist of series of electromagnetic lenses to magnify the object. The sample specimen is placed in copper grid of few mm of diameter. The specimen sample must be sufficiently thin (a few tens to a few hundred nm) to transparent of the electrons. The electrons emitted from electron gun accelerated to high voltages in magnitude of 100

to 400 kV. [15] These electrons are converged into a fine beam using electromagnetic lenses. The electromagnetic lenses are named as condenser lenses, the objective lenses, and the projector lenses. The condenser lenses are used to form the primary electron beam, the objective lenses are used to focus the electron beam into the sample and the projector lenses are used to expand the transmitted electron beam from the sample onto the phosphor screen. Structural images are obtained in number of ways. The bright field image is obtained by allowing central electron beam (transmitted beam) passing through sample and excluding all the diffracted beams. It is done by placing suitable sized apertures in the back focal plane of the objective lenses. As un-scattered central beam is selected, the electrons may scatter or absorb by the areas with crystalline or high mass areas (inorganic nanoparticles[16]) of specimen and will appear as dark. In other way, dark field images are obtained by magnifying a single beam of one of the diffracted beams by blocking the central transmitted beam and other diffracted beams. This technique is useful to increase the contrast of the image when bright field image is not enough clear. In a third method of imaging i.e. HRTEM imaging, number of diffracted beams and primary transmitted beam are combined to give an interference image. In SAED analysis, electron beams are diffracting from crystalline material at a particular angle depend on its crystal structure. These diffracted electron beams form a series of spots on the screen. Each spot corresponds to diffraction condition of the sample crystal structure[17]. In addition, single spot SAED pattern represents the appearance of a single crystal and ring like SAED pattern is formed for polycrystalline materials. [17]

The samples for TEM analysis were prepared by drop casting on a carbon coated copper grids of 300 mesh, which were left for overnight for drying. The images were recorded using a JEOL (Model: JEM 2100 and 2100F) instrument with an accelerating voltage of 200 kV. The resolution of lattice images (HRTEM) were improved by using fast Fourier transformation (FFT).

2.3.5 Surface area and pore volume analysis

In 1938, Stephen Brunauer, Paul Hugh Emmett, and Edward Teller (BET) developed a mathematical model to measure the two important attributes of porous materials i.e. surface area and pore volume. [18] The BET method had five major assumptions

- Each adsorption site has equivalent energy (i.e. homogeneous) and can adsorb one molecule of adsorbate to form monolayer
- No lateral interaction between the molecules
- Upper most layer will approximate a liquid phase and is in equilibrium with the vapor phase
- The energy of desorption for each molecule in the first layer at solid surface is equivalent to the heat of adsorption, while for all additional layers, it is the heat of condensation i.e. $E_2=E_3=E_4=\ldots=E_n=E_L$.
- At saturation pressure (i.e. P/P_0 approaches unity), the number of layers becomes infinity.

The resultant BET equation is

$$\frac{1}{V\left[\left(\frac{P_0}{P}\right)-1\right]}=\frac{C-1}{V_mC}\left(\frac{P}{P_0}\right)+\frac{1}{V_mC} \quad ----------2.2$$

Where P and P_0 are equilibrium and saturation pressure of adsorbate at the temperature of adsorption, V is the volume of gas adsorbed at STP, V_m is the monolayer adsorbed quantity, and C is the BET constant,

$$C=exp\left(\frac{E_1-E_L}{RT}\right) \quad ----------2.3$$

Where E_1 is heat of adsorption for the first layer, and E_L is that for second and higher layers and is equal to heat of liquefaction. *R* is the ideal gas constant and *T* is temperature of the adsorption (-196 °C or 77 K)

The experimental data plotted between $\frac{1}{V\left[\left(\frac{P_0}{P}\right)-1\right]}$ vs $\frac{P}{P_0}$ yields a straight line with y- intercept

$$\text{Intercept } I = \frac{1}{V_m C} \quad ---------- \quad 2.4$$

$$\text{Slope } A = \frac{C-1}{V_m C} \quad ---------- \quad 2.5$$

Intercept I and slope A are used to calculate the monolayer adsorbed gas quantity V_m and BET constant C by following equations.

$$V_m = \frac{1}{A+I} \quad ---------- \quad 2.6$$

$$C = 1 + \frac{A}{I} \quad ---------- \quad 2.7$$

The specific BET surface area can be calculated by following formula

$$S_{BET} = \frac{V_m N_a a_m}{m \times 22400} \quad ---------- \quad 2.8$$

Where N_a is Avogadro's number (6.023*10^23 mol^{-1}), a_m is coverage w.r.t. a single adsorbing molecule (0.162 nm^2/N_2 molecule), V_m is the molar volume of adsorbate gas and a_m is the mass of the absorbent. Ideally, 1 mole of probing gas occupies 22.4 L or 22400 cm^3 volume in STP. Typically, N_2 as adsorbate gas (at -196 °C) was used to estimate the BET surface area and pore volume in the present research work. The specific surface area was evaluated in the relative pressure range $\left(\frac{P}{P_0}\right)$ of 0.05-0.25 using the BET model. The total pore volume is calculated in

the relative pressure range of $\left(\frac{P}{P_0}\right) = 0.99$ by Kelvin equation.[19] The micropore volume and external surface area are calculated using *t*-plot method. The statistical film thickness *t* is calculated by following formula. [20]

$$t\ (nm) = \sigma \times \left(\frac{5}{ln\frac{P}{P_0}}\right)^{\frac{1}{3}} \text{----------2.9}$$

Where, σ is film thickness of one layer and it is typically 0.354 nm for N_2.

The BET surface area and pore volume of all the samples were measured in a Autosorb iQ (Make: Quantachrome Instruments, USA) adsorption apparatus equipped with ASiQwin software for data analysis. Prior to the measurement, all powder samples were degassed at 150 °C under high vacuum for 12-14 hours.

2.3.6 Thermo gravimetric analysis (TGA)

TGA is a method of thermal analysis in which changes in physical and chemical properties of materials are measured as a function of temperature (with constant heating rate), or as a function of time (with constant temperature and/or constant mass loss). The instrument contains a high temperature furnace and a precise mass balance. A purge gas stream is passed over the sample and the system temperature is incrementally raised while the change in mass of the material is recorded. The TGA plot (weight loss as a function of temperature) reveals information about the activation and decomposition temperatures of the material. [13]

In the present work, a NETZSCH analyzer (model no. STA449 F3 Jupiter) are used for TGA analysis of pure MOF and nanoparticle-MOF composites. About 10 mg of the sample was

heated at a rate 10 °C min^{-1} over a temperature range of 30–800 °C in the analyzer to obtain the thermogram under an inert atmosphere of N_2 (N_2 flow of about 40 cm^3 min^{-1}).

2.3.7 Fourier transform infrared spectroscopy (FT-IR)

FTIR is an important analytical method to determine the structural bonding information, functional groups present in the solids and on surfaces. The theory behind IR spectroscopy is that the molecules absorb frequencies that are characteristic for their structure. Chemical bonds are not rigid and inflexible entities, but are capable of undergoing series of different vibrations. Every bond has its own characteristic vibrational frequency, the value of which depends upon nature of the bond and its chemical environment. As a result, each bond will absorb infrared radiation (IR) of a characteristic wavelength. The correlation between bond absorptions with their corresponding wavenumbers or wavelengths is the basis for the determination of structural features of the compounds by FT-IR analysis. Bond vibrations may be of several types like asymmetrical and symmetrical stretching as well as in-plane and out-of-plane bending modes. These all vibrational mode are referred to as fundamental vibrations. [21] The interferometer consists of a IR radiation source, beam splitter, a fixed mirror, and a moving mirror etc. An IR source is polychromatic, emitting light over a broad range of wavelengths and frequencies. Each wavelength is represented by a sinusoidal wave. Therefore, the resultant interferogram represents the sum of all sinusoidal waves created from each IR wave. The beam splitter is made of a special material that transmits half of the radiation striking it and reflects the other half. Radiation from the source strikes the beam splitter and separates into two beams. One beam is transmitted through the beam splitter to the fixed mirror and the second is reflected off the beam splitter to the moving mirror. The fixed and moving mirrors reflect the radiation back

to the beam splitter. Again, half of this reflected radiation is transmitted and half is reflected at the beam splitter, resulting in one beam passing to the detector and the second back to the source. An interferogram is made by plotting the light intensity versus optical path difference. But this interferogram cannot be understood directly. This decrypting is done by mathematical technique called Fourier transformation. Fourier algorithm converts the measured interferogram into a plot of intensity versus frequency or wavenumber of the spectrum. [13]

FTIR studies of powder samples were carried out in diffuse reflectance spectroscopy (DRS) mode using Shimadzu IRAffinity-1 spectrometer in 4000-400 cm^{-1} range with a resolution of 4 cm^{-1} for 30 scans. A background scan was also performed initially, using dried KBr powder.

2.3.8 Vibrating sample magnetometer (VSM)

It is widely used to determine magnetic properties of the magnetic materials. Using VSM, one can measure the magnetic moment as a function of temperature, magnetic field and time. So, it allows performing magnetic susceptibility and magnetization studies. The principle of VSM is based on Faraday's law of induction. According to this, an electromotive force (emf) is induced in a conductor or coil when there is change in magnetic flux through the coil. [22] A specimen sample is mounted on long quartz rod in such a way that sample is positioned in between pole pieces of two electromagnets producing uniform magnetic field. As a result, dipole moment will be induced. If the sample vibrates with sinusoidal motion, *i.e.* up and down, with the help of mechanical vibrator, there is a change in magnetic flux. This induces a voltage in the pick-up coils mounted on pole pieces of electromagnet. This voltage is proportional to the magnetic moment of the sample. The various parts of the electromagnets are electromagnets with power

supply, mechanical vibrator with sample holder, pick up coils, hall probe, temperature controller, closed cycle Helium refrigerator, high temperature oven etc. [22]

The magnetic properties (hysteresis loop) of the samples were measured by using a Lakeshore (Model 7410) Vibrating Sample Magnetometer (VSM) at room temperature. The powder samples weighing ~ 10 mg were draped with Teflon tape prior to the VSM analysis. Before performing the measurements, calibration was carried out by measuring the magnetic moment of standard Nickel (Ni) sphere sample. The mechanical vibrator vibrates at a frequency of 80 Hz. The magnetic loop was measured by varying the magnetic field (*H*) up to 1.5 T.

2.4 Drug loading and release experiments

In this work, pure MOF, nanoparticles and nanoparticles-MOF composites were studied as carriers for anticancer drug "Doxorubicin hydrochloride" (henceforth referred as DOX). At first the DOX was loaded to the carriers and later released study was performed in simulated saline solution. The drug concentration is quantified by UV-Visible spectrophotometer. The description related to experimental protocols and instrument are given below.

2.4.1 Drug loading experiments

The DOX loading experiments were performed using the protocol from the literature.[23] At first, the carrier sample was dried at 100 °C for about 4 h to remove the moisture. About 100 mg of this dried carrier was added to 15 ml of 2 mg/ml DOX solution and kept under dark in an orbital shaker at 200 rpm and 25 °C for about 24 h. The sample was recovered in a high speed centrifuge (run at 10,000 rpm for about 10 mins). The concentration of DOX in the supernatant was measured via its absorbance using a UV-Visible spectrophotometer.

The drug loading capacity $\left(q \text{ in } \frac{\text{mg of DOX}}{\text{g of carrier}}\right)$ of the carrier were calculated from the following equations. [23,24]

$$q = \frac{m_0 - m_f}{m_{ads}} \quad ----------2.10$$

where m_0 is the initial amount (mg) of DOX in the solution and m_f is the amount (mg) in the final supernatant, m_{ads} is the mass (g) of the dried carrier used in the experiment.

2.4.2 Release media preparation

The DOX release experiments were carried out in the phosphate buffer saline (PBS) solution of pH 7.4. Typically, for making of 1 L PBS of pH 7.4, following reagents NaCl (8.0 g), KCl (0.2 g), Na_2HPO_4 (1.42 g) and KH_2PO_4 (0.24 g) were dissolved in 800 ml of water. The pH of the solution was about 7.4. Finally, necessary amount of additional water was added to makeup the solution to 1L. [25]

2.4.3 Release of DOX from pure and nanoparticles-MOF composites

The DOX release experiments were carried out by the protocol similar to as described in literature. [23, 26] The drug release behavior of the DOX-carriers was studied by dispersing the composites in ~15 ml of phosphate buffer saline (PBS) of pH 7.4 or 5.0 at 37 °C. All the experiments were carried out in an orbital shaker (Make: Daihan Labtech, Model LSI-3016R) with shaking motion of 200 rpm. The release profile was obtained by measuring the supernatant concentration in the PBS at periodic intervals. At each sampling time, the composites were completely separated from the PBS in a centrifuge at 10,000 rpm for 10 min. An equal volume of fresh PBS was added after each sampling and the release experiment was continued. The

DOX concentration in the sampled supernatant PBS was analyzed using a UV-Visible spectrophotometer.

The specific drug release capacity of carrier, q' in $\frac{\text{mg of DOX}}{\text{g of carrier}}$ is calculated using

$$q' = \frac{m_r}{m_{ads}} \quad ---------- 2.11$$

where, m_r is the total specific (mg) of DOX released in PBS, and m_{ads} is the mass (g) of the dry carrier used for loading DOX.

2.4.4 UV-Vis absorption spectroscopy

The drug loading and release The basic principle of UV-VIS spectroscopy works on the basis where molecules containing π electrons or non-bonding electrons (*n*-electrons) absorb the energy from the incident ultraviolet or visible light and get excited to higher anti-bonding molecular orbitals. The four possible types of transitions are π- π*, *n*- π*, σ-σ* and *n*- σ*.

According to Beer-Lambert law, the absorbance of a solution is directly proportional to the concentration of the absorbing molecules in the solution and the path length. [13] It is given below.

$$A = \text{Log}_{10}\left(\frac{I_0}{I}\right) = \varepsilon \times c \times L \quad ---------- 2.12$$

Where, A is the absorbance, I_0 is the intensity of the incident light, I is the intensity of transmitted light, ε is the molar absorptivity, c is the concentration of absorbing molecules and L is the path length.

The instrumentation part of UV-Vis spectroscopy consists of tungsten filament (for visible measurements, range: 400-1200 nm) and a deuterium arc lamp (for UV measurement, range:190-400 nm) as the radiation source. Instruments automatically swap lamps when scanning between the UV and visible region. The various parts of this instruments are

diffraction grafting unit, wavelength selectors, filters, sample containers, detectors etc. Commercial UV-Vis spectrophotometer are two types i.e. single beam and double beam instrument.

In present thesis, the concentration of drug (Doxorubicin hydrochloride) in liquid phase was evaluated by UV-Vis spectrophotometer at the wavelength of 480 nm using UV-Visible spectrophotometer (Model; Orion AquaMate 8000 and Evolution 201, Thermo Scientific). Quartz cuvettes were used for holding the liquid samples. Prior to all loading and release experiments, calibration curves were made in different liquid media.

References

1. Y-R. Lee, J. Kim and W-S. Ahn, *Korean J. Chem. Eng*., 2013, **30**, 1667-1680.
2. J. Li, Q. Wu and Ji Wu, Synthesis of Nanoparticles via Solvothermal and Hydrothermal Methods, *Handbook of Nanoparticles*, 2015, Springer International Publishing, Switzerland.
3. J. W. Yoon, Y-K. Seo, Y. K. Hwang, J-S. Chang, H. Leclerc, S. Wuttke, P. Bazin, A. Vimont, M. Daturi, E. Bloch, P. L. Llewellyn, C. Serre, P. Horcajada, J-M Grenèche, A. E. Rodrigues and G. Férey, *Angew. Chem. Int. Ed.*, 2010, **49**, 5949–5952.
4. Y-K Seo, J. W. Yoon, J. S. Lee, U-H Lee, Y. K. Hwang, C-H. Jun, P. Horcajada, C. Serre and J-S. Chang, *Microporous Mesoporous Mater*., 2012, **157**, 137-145.
5. R. Massart, *IEEE Trans. Magn*., 1981, **17**, 1247–1248.
6. Z. G. Peng, K. Hidajat and M.S. Uddin, *J. Colloid Interface Sci*., 2004, **271**, 277–283.
7. A. K. Gupta and M. Gupta, *Biomaterials*, 2005, **26**, 3995–4021.
8. T. Ahn, J.H. Kim, H-M. Yang, J.W. Lee and J-D Kim, *J. Phys. Chem. C*, 2012, **116** 6069-6076.
9. S-K. Wang, F. Wang, Y-R Hu, A. R. Stiles, C. Guo and C-Z. Liu, *ACS Appl. Mater. Interfaces*, 2014, **6**, 109–115.
10. C-M. Wu, J. Baltrusaitis, E. G. Gillan and V. H. Grassian, *J. Phys. Chem. C*, 2011, **115**, 10164–10172.
11. E. Alpaslan, H. Yazici, N. H. Golshan, K. S. Ziemer and T. J. Webster, *ACS Biomater. Sci. Eng*., 2015, **1**, 1096-1103.
12. J. M. Perez, A. Asati, S. Nath and C. Kaittanis, *Small*, 2008, **4**, 552-556.
13. S. Zhang, L. Li and A. Kumar, *Materials Characterization Techniques*, 2009,1st edition, CRC Press, USA.
14. C. Kittel, *Introduction to Solid State Physics*, 2004, 8th edition, Wiley & Sons publication, USA.
15. D.K. Schroder, *Semiconductor Material and Device Characterization*, 2005, 3rd edition, Wiley & Sons publication, USA.
16. N. D. Klein, K. R. Hurley, Z. V. Feng and C. L. Haynes, *Anal. Chem*., 2015, **87**, 4356-4362.

17. J. J. Bang, E.A. Trillo and L. E. Murr, *J. Air & Waste Manage. Assoc*., 2003, **53**, 227–236.
18. S. Brunauer, P. H. Emmett and E. Teller, *J. Am. Chem. Soc*., 1938, **60**, 309-319.
19. S. Lowell, J. E. Shields, M.A. Thomas and M. Thommes, *Characterization of Porous solids and Powders: Surface Area, Pore Size and Density*, 2004, 3rd edition, Springer, Netherland.
20. D. D. Do, *Adsorption Analysis: Equlibria and kinetics*, 1998, Imperial college press, London.
21. J. M. Thompson, *Infrared Spectroscopy*, 2018, Pan Stanford Publishing, Singapore.
22. S. Foner, *Rev. Sci. Instrum*., 1959, **30**, 548-557.
23. Y. Zhu, Y. Fang and S. Kaskel, *J. Phys. Chem. C*, 2010, **114**, 16382-16388.
24. A. Chakravarty, K. Bhowmik, G. De and A. Mukherjee, *New J. Chem*., 2015, **39**, 2451–2458.
25. A. D. Eatton, L. S. Clesseri, E. W. Rice and A. E. Greedberg, *Standard methods for the examination of water and wastewater*, 2005, 21st edition.
26. V. Mohanta, G. Madras and S. Patil, *J. Phys. Chem. C*, 2012, **116**, 5333-5341.

Chapter 3

Doxorubicin Loading Capacity of MIL-100(Fe): Effect of Synthesis Conditions

Chapter 3

Doxorubicin Loading Capacity of MIL-100(Fe): Effect of Synthesis Conditions

In this chapter, MIL-100(Fe), an iron based MOFs is chosen as delivery agent for anticancer drug doxorubicin hydrochloride (DOX). Three MIL-100(Fe) carriers were synthesized using different reactants viz. MF (presence of HF), MNF1 (absence of HF and lower water content), MNF2 (absence of HF). It was observed that MNF1 exhibited highest mesoporosity but less crystalline than MF, while MNF2 was amorphous. The mesoporosity contributed to the highest DOX loading exhibited by MNF1. On the other hand, the loaded DOX was easily released from amorphous MNF2, due to the weaker interactions between the drug and the carrier. The results obtained in this work indicate that the synthesis route and pore structure of the carrier play a significant role in the loading and release of DOX from MIL-100(Fe) carriers.

3.1 Synthesis of all the variants of MIL-100(Fe)

MIL-100 (Fe) was successfully synthesized through HF route (henceforth referred as MF) and without HF (henceforth referred as MNF1) following the procedure described in preceding section 2.2.1 (chapter 2). Apart from MF and MNF1, a third variant of the MIL-100(Fe) sample without HF route (henceforth referred as MNF2) was also synthesized describe by Seo et al.[1] About 1.94 g of Fe $(NO_3)_3.9H_2O$, 0.69g of BTC and 24 ml of water were used. The other steps are identical to those in synthesis of MNF1. Synthesis conditions of all the variants are given in **Table 3.1**. The ratio of water to the linker used in synthesis of MF and MNF2 are the same, while that in MNF1 is lower.

Table 3.1: Synthesis conditions of MIL-100(Fe)

Sample	Iron source	HF	HNO_3	Molar composition (Fe : BTC : H_2O)
MF	Iron powder	Yes	Yes	1 : 0.66 : 278
MNF1	$Fe(NO_3)_3.9H_2O$	No	No	1 : 0.66 : 55
MNF2	$Fe(NO_3)_3.9H_2O$	No	No	1 : 0.66 : 278

3.2 Results and discussion

3.2.1 XRD analysis

The powder X-ray diffraction patterns of as prepared MF and MNF MOFs are shown in **Figure 3.1**. Clearly in the absence of the mineralizing agent i.e. HF poorly crystalline phase MIL-100(Fe) is formed, while MF exhibits good crystallinity. It is reported that HF acts as a mineralizing agent to increase the crystallinity of microporous materials and favours the formation of crystalline phases.[1] HF plays an important role in dissolution, crystal nucleation and phase growth. The rate of nucleation and crystal growth are slower while using HF in the reaction and it helps in the crystallization process and decreases the crystal defects. Similar results (high crystalline) using HF as a mineralizing agent were observed in synthesis of zeolite such as ITQ-3, ITQ-4, MFI. [2-4]

In addition, in the absence of HF an amorphous phase (MNF2) is obtained when the ratio of Fe (and the linker) to water in the reacting mixture was same as in the case of MF. However, as the ratio of these components to water in the reaction mixture increased (MNF1)**,** slightly improved crystallinity was obtained even in the absence of HF. [1]

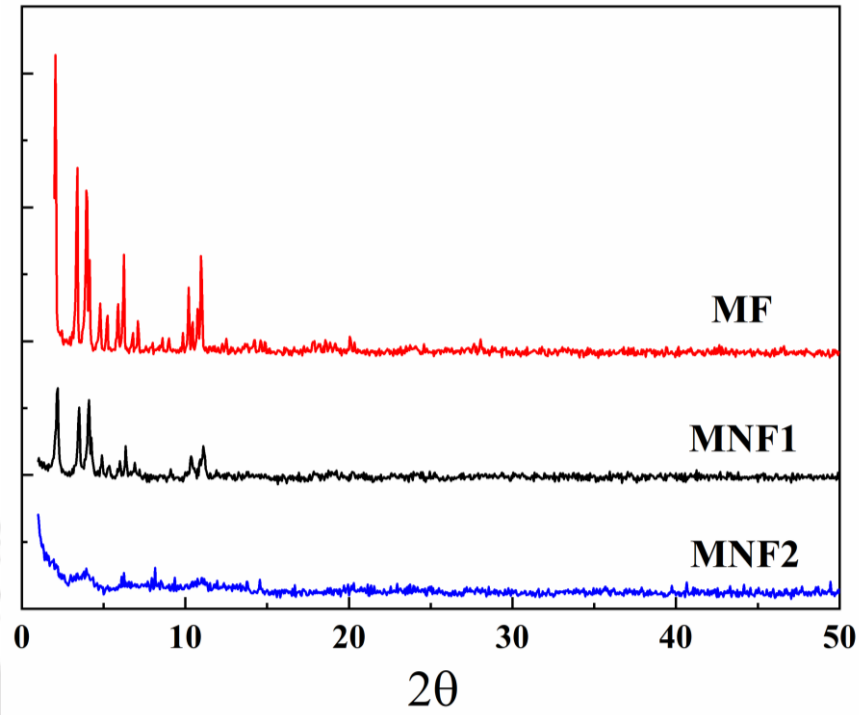

Figure 3.1: X-Ray diffraction data of MF, MNF1 and MNF2

3.2.2 FESEM and EDX mapping analysis

The FESEM images of the three materials are shown in **Figure 3.2**. In the case of MF, a well faceted octahedral morphology with a distribution of particle sizes was observed. However, in the case of amorphous MNF2, the particles aggregate, although and do not exhibit any specific morphological shape. [5] In addition, The elemental mapping (shown in **Figure 3.3**) obtained from EDX analysis indicates that C, O and Fe are uniformly distributed in case of all synthesized MOFs.

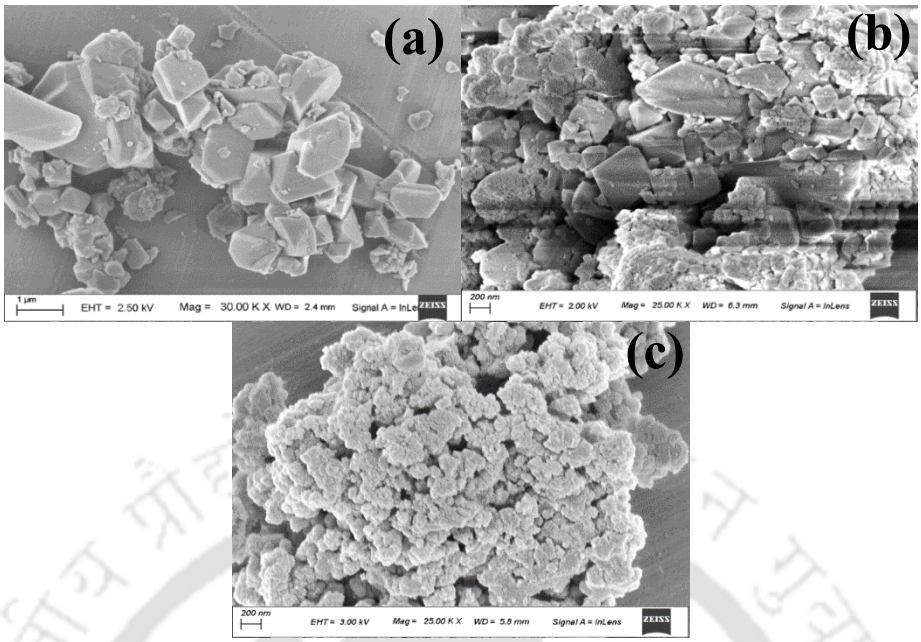

Figure 3.2: FESEM images of (a) MF, (b) MNF1, (c) MNF2

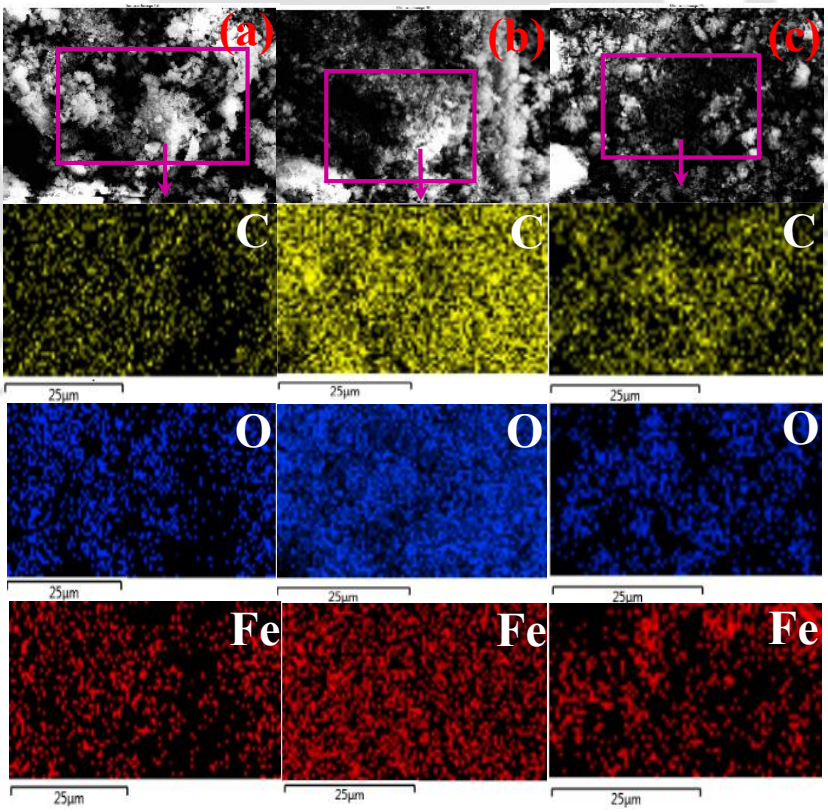

Figure 3.3: EDX mapping images of (a) MF, (b) MNF1, (c) MNF2

3.2.3 N_2 adsorption-desorption analysis

N_2 adsorption-desorption isotherms of MF, MNF1, and MNF2 are shown in **Figure 3.4** and corresponding surface areas and pore volumes are given in **Table 3.2.** The adsorption isotherm of MF follows type I indicating a large micropore volume fraction [6]; however, the materials MNF1, and MNF2 exhibit type IV isotherms with a hysteresis loop [5], indicating presence of mesopore volume. The total pore volume of MF ad MNF1 were comparable, whereas it is somewhat lower for amorphous MNF2.

The micro pore volume (V_{micro}) was evaluated by the *t*-plot method and mesopore volume was calculated from the difference of V_t and V_{micro}. The mesoporous volume (V_{meso}) is significantly higher for MNF1, and MNF2 compared to that of MF. Clearly, large amount of mesopores are created in the structure when HF is not used in the synthesis. Moreover, the MIL-100(Fe) synthesized in a dilute reaction mixture i.e. MNF2 exhibits lower meso and micropore volumes compared to MNF1. The effect of these pore volumes on the drug loading will be discussed later.

Table 3.2: Surface area and pore volumes of MIL-100(Fe)

Sample	**S_{BET} (m^2g^{-1})**	**S_{EXT} (m^2g^{-1})**	**V_t (cm^3g^{-1})**	**V_{micro} (cm^3g^{-1})**	**V_{meso} (cm^3g^{-1})**
MF	2354	27.7	1.2	1.15	0.05
MNF1	1633	120.5	1.3	0.78	0.52
MNF2	1304	118.8	1.0	0.62	0.38

S_{BET}: Surface area calculated by BET Method, S_{EXT}: External surface area, V_t: Total pore volume, V_{micro}: Micropore volume, V_{meso}: Mesopore volume

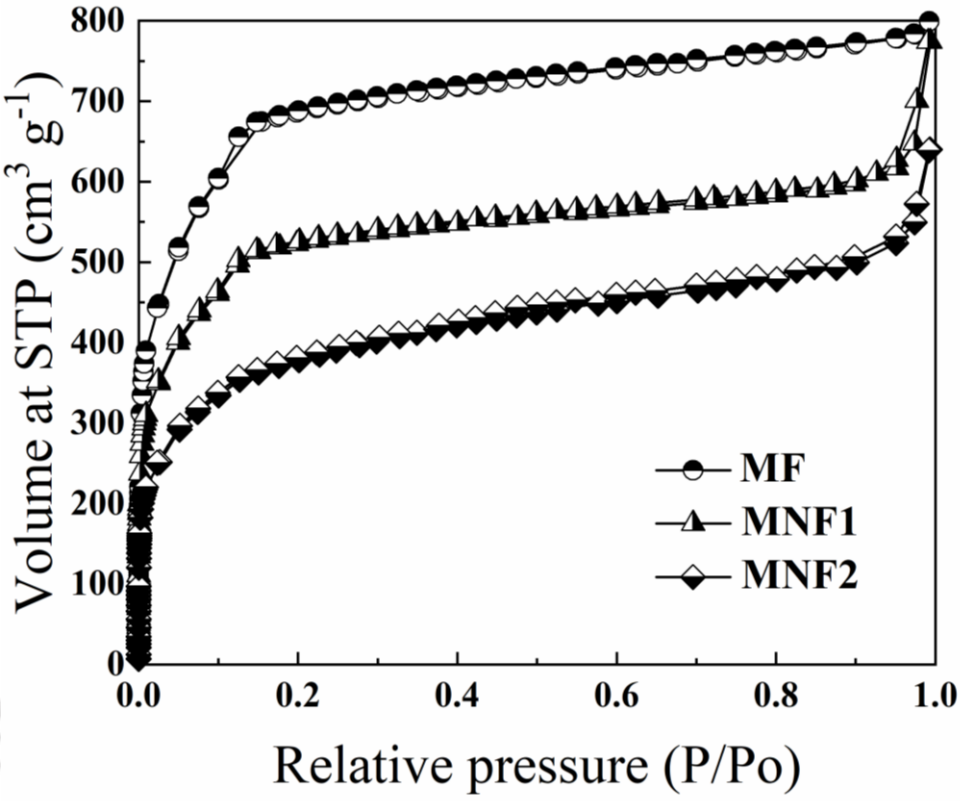

Figure 3.4: N_2 adsorption-desorption isotherms of MF, MNF1 and MNF2

3.2.4 FT-IR analysis

Figure 3.5 displays the FTIR spectra of MF, MNF1, and MNF2**.** The bands at 711 and 760 cm^{-1} appear due to C-H stretching vibrations. The existence of peaks at 1378 cm^{-1} and 1456 cm^{-1} appear due to for C-O vibrations and the O-H bending respectively. The stretching vibration of C=O is found around 1622 cm^{-1}. The appearance of these characteristic bands match with previous reports for MIL-100(Fe). [7, 8]

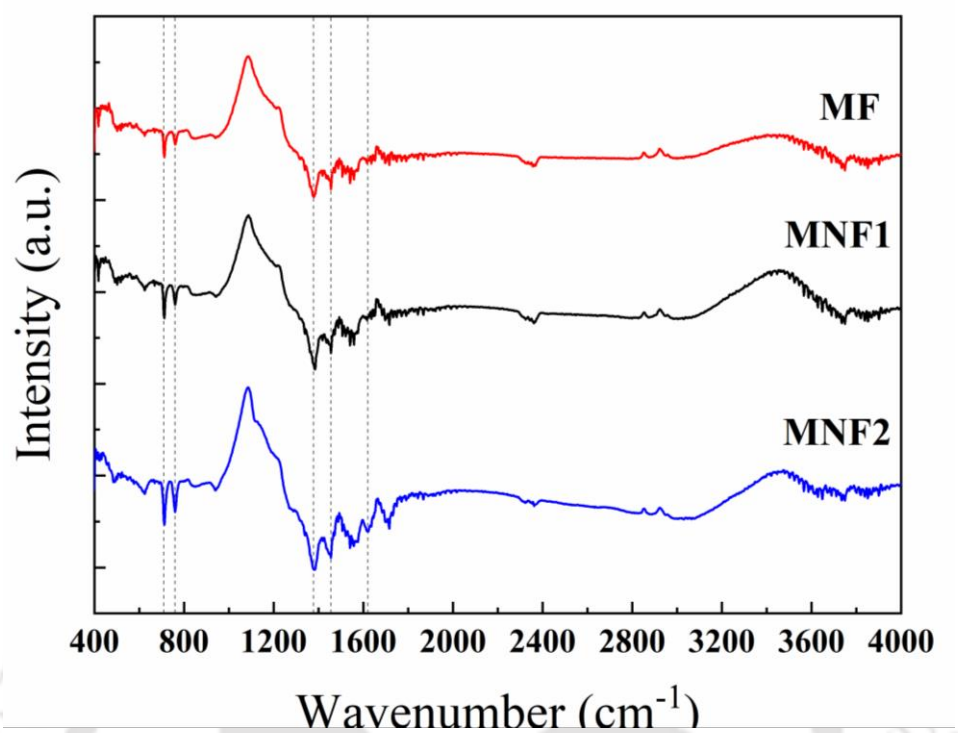

Figure 3.5: FTIR spectra of MF, MNF1 and MNF2

3.2.5 TGA analysis

The thermal stability of the samples was studied over the temperature range of 30-800 ºC and is shown in **Figure 3.6**. In the first and second segments (30-350 °C), the weight loss is due to adsorbed water and other solvents (such as ethanol) used in synthesis procedure. The total losses are around 33.8%, 31.3% and 24.4% for MF, MNF1 and MNF2 respectively. Since MF is more microporous compared to the other two samples more bound water possibly present in the frameworks leads to highest weight loss in first two segments. The third major loss in the range of 350–550 °C (about ~27 wt% for all the three samples) is due to the partial collapse of MIL-100(Fe) frameworks. The fourth loss in the range of 550–800 °C is due to complete decay of organic linker in the frameworks. [8]

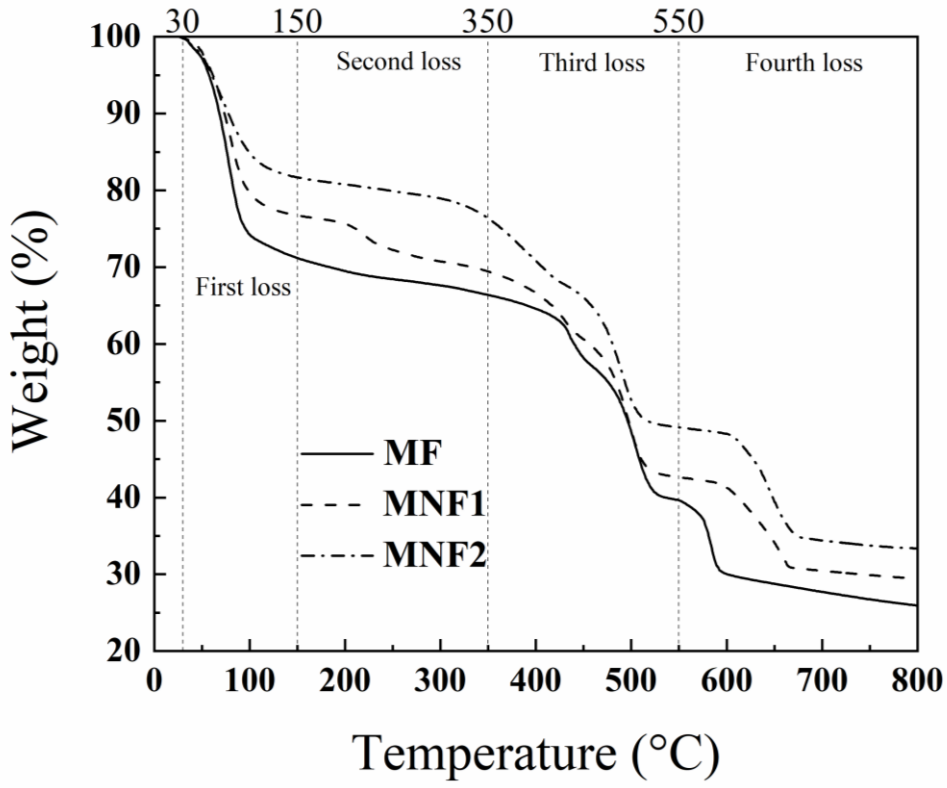

Figure 3.6: TGA curves of MF, MNF1 and MNF2

3.2.6 DOX loading

The loading capacity of MF, MNF1 and MNF2 for DOX are shown in **Figure 3.7**. MF has a DOX loading capacity of 107 mg/g; this is comparable to the results obtained by Horcajada et al. (85 mg/g).[9] On the other hand, the DOX loading capacity of the both MNF1 and MNF2 are significantly higher; in fact, the loading capacity for MNF1 is about 2.2 times that of MF. Higher mesopore volumes in MNF1 and MNF2 contribute to this increase in drug loading. For larger molecules such as DOX, mesopore volume plays an important role in the loading capacity. The DOX loading

capacities of MNF1 and MNF2 are comparable to other porous carriers such as silica coated $NaYF_4$: Yb/Er (174 mg/g), and TiO_2-PLA sphere (100-180 mg/g of carrier), etc.[10, 11]

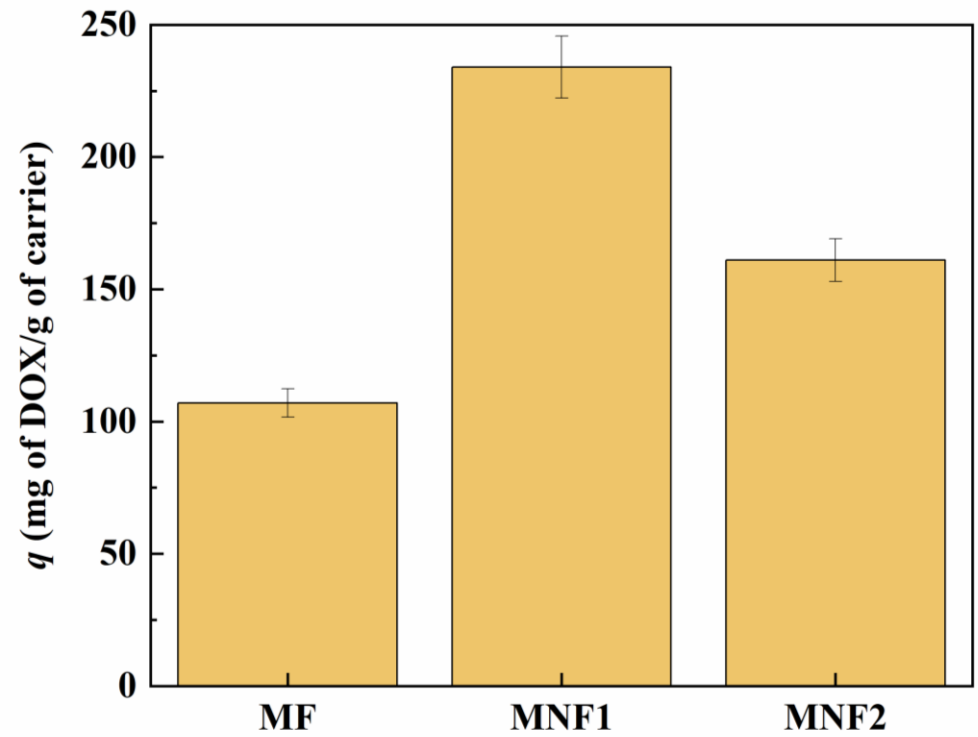

Figure 3.7: DOX loading of MF, MNF1 and MNF2

3.2.7 DOX release study

The specific DOX release capacity for all the carriers is shown in **Figure 3.8**. MF releases about 30 mg of DOX/g of carrier in first 10 days. MNF1 has higher DOX loading capacity and one would expect it to have higher specific release capacity; it releases about 51 mg of DOX/g of carrier, over the same period. On the other hand, MNF2 releases about 53 mg of DOX/g of carrier over the first 10-day period, although it has lower DOX loading capacity compared to MNF1. The amorphous and disordered mesopores of MNF2 have lower affinity for DOX and thereby the release is faster.

By about 30 days, the specific DOX released by MNF2 is about 6.6 % higher, although its loading capacity was about 31 % lower than that of MNF1**.**

The release rate for MF decreases after about 4 days and thereafter at 15 days; in fact, from 15 to 30 days, the specific drug released changes only from 36.7 to 38.7 mg of DOX/g of carrier. In case of MNF1 and MNF2 a faster drug release pattern is noted for first 2 days as compared to MF**;** this may be due to weaker interaction of the carrier with DOX within the mesopores. In addition, after about 9 days the release from MNF2 significantly slows down as compared to that in amorphous MNF1. The difference in the pore structures (and thereby interaction with DOX) of the two carriers results in this behaviour.

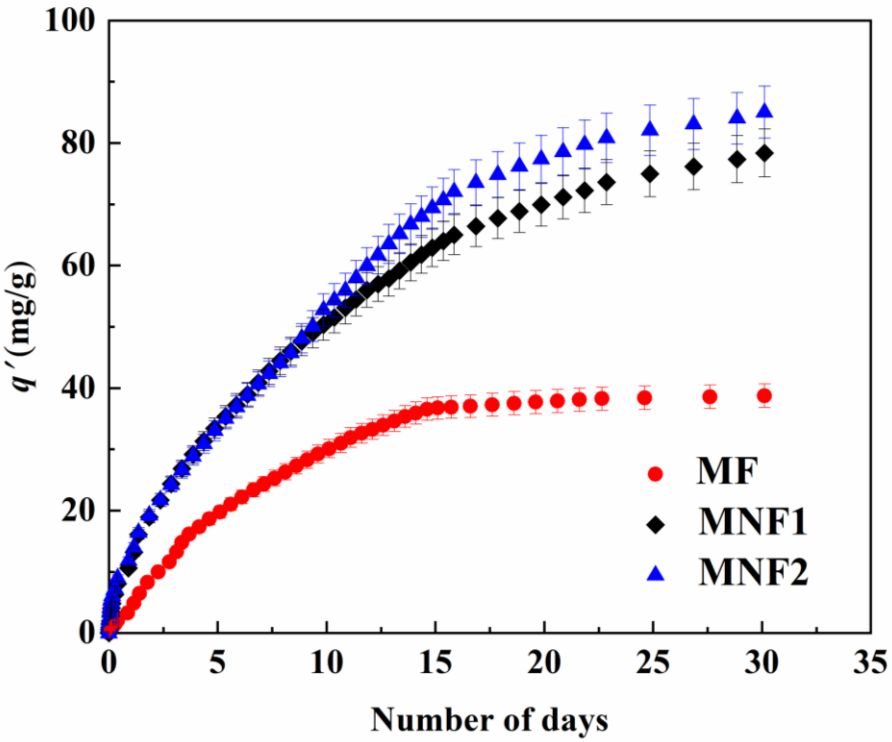

Figure 3.8: Specific DOX release capacity of MF, MNF1 and MNF2

3.3 Summary

In this chapter, three different variants of MIL-100(Fe) MOF i.e. MF (presence of HF), MNF1 (absence of HF and lower water content), MNF2 (absence of HF) were prepared. These materials were characterized by different characterization techniques. MNF2 was slightly amorphous without any specific morphological shape among these three variants. The highest mesopore volume was found (0.52 cm^3g^{-1}) for MNF1. Among these carriers, DOX loading capacity was found maximum for MNF1. However, highest amount of DOX was released from the amorphous MNF2 over a span of 30 days.

References

1. Y-K Seo, J. W. Yoon, J. S. Lee, U-H Lee, Y. K. Hwang, C-H. Jun, P. Horcajada, C. Serre and J-S. Chang, *Microporous Mesoporous Mater*., 2012, **157**, 137-145.
2. T. Zhao, F. Jeremias, I. Boldog, B. Nguyen, S. K. Henninger and C. Janiak, *Dalton Trans*., 2015, **44**, 16791-16801.
3. L. Ge, L. Yuan, K. Huang, W. Feng, H. Fang and S. Feng, *New J. Chem*., 2015, **39**, 5080-5083.
4. T. Loiseau and G. Férey, *J. Fluorine Chem.*, 2007, **128**, 413-422.
5. Y. Fang, J. Wen, G. Zeng, F. Jia, S. Zhang, Z. Peng and H. Zhang, *Chem. Eng. J*., 2018, **337**, 532-540.
6. Y-K. Seo, J. W. Yoon, J. S. Lee, Y. K. Hwang, Cl-H. Jun, J-S. Chang, S. Wuttke, P. Bazin, A. Vimont, M. Daturi, S. Bourrelly, P. L. Llewellyn, P. Horcajada, C. Serre and G. Férey, *Adv. Mater*., 2012, **24**, 806-810.
7. F. Tan, M. Liu, K. Li, Y. Wang, J. Wang, X. Guo, G. Zhang and C. Song, *Chem. Eng. J*., 2015, **281**, 360-367.
8. S. Huang, K-L. Yang, X-F. Liu, H. Pan, H. Zhang and S. Yang, *RSC Adv*., 2017, **7**, 5621-5627.
9. P. Horcajada, T.Chalati, C. Serre, B. Gillet, C. Sebrie, T.Baati, J. Eubank, D.Heurtaux, P. Clayette, C. Kreuz, J. Chang, Y. Hwang, V. Marsaud, P. Bories, L. Cynober, S. Gil, G. Férey, P. Couvreur and R. Gref, *Nat. Mater*., 2010, **09**, 172-178.
10. K. L. Reddy, P. K. Sharma, A. Singh, A. Kumar, K. R. Shankar, Y. Singh, N. Garg and V. Krishnan, *Mater. Sci. Eng. C*, 2019, **96**, 86-95.
11. J. Hou, C. Guo, Y. Shid, E. Liu, W. Dong, B. Yu, S. Liu and J. Gong, *Int. J. Pharm*., 2017, **533**, 73-83.

Chapter 4

Fe_3O_4 promoted MIL-100(Fe) for the controlled release of doxorubicin hydrochloride

Fe_3O_4 promoted MIL-100(Fe) for the controlled release of doxorubicin hydrochloride

In this chapter, a metal-organic framework MIL-100(Fe) and its composite with Iron oxide nanoparticles Fe_3O_4@MIL-100 were investigated as delivery agents for anticancer drug doxorubicin hydrochloride (DOX). A series of composites with varying amounts of Fe_3O_4 were synthesized by adding different amount of Fe_3O_4 to the solvent mixture used for synthesis of the MOF MIL-100. The composites were characterized by various techniques like BET, TEM, FESEM, VSM and TGA to understand the effect of the nanoparticles in the MOF structure. The MOF and several Fe_3O_4@MIL-100 composites were then analyzed used to load the drug by equilibrating aqueous solution of DOX with the porous carriers. The synthesis procedures and the results are reported in subsequent sections.

4.1 Synthesis of pure MIL-100(Fe) and Fe_3O_4

MIL-100 (Fe) was successfully synthesized through HF route (henceforth referred as MF) by hydrothermal method following the procedure described in preceding section 2.2.1 (chapter 2). The description of Fe_3O_4 nanoparticles (henceforth referred as F) synthesis was given in the section 2.2.2 (chapter 2).

4.2 Synthesis of Fe_3O_4@MIL-100(Fe) composites

The synthesis procedure for Fe_3O_4@ MIL-100(Fe) (henceforth referred as Fw-MF) composites was similar to that of pure MIL-100(Fe) MOF. However, the reaction mixture in this case additionally includes a known amount of Fe_3O_4 nanoparticles. This procedure was similar to that described for composites M-DUT-4, M-DUT-5, M-HKUST-1[1] and for Fe_3O_4@ MIL-101(Cr).[2] For example, Fw-MF was prepared by adding 0.27 g of iron powder, 0.675 g of BTC, 0.17 ml of HF, 0.13 ml of HNO_3 to 24 ml of water. The mixture was thoroughly sonicated for 1 h. Then, w (g) of Fe_3O_4 nanoparticles were added to this mixture and loaded in a Teflon lined autoclave reactor. The remaining steps including the purification procedure were identical to that of MF synthesis. Several composites with w = 50, 100, 125, 150 200 and 400 were synthesized following the procedure described above.

4.3 Results and discussion

4.3.1 FESEM analysis

Figure 4.1 provides morphological information regarding pure MF and its composites. The well-faceted octahedron or polyhedron morphology is observed in case of sample MF (**Figure 4.1a**).[3] In the case of composites, Similar morphological features are seen with addition of nanoparticles in case of composites F100-MF and F400-MF.

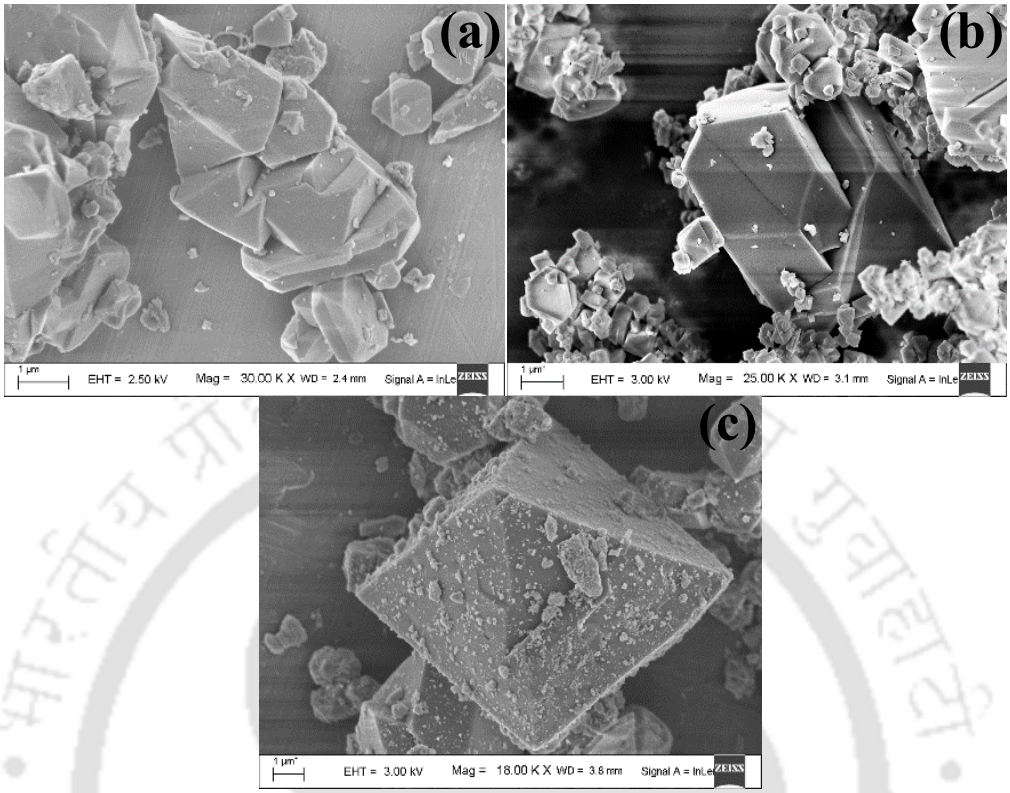

Figure 4.1: FESEM images of (a) MF, (b) F100-MF (c) F400-MF

4.3.2 TEM and SAED analysis

The TEM micrograph of as synthesized F particles are shown in **Figure 4.2a**. The diameter of these magnetic particles are in the range of 10-20 nm. **Figure 4.2b** represents is the image for pure MF. The micro-structural information about Fw-MF composites can be describe from **Figure 4.2c -4.2h**. In these figures, the small darker circular areas of higher electron density correspond to F particles, whereas brighter areas represent the MF matrix (as explained later through the SAED patterns). One can clearly observe that the F particles tend to agglomerate, particularly at higher loadings as in the case of F200-MF and F400-MF (**Figure 4.2g and 4.2h**). In addition, the SAED patterns of pure and composite materials were studied. In case of F, a

distinct SAED pattern was seen (**Figure 4.3a**), but no pattern was found for pure MF (**Figure 4.3b**). In case of composites, a clear diffraction pattern was observed for the darker areas, and while no pattern was seen for the brighter areas (depicted in **Figure 4.3c-4.3n**). These SAED patterns of darker areas unambiguously indicate that they correspond to the F nanoparticles in the composites.

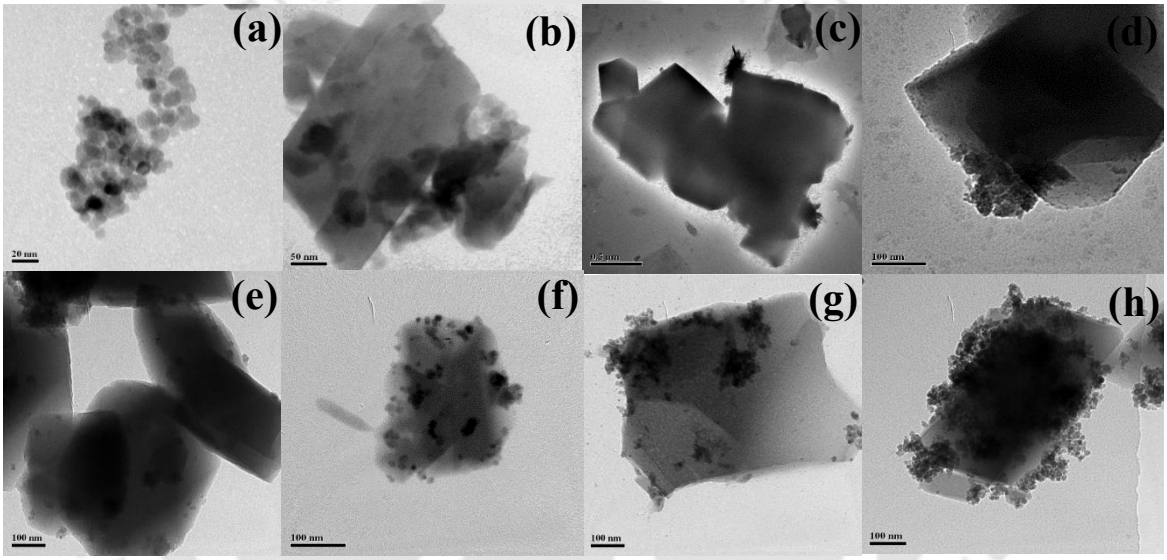

Figure 4.2: TEM images of (a) F, (b) MF, (c) F50-MF, (d) F100-MF, (e) F125-MF, (f) F150-MF, (g) F200-MF, and (h) F400-MF

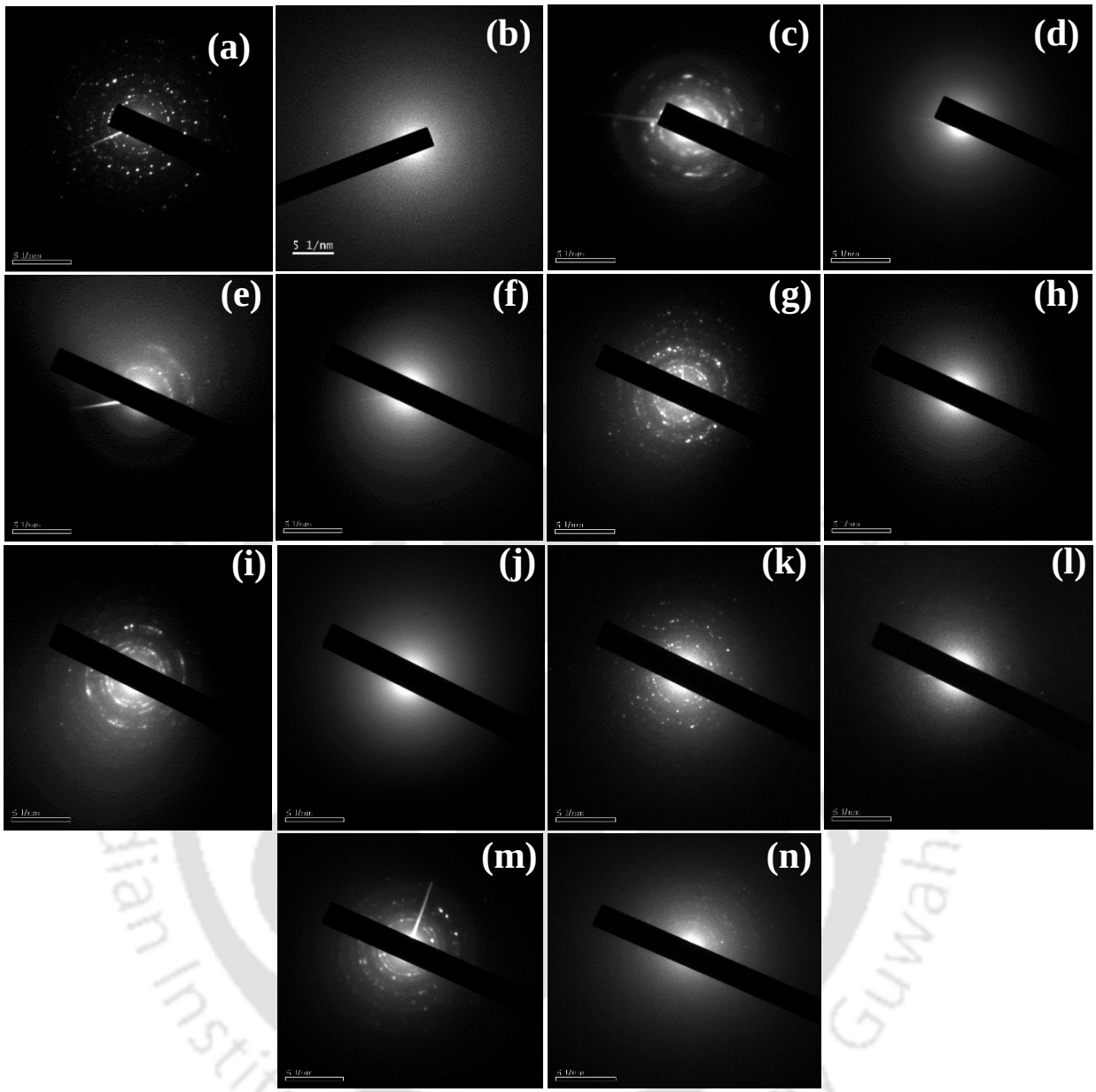

Figure 4.3: SAED patterns of (a) F, (b) MF, (c) F50-MF darker area, (d) F50-MF brighter area, (e) F100-MF darker area, (f) F100-MF brighter area, (g) F125-MF darker area, (h) F125-MF brighter area, (i) F150-MF darker area, (j) F150-MF brighter area, (k) F200-MF darker area, (l) F200-MF brighter area, (m) F400-MF darker area, and (n) F400-MF brighter area

4.3.3 XRD analysis

The powder X-ray diffraction patterns of as prepared Fw-MF composites are compared to the bare nanoparticle F and MF shown in **Figure 4.4**. The PXRD for pure Fe_3O_4 depicts five characteristic peaks at 2θ of 30.3, 35.6, 43.3, 57.3 and 62.8° corresponds to the crystalline planes of (2 2 0), (3 1 1), (4 0 0), (5 1 1), and (4 4 0), respectively. These peaks are consistent for magnetite phase and also matched with the literature.[4] In PXRD patterns of Fw-MF composites no significant peak for Fe_3O_4 particles is found. In addition, the crystallinity of MF is unaffected for all the composites. The amount of nanoparticles present in the composite frameworks is quite low as compared to MF and may be the reason for the absence of the characteristic peaks corresponding to F.

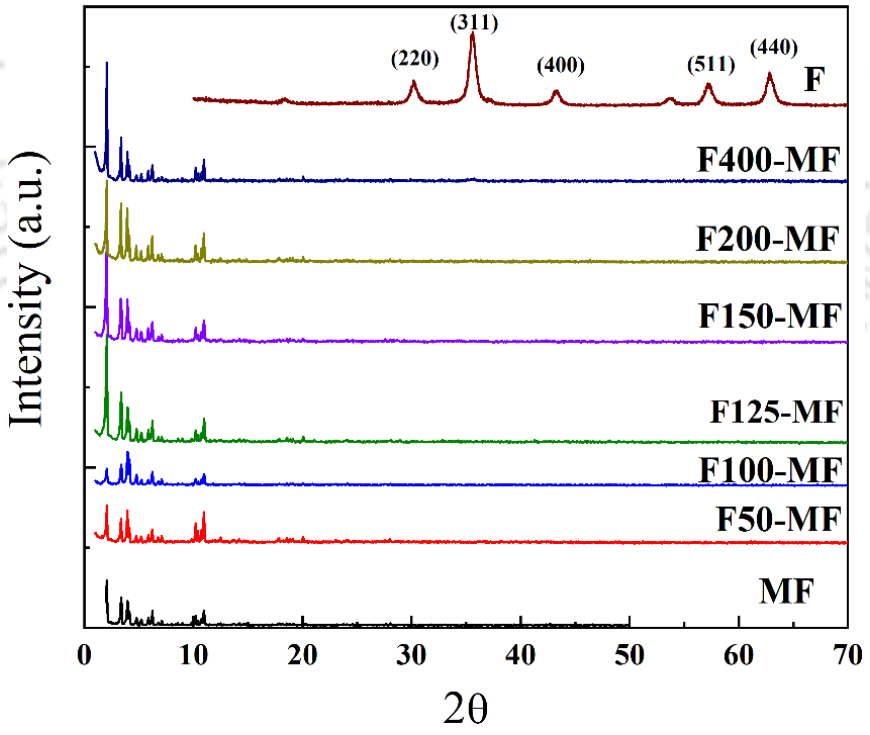

Figure 4.4: X-Ray diffraction data of F, MF and Fw-MF composites

However, in cases of higher Fe_3O_4 composition some characteristic peaks corresponding to nanoparticles can be observed (**Figure 4.5**). For example, in F200-MF**,** the peak at 2θ of 35.6° corresponding to (3 1 1) crystalline plane and in F400-MF peaks at 2θ of 35.6° and 57.5° corresponding to (3 1 1) and (5 1 1) crystalline planes can be seen.

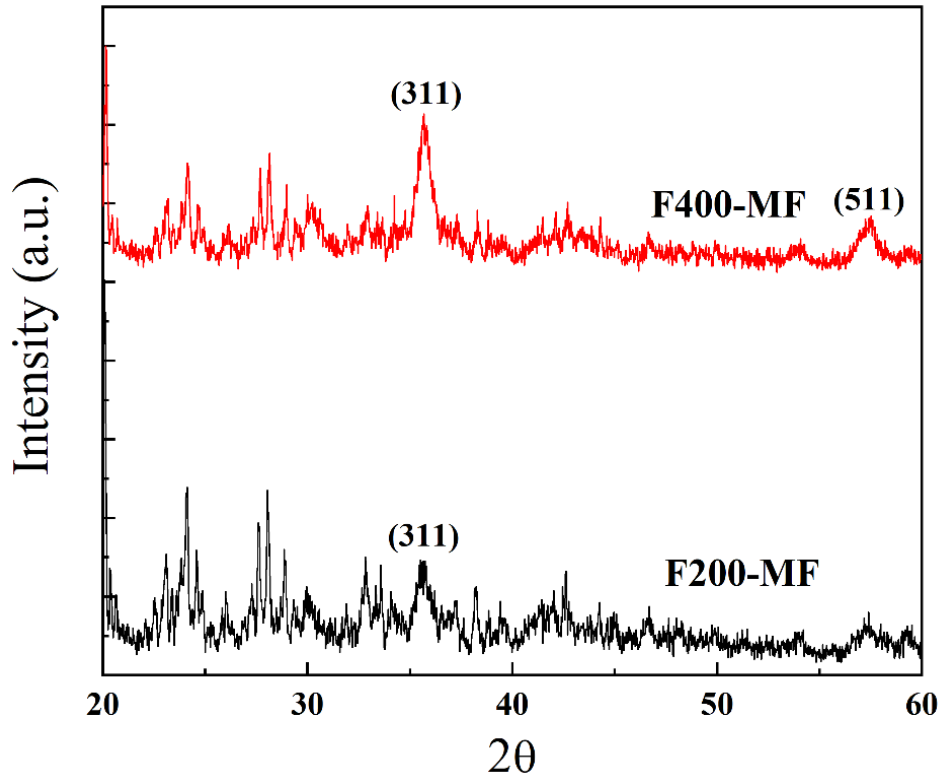

Figure 4.5: X-Ray diffraction data of F200-MF and F400-MF

4.3.4 TGA analysis

The thermal stability of pure F, MF and Fw-MF composites were studied over the temperature range of 50-700 °C and is shown in **Figure 4.6**. Inorganic F particles are very stable up to 700 °C and lose about 5 wt% due to release of free water molecules.[5] However, the weight loss for pure MF and Fw-MF composites is significantly higher.

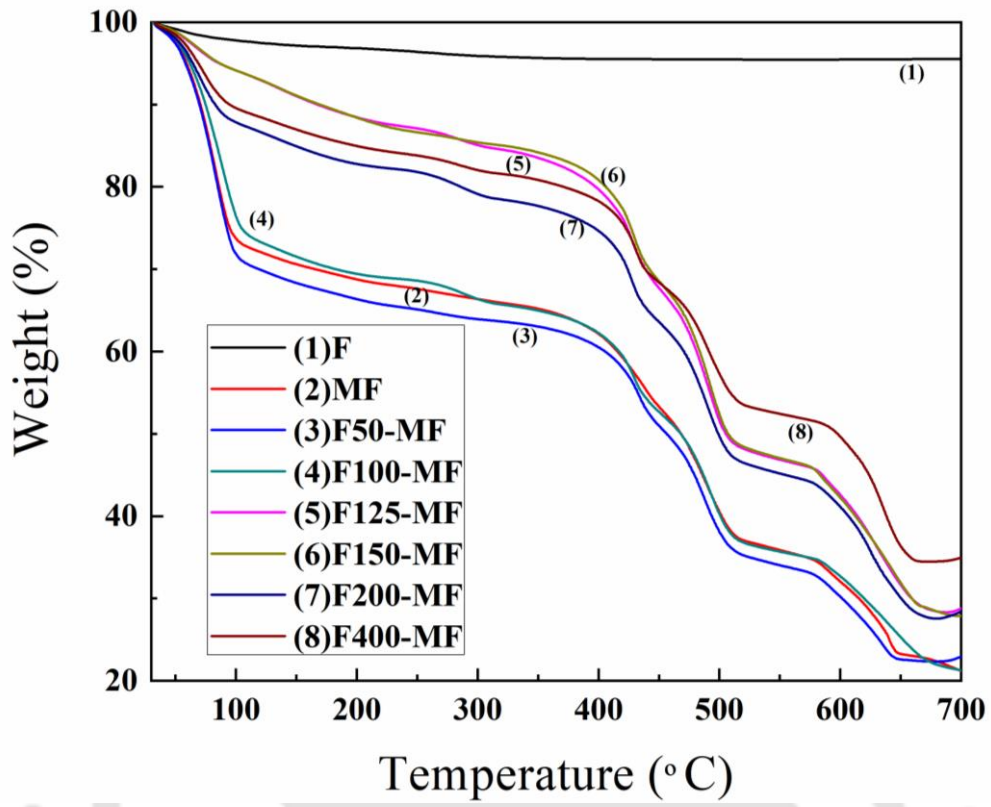

Figure 4.6: TGA curves of F, MF and Fw-MF composites

In case of MF, the first weight loss step corresponding to release of free water is observed at about 80 °C; in between 80-150 °C the bound water is also released. The second gradual weight loss in the temperature range of 150-350 °C is due to release of water interrelated with the iron metal trimers and the solvents used during MOF synthesis. The third major weight loss in the range of 350-650 °C (about 42 wt%) is due to decomposition of the organic linker. [6] Similar TG patterns were observed for F50-MF and F100-MF composites. As the amount of nanoparticles in the composites increases, the weight loss decreases in case of F125-MF to F400-MF in the range of 30-150 °C; although the weight loss trend in the temperature range of 350-650 °C for the F125-MF to F400-MF composites are similar to that of pure MF.

4.3.5 N_2 adsorption-desorption analysis

N_2 adsorption-desorption isotherms curves for pure F, MF and Fw-MF composites are shown in **Figure 4.7**. The adsorption isotherm for pure MF follows type I [7,8] whereas pure Fe_3O_4 nanoparticles (F) follow type IV isotherm with hysteresis loop, representing the mesoporous cages present in the material. Similar N_2 adsorption-desorption isotherms at 77 K are reported for F in earlier literature.[9] The Fw-MF composites exhibit nitrogen adsorption-desorption isotherms similar to that of MF. The composition of the various Fw-MF composites with respective surface area and pore volume are given in **Table 4.1**.

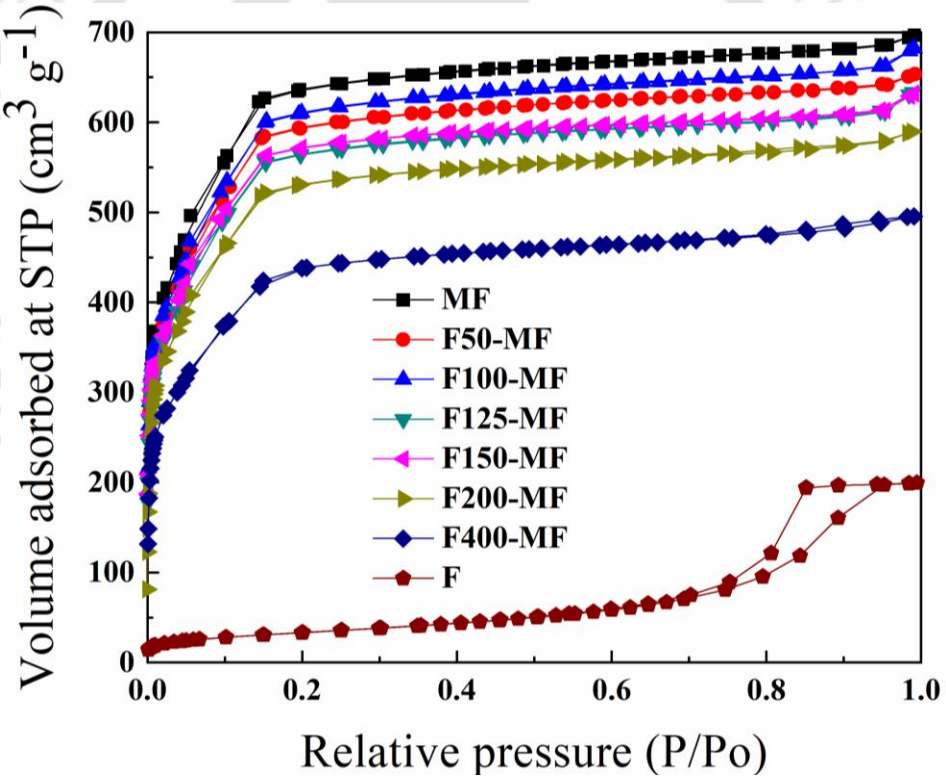

Figure 4.7: N_2 adsorption-desorption isotherms of as synthesized F, MF and Fw-MF composites

Table 4.1: Surface area and pore volumes of Fw-MF composites

Sr. No.	Sample	Mass fraction of Fe_3O_4 , x	S_{BET} ($m^2 g^{-1}$)	V_t ($cm^3 g^{-1}$)
01	MF	0.0	2054	1.08
02	F	1.0	118	0.31
03	F50-MF	0.08	1979	1.01
04	F100-MF	0.11	1935	1.00
05	F125-MF	0.16	1782	0.98
06	F150-MF	0.18	1805	0.98
07	F200-MF	0.22	1674	0.91
08	F400-MF	0.37	1397	0.77

S_{BET}: Surface area by BET Method, V_t: Total pore volume

The surface area (S_{BET}) of pure material MF is 2054 m^2g^{-1}, similar to previously reported literature [7]; on the other hand, S_{BET} of pure F is 118 m^2g^{-1} comparable to earlier reported literature of Fe_3O_4nanoparticles.[9] The BET surface area and total pore volume of the Fw-MF composites exhibit almost linear dependency with the fraction of magnetic nanoparticles (F) present in the composites and is shown in **Figure 4.8**. Typically, Fe_3O_4 mass fraction (x) in the composites is calculated by following formula.

$$x = \frac{w}{y} - - - - - - - 4.1$$

where, y is the yield (g) of the Fw-MF composites from the synthesis and w is the amount (g) of Fe_3O_4 nanoparticles added to each batch of synthesis.

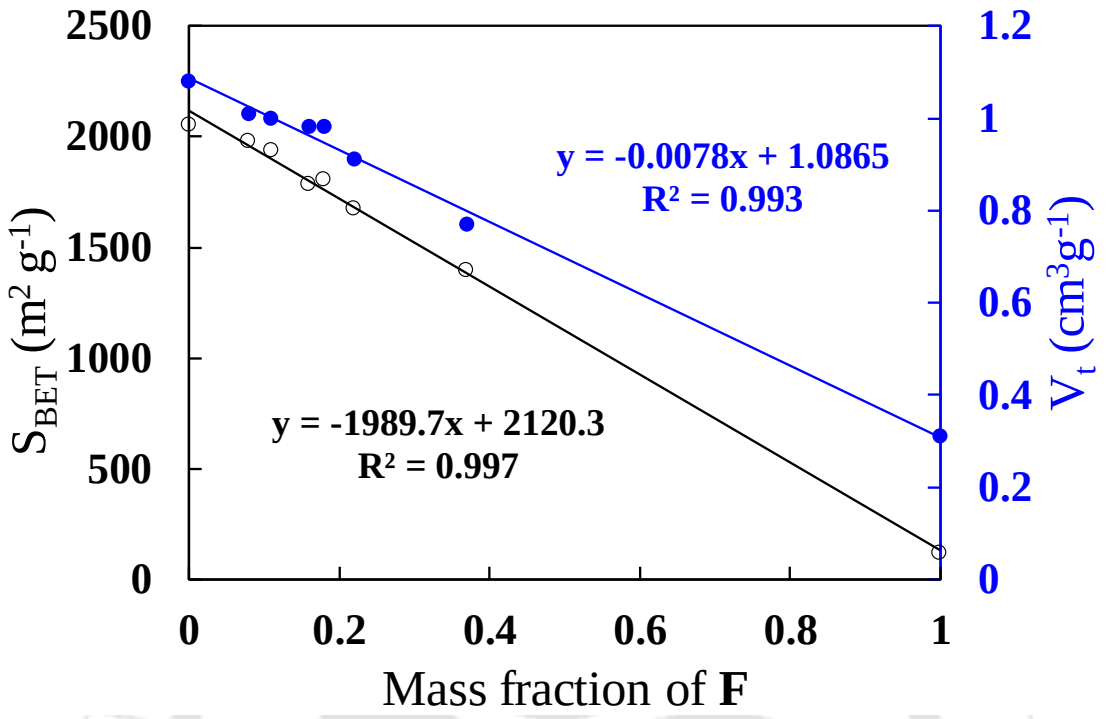

Figure 4.8: Variation of surface area and pore volume of the Fw-MF composites with the mass fraction of Fe_3O_4

4.3.6 VSM analysis

The magnetic properties of as synthesized materials were studied at room temperature in the field range of -15 to +15 kOe; the results are shown in **Figure 4.9**. Pure material MF has negligible magnetic moment (0.20 emu/g with zero remanence). As is to be expected, the magnetic moment of the composites increase, with the increase in the amount of F nanoparticles in the MOF matrix. The composites F200-MF and F400-MF exhibit moment of 5.56 and 12.20 emu/g, respectively due to significant presence of F in these composites. The magnetization for bare F nanoparticles is 68.53 emu/g (inset), lower than that of bulk Fe_3O_4 (92 emu/g).[10] In the case of nanoparticles due to their large surface area to volume ratio magnetic anisotropy energy

becomes comparable to the thermal energy and the induced thermal fluctuations can reduce the magnetic moment significantly in a given field. [10,11]

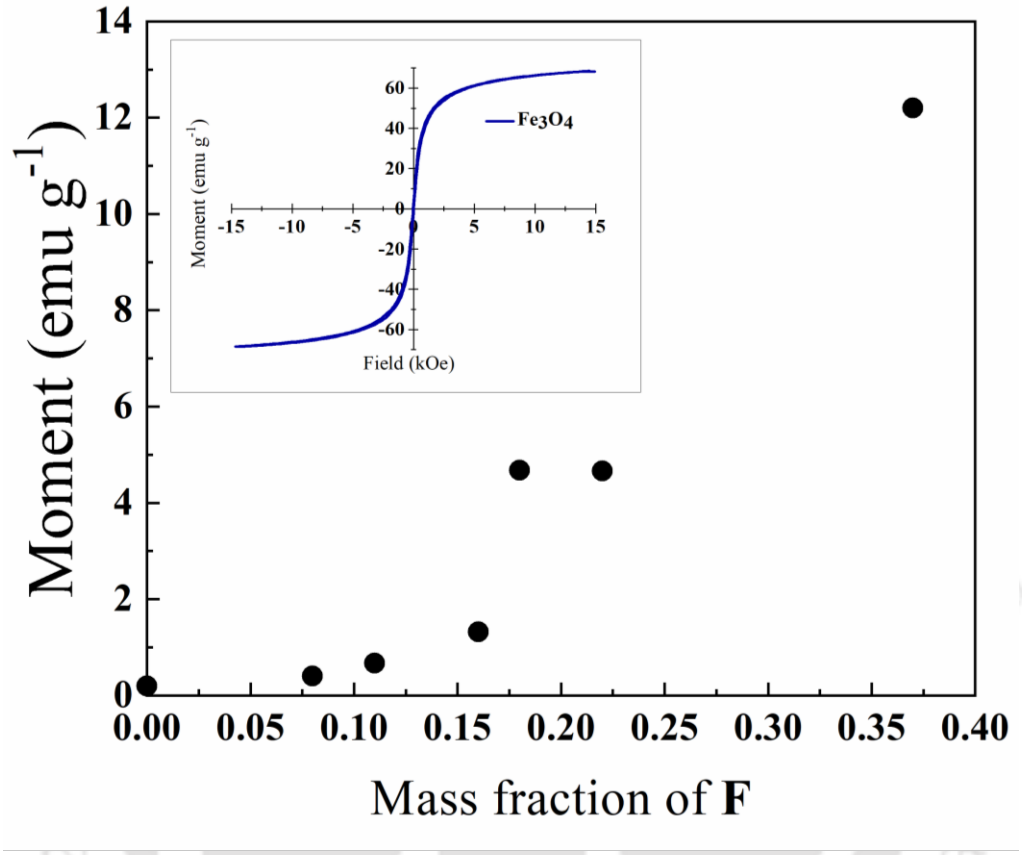

Figure 4.9: Variation of the magnetic moment of the Fw-MF composites with the mass fraction of Fe_3O_4; (inset) M-H curve for Fe_3O_4.

4.3.7 DOX loading

The loading capacity of pure and different Fw-MF carriers are given in **Figure 4.10**. The drug loading capacities of pure F and MF are almost similar i.e. 110 and 107 mg/g, respectively. It is interesting to note that in case of the composites the drug loading capacity are higher than that of both the pure MOF and the pure nanoparticles. The presence of nanoparticles in the composites even at low amounts, significantly increases their loading capacity for DOX from

107 mg/g (for MF) to 180 mg/g (for F50-MF). As more F is introduced in the frameworks the DOX loading capacity increases further; the maximum loading capacity is 194 mg for F125-MF composite which have 0.16 mass fraction of nanoparticles. This increase may be attributed to the synergistic effect wherein the presence of the nanoparticles enhances the interaction of DOX with the MOF framework. Further increase the nanoparticle content in the framework in case of composites F150-MF through F400-MF resulted in a decrease of DOX loading probably due to blocking of MOF pores by the nanoparticles.

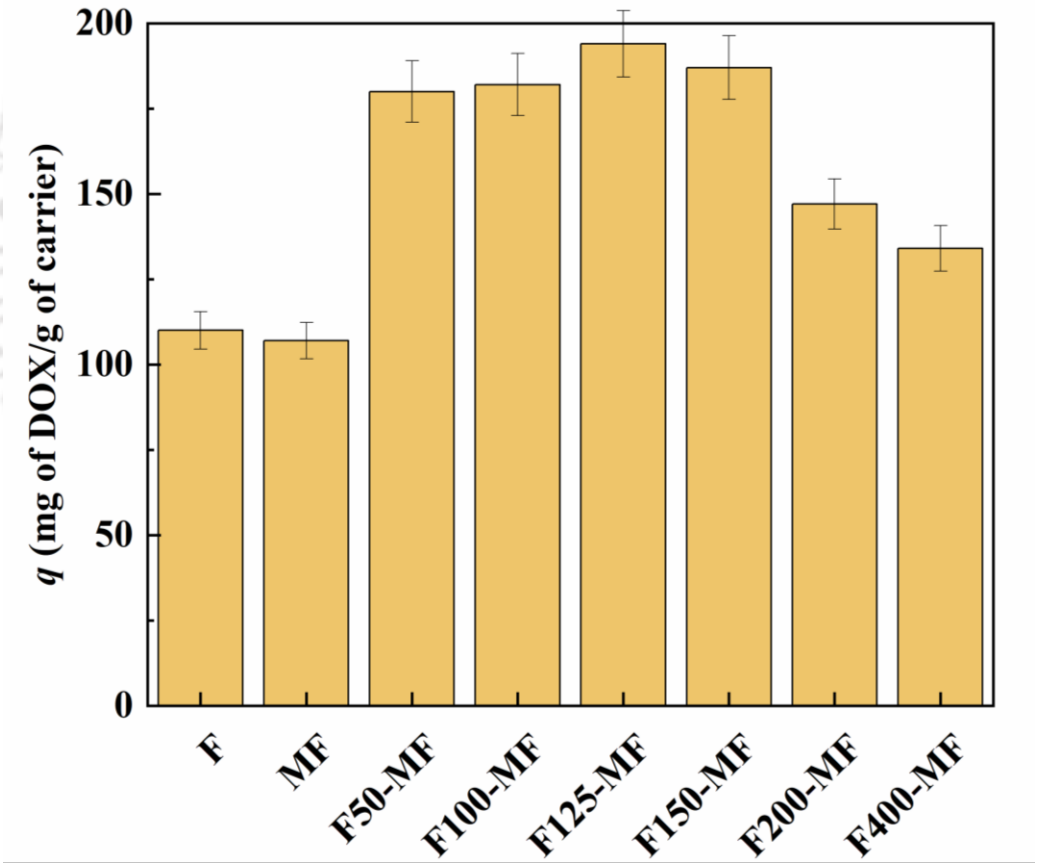

Figure 4.10: DOX loading of F, MF and Fw-MF composites

4.3.8 DOX release study

Specific drug released capacity for pure and all the composites materials are shown in **Figure 4.11**. The specific release capacity of F50-MF is around 41 mg over a span of 10 days; where around 30 mg/g DOX was released from MF in same period. Almost same amount of drug (~ 39 mg/g) was released from pure nanoparticles F with burst effect (in **Figure 4.11a**).

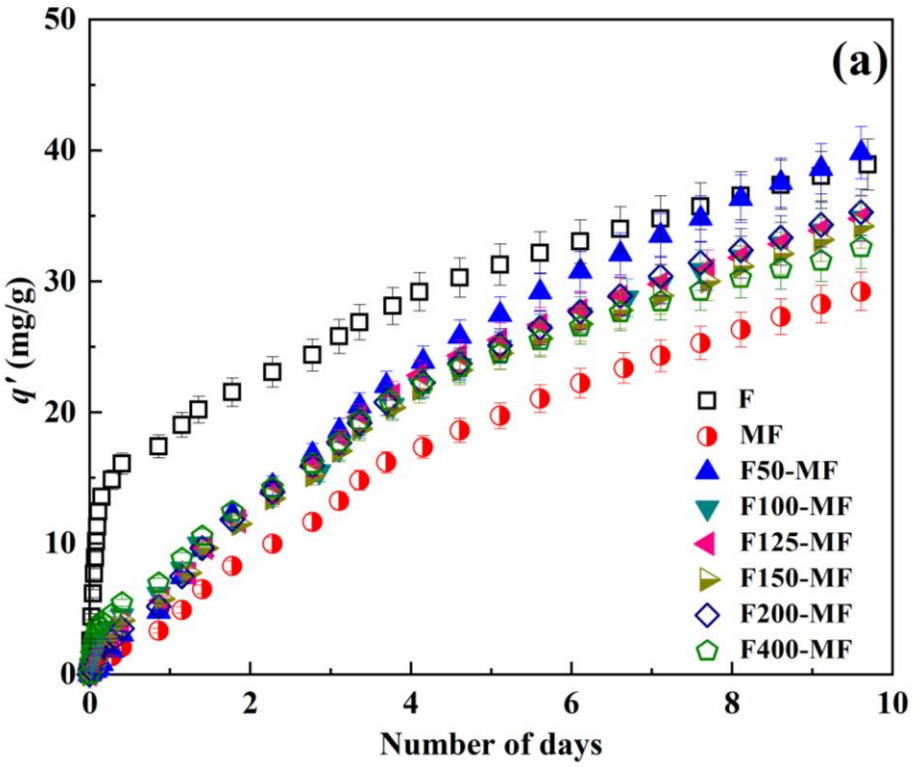

Figure 4.11a: Specific DOX release capacity of Fw-MF composites for first 10 days

The specific DOX release profiles are more controlled for all the Fw-MF composites similar to that of pure MF. The profiles for all the composites follow a sharp release pattern over the first 5 days, then rate of DOX release slow down between 6-15 days; the release kinetics slow down even further after 15 days. F50-MF, F100-MF, F125-MF and F150-MF have provided a specific

release of 53.5, 52.7, 51.4 and 51.1 mg/g of composite over the span of 25 days (in **Figure 4.11b**). These values are significantly higher than DOX released from pure F and MF owing to their higher DOX loading capacities, but retain a controlled release pattern similar to that of pure MF without any burst effect.

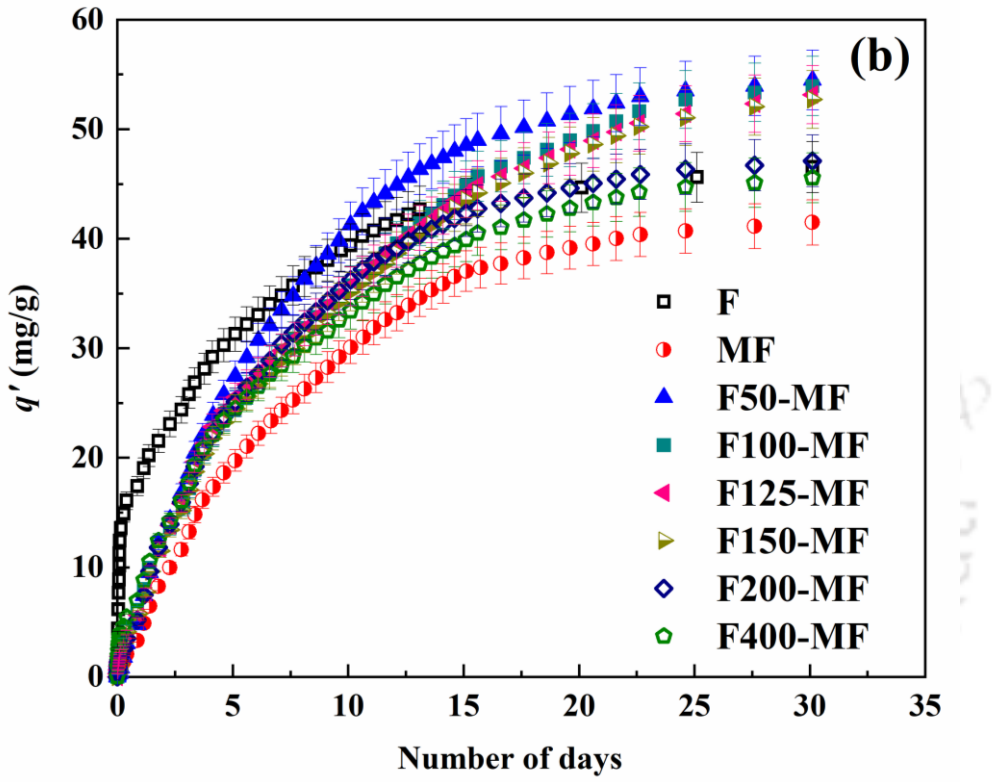

Figure 4.11b: Specific DOX release capacity of Fw-MF composites for 30 days

4.4 Summary

Fe_3O_4 incorporated porous iron carboxylate MIL-100 composites (Fw-MF) were successfully prepared by one pot in situ crystallization technique. The nanoparticle and composites were characterized by various techniques. The presence of nanoparticles was identified by the TEM and SAED analysis. Nanoparticles enhanced the magnetic properties in MIL-100(Fe). The

maximum DOX loading capacity was found for F125-MF (0.16 fraction of NPs) as 194 mg/g. DOX loading capacity in the composites further declined due to pore blockage by the excessive nanoparticles. The released profiles of DOX from the composites were controlled in nature as compare to pure Fe_3O_4.

References

1. M. R. Lohe, K. Gedrich, T. Freudenberg, E. Kockrick, T. Dellmann and S. Kaskel, *ChemComm*, 2011, **47**, 3075–3077.
2. Y-F Huang, Y-Q Wang, Q-S. Zhao, Y. Li and J-M. Zhang, *RSC Adv*., 2014, **4**, 47921–47924.
3. J. Shi, S. Hei, H. Liu, Y. Fu, F. Zhang, Y. Zhong and W. Zhu, J. Chem., 2013, **2013**, article 792827.
4. B. Saha, S. Das, J. Saikia and G. Das, *J. Phys. Chem. C*, 2011, **115**, 8024–8033.
5. M. Shen, W. Jia, C. Lin, G. Fan, Y. Jin, X. Chen and G. Chen, *Nanoscale Res. Lett*., 2014, **9**, 558-565.
6. S. Huang, K-L. Yang, X-F. Liu, H. Pan, H. Zhang and S. Yang, *RSC Adv*., 2017, **7**, 5621-5627.
7. Y-K Seo, J. W. Yoon, J. S. Lee, Y. K. Hwang, C-H. Jun, J-S Chang, S. Wuttke, P. Bazin, A. Vimont, M. Daturi, S. Bourrelly, P. L. Llewellyn, P. Horcajada, C. Serre and G. Férey, *Adv. Mater*., 2012, **24**, 806–810.
8. G. Férey, C. Serre, C. Mellot-Draznieks, F. Millange, S. Surblé, J. Dutour and I. Margiolaki, *Angew. Chem. Int. Ed*., 2004, **43,** 6296–6301.
9. W. Zhou, W. He, S. Zhong, Y. Wang, H. Zhao, Z. Li and S. Yan, *J. Magn. Magn. Mater*., 2009, **321**,1025-1028.
10. S. Ghosh, A.Z.M. Badruddoza, M.S. Uddin and K. Hidajat, *J. Colloid Interface Sci*., 2011, **354**, 483–492.
11. N. A. Spaldin, *Magnetic Materials Fundamentals and Appli*cations, 2011, Second edition, Cambridge University Press, UK.

Chapter 5

Loading and release of doxorubicin hydrochloride from iron(III) trimesate MOF and zinc oxide nanoparticle composites

Chapter 5

Loading and release of doxorubicin hydrochloride from iron(III) trimesate MOF and zinc oxide nanoparticle composites

In this chapter, Iron(III) trimesate metal organic framework i.e. MIL-100(Fe) and its composites with ZnO nanoparticles i.e. ZnO@MIL-100(Fe) were investigated as delivery agents for anticancer drug doxorubicin hydrochloride (DOX). The synthesis of the composites was done in two routes viz. a conventional HF route (in the presence of HF as crystallizing agent) and another in the absence of HF. The resultant MOF and its composites significantly differ in DOX loading capacity and release rates. The results obtained in this work indicate that DOX loading capacity increases upon addition of nanoparticles when the original MOF has lower mesopore volume (as in the sample obtained via HF route). Details of synthesis procedures and results are discussed in this chapter.

5.1 Synthesis of pure MIL-100(Fe) and ZnO

Synthesis procedures of MIL-100 (Fe) through HF route (referred as MF) and HF free route (referred as MNF1) were described in the preceding section 2.2.1. The synthesis description of ZnO nanoparticles (henceforth referred as Z) synthesis was given in the section 2.2.3 (chapter 2)

5.2 Synthesis of ZnO@MIL-100(Fe) composites by HF route

The synthesis procedure for ZnO@ MIL-100(Fe) (henceforth referred as Zw-MF) composites was similar to that of Fe_3O_4@ MIL-100(Fe); instead Fe_3O_4 nanoparticles, w (g) of ZnO particles were introduced in the raw precursors. Several composites with w = 100, 200 and 300 were synthesized following the procedure similar to described in section 4.2 (chapter 4).

5.3 Synthesis of ZnO@MIL-100(Fe) and Fe_3O_4@MIL-100(Fe) composites by HF free route

In case of HF free route, w g of ZnO or Fe_3O_4 particles were added to the MOF precursors i.e. 8.08 g of $Fe(NO_3)_3.9H_2O$, 2.7 g BTC and 20 ml of water. Several composites with varying the 'w' amount of nanoparticles were synthesized. The remaining steps for synthesis and purification procedure were similar to that of MNF1 synthesis in the preceding section 2.2.1 (chapter 2). the composites are referred as Zw-MNF1 for ZnO@MIL-100 or Fw-MNF1 for Fe_3O_4@MIL-100 in this chapter.

5.4 Results and discussion

5.4.1 FESEM analysis

The FESEM images of pure MOF and its nanocomposites are shown in **Figure 5.1**. In the case of pure MIL-100(Fe) synthesized by HF route (MF), a well facetted octahedral morphology with different particle sizes [1] was observed (**Figure 5.1a**). However, the particles of MNF1 lack the sharp edges as in case of MF and seem to be aggregated (**Figure 5.1b**). The morphology of

ZnO nanoparticles (**Figure 5.1c**) indicates the particles are spherical in the size range of 20-50 nm. Similar size distribution was previously reported in literature. [2]

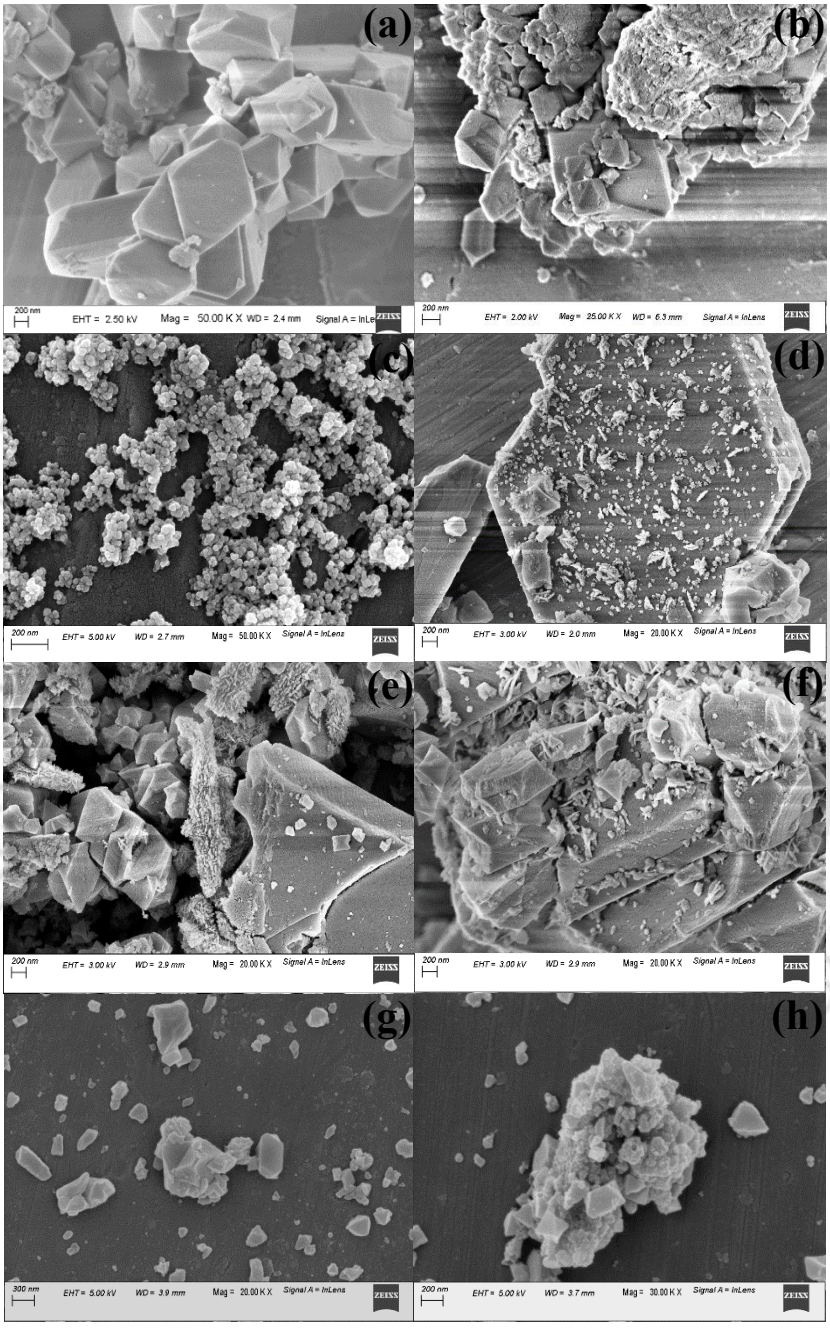

Figure 5.1: FESEM micrographs of (a) MF, (b) MNF1, (c) Z, (d) Z100-MF (e) Z200-MF (f) Z300-MF (g) Z100-MNF1 (h) Z400-MNF1

The FESEM images of Zw-MF composites shown in **Figure 5.1d-5.1f** indicate the presence of additional smaller particles on the well facetted MF structures. This morphology of the composite was similar to that observed by in case of ZnO-PLA composites.[3] However, as MNF1 is not well facetted, smaller ZnO nanoparticles could not clearly distinguished in case of Zw-MNF1 composites (in **Figure 5.1g- 5.1h**).

5.4.2 EDX mapping analysis

The elemental mapping patterns for the composites are shown in **Figure 5.2**. The EDX analysis was performed on pellets made by compacting of the powdered sample. The FESEM images of those pellets are shown along with the mapping patterns. Carbon (C), oxygen (O) and iron (Fe) are well distributed in all the materials. Zn is also uniformly distributed throughout the observed area and as expected, the intensity of element Zn increased with the amount of ZnO present in the composites.

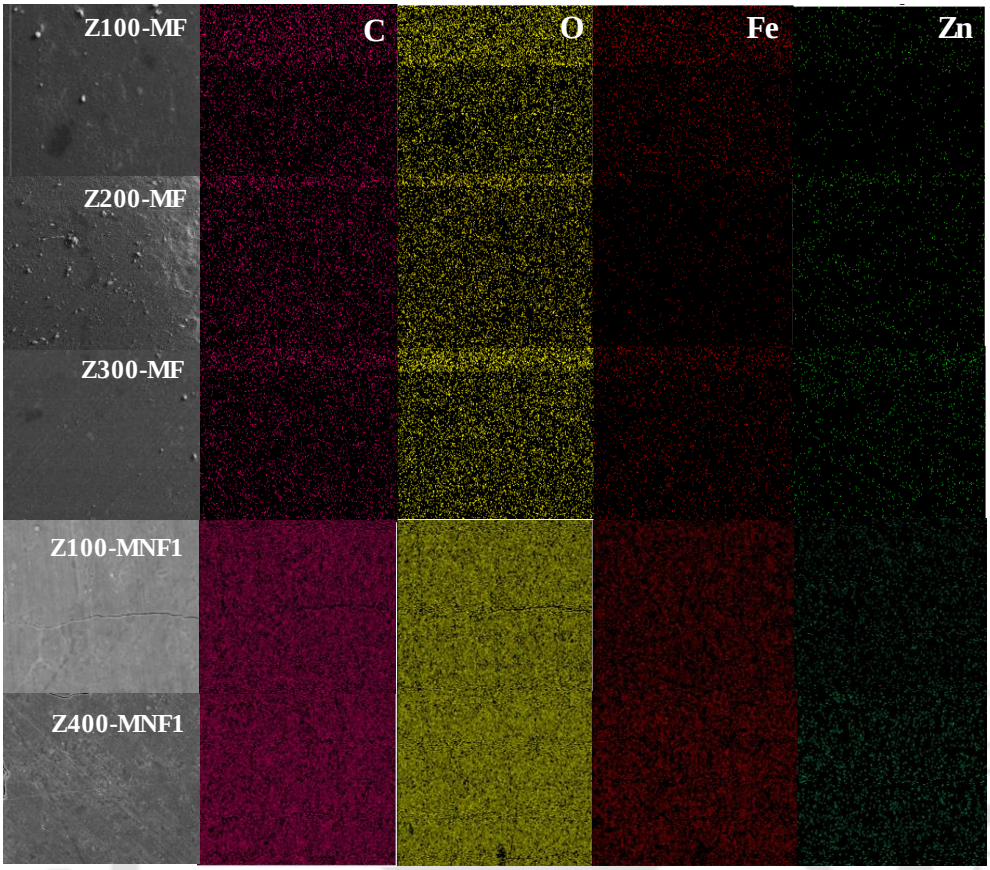

Figure 5.2: EDX mapping images of Zw-MF and Zw-MNF1 composites

5.4.3 TEM analysis

The FETEM image in **Figure 5.3a** indicates that the ZnO particles have a size range in between 15 and 30 nm. The SAED patterns (**Figure 5.3b**) of synthesized ZnO are similar to that of wurtzite with Miller indices along (1 0 0), (0 0 2), (1 0 1), (1 0 2), (1 1 0), (1 0 3), and (1 1 2) planes [4, 5] and in accordance with the XRD results (discussed later). **Figure 5.3c-5.3e** describe the morphology of Zw-MF composites. In these figures, darker areas of higher electron density correspond to ZnO particles, whereas brighter areas correspond to MF. In case of Z100-MF and

Z200-MF composites, nanoparticles are well distributed in MOF matrix, but with higher ZnO content, particles tend to agglomerate as in case of Z300-MF.

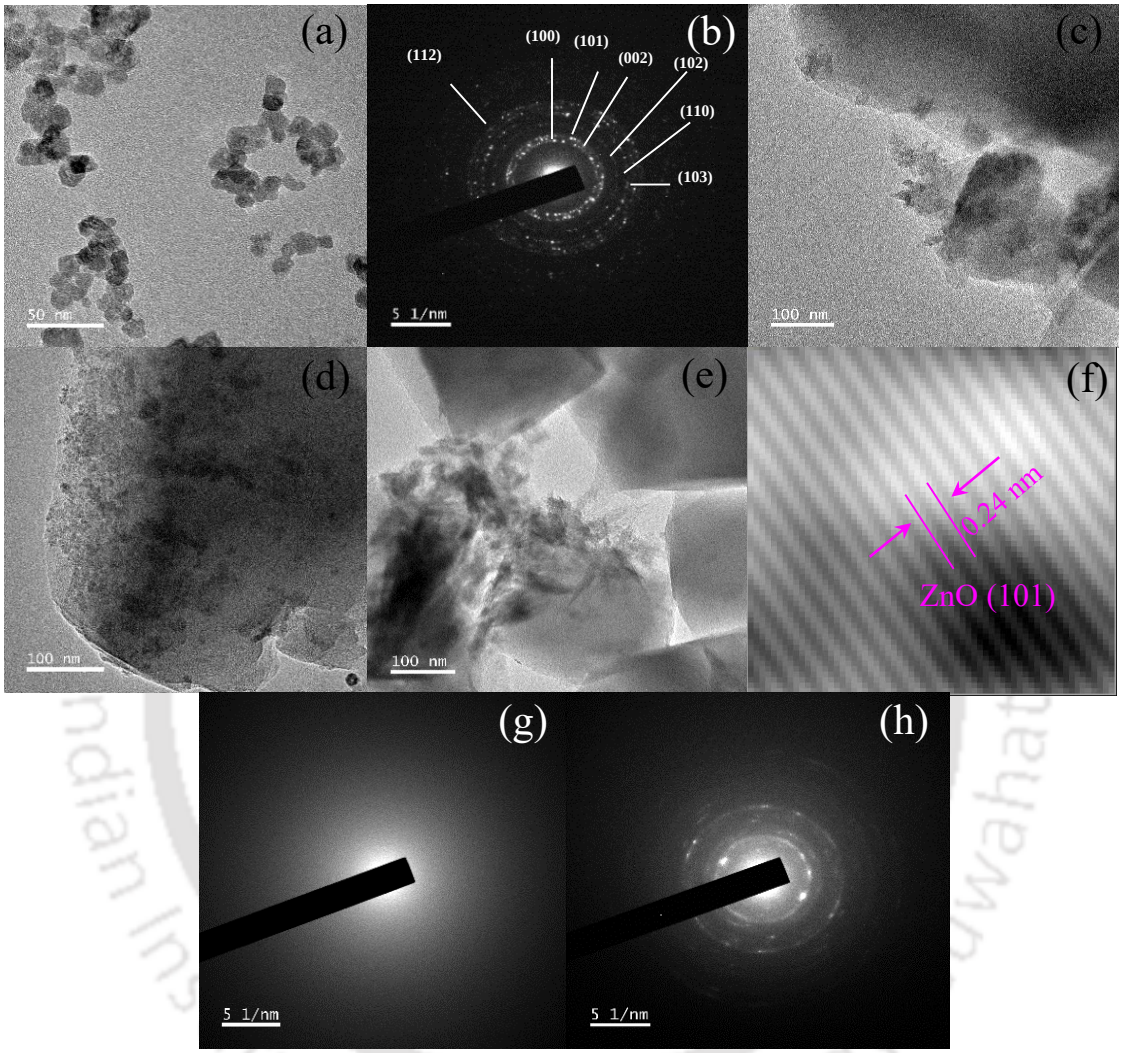

Figure 5.3: FETEM micrograph of (a) Z, (b) SAED pattern of Z, FETEM micrographs of (c) Z100-MF, (d) Z200-MF, (e) Z300-MF, (f) HRTEM of Z200-MF (darker areas) (g) SAED of Z300-MF (brighter area), (h) SAED pattern of Z300-MF (darker area)

Figure 5.3f represents the HRTEM image of Z200-MF composite (darker side corresponding to ZnO). The HRTEM image shows a parallel lattice fringes with lattice spacing of 0.24 nm, which can be ascribed to (101) planes of ZnO. [6, 7] **Figure 5.3g** shows the SAED pattern of low electron density zone of Z300-MF composite (lighter region); since this region corresponds to MF, no diffraction patterns were visible (similar to that of pure MF in **Figure 4.3b**, in the preceding section 4.3.2.). On the other hand, diffraction is distinctly visible in the SAED pattern (**Figure 5.3h**) of the high-electron density zone (darker area) of Z300-MF corresponds to ZnO.

5.4.4 XRD analysis

The powder X-ray diffraction (PXRD) patterns of pure Z, MF and Zw-MF composites are shown in **Figure 5.4a**. The PXRD for pure ZnO depicts eight characteristic peaks at 2θ of 31.7, 34.4, 36.3, 47.6, 56.7, 62.9, 67.9 and 69.2° corresponds to the crystalline planes of (1 0 0), (0 0 2), (1 0 1), (1 0 2), (1 1 0), (1 0 3), (1 1 2) and (2 0 1), respectively. Similar type of crystalline planes for ZnO was reported in literature. [8, 9] In XRD pattern of composites, no significant peaks corresponding to ZnO were observed, as its content is relatively small compared to MF. Similar results were observed for Zw-MNF1 composites (in **Figure 5.4b**). In addition, it is worth noting that the composites also exhibit good crystallinity similar to that of MF and MNF1.

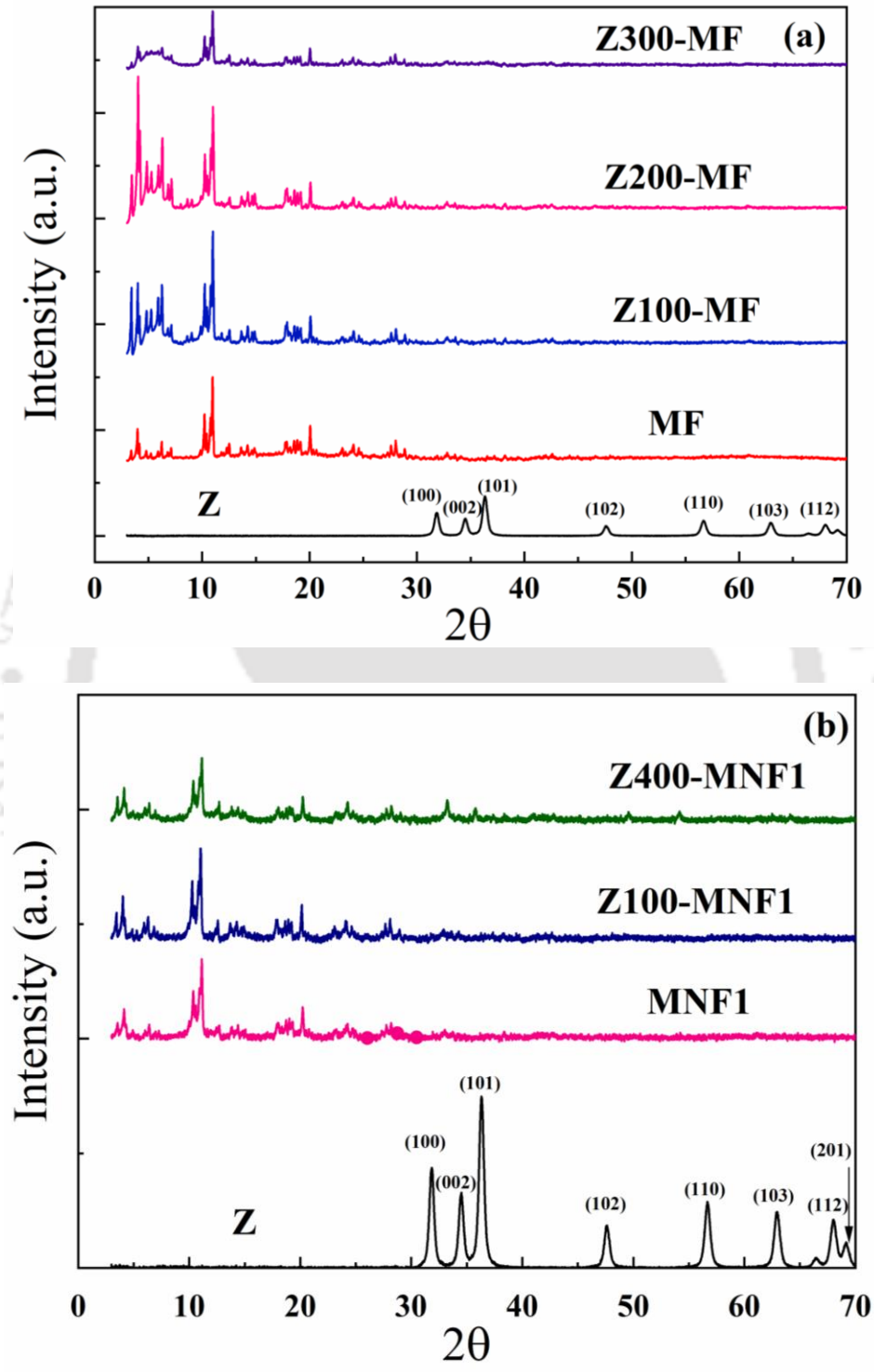

Figure 5.4: X-ray diffraction patterns of (a) Z, MF and Zw-MF composites and (b) Z, MNF1 and Zw-MNF1 composites

5.4.5 N_2 adsorption-desorption isotherms analysis

A type IV isotherm with a hysteresis loop was observed for ZnO nanoparticles (**Figure 5.5a**, inset), indicating the presence of mesopores. [10,11] MF exhibits a type I N_2 adsorption-desorption isotherm, indicative of its microporous nature with small external surface area. [12, 13] Zw-MF composites also exhibit similar isotherm type (**Figure 5.5a**). Similar observations were reported for Fe_3O_4@MIL-100(Fe) composites in the previous chapter.

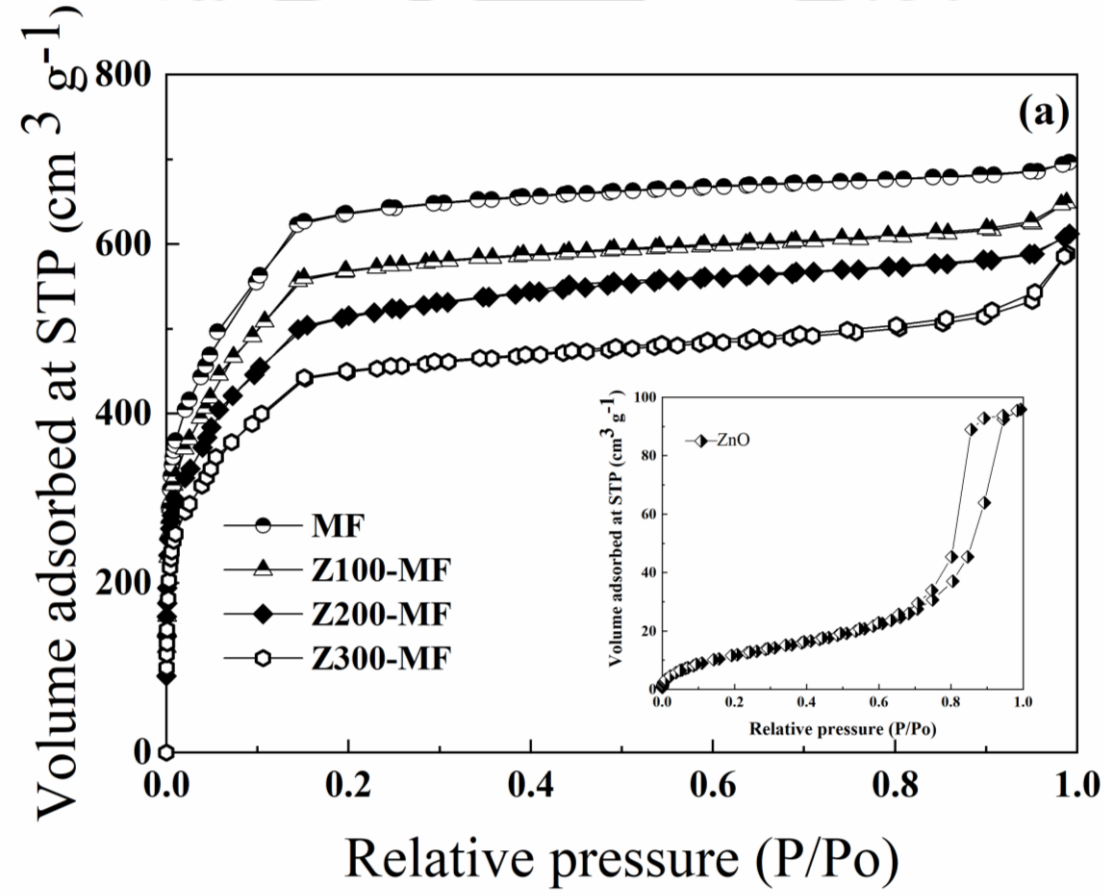

Figure 5.5a: N_2 adsorption-desorption isotherms of ZnO (inset), MF and Zw-MF composites

On the other hand, isotherms of MNF1 and its composites (**Figure 5.5b**) are of type IV with a hysteresis loop. [14] The surface area and the total pore volume are given in **Table 5.2**. The variation in surface area and pore volume with the addition of ZnO nanoparticles are shown in **Figure 5.6**.

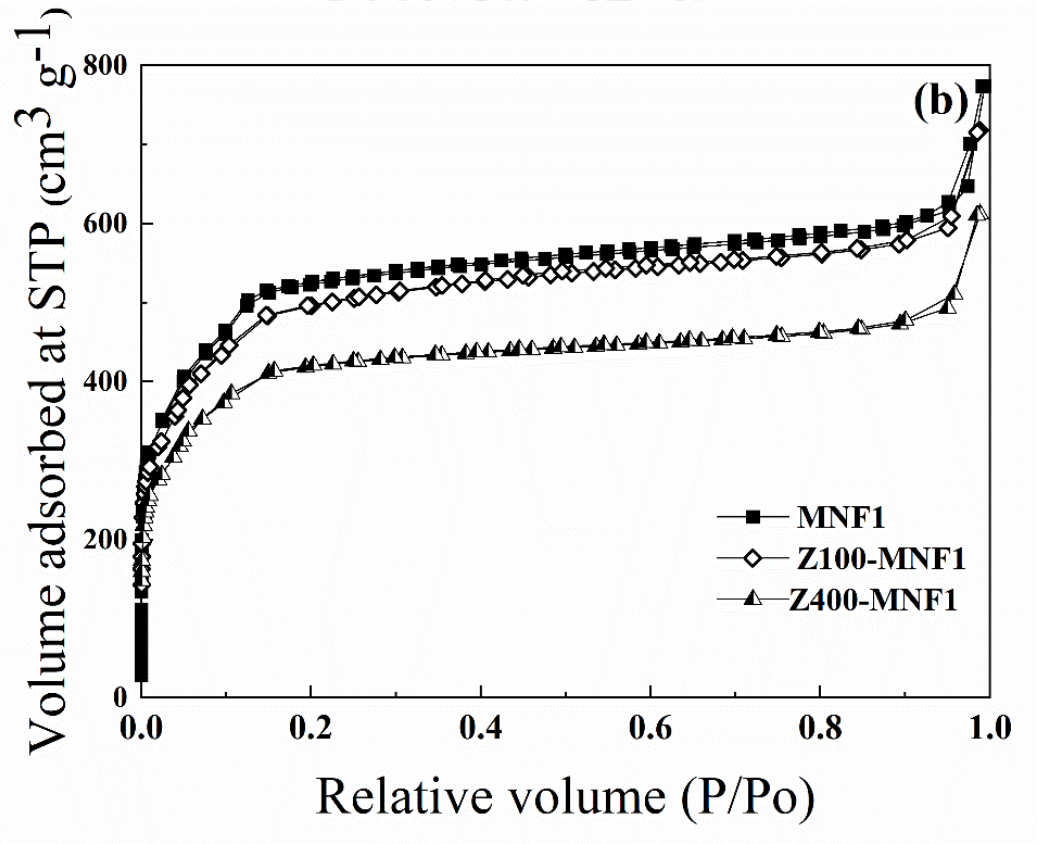

Figure 5.5b: N_2 adsorption-desorption isotherms of MNF1 and Zw-MNF1 composites

Pure ZnO has a surface area of 46 m^2 g^{-1} and pore volume of 0.15 cm^3 g^{-1} and comparable to previously reported literature. [15] In case of the composites, the BET surface area and pore volume decrease due to presence of (relatively nonporous) ZnO nanoparticles. The surface area

and pore volume of all the composites vary almost linearly with the mass fraction of the nanoparticles present in the composites (**Figure 5.6**). Similar kind of trend was seen for Fw-MF composites in chapter 4.

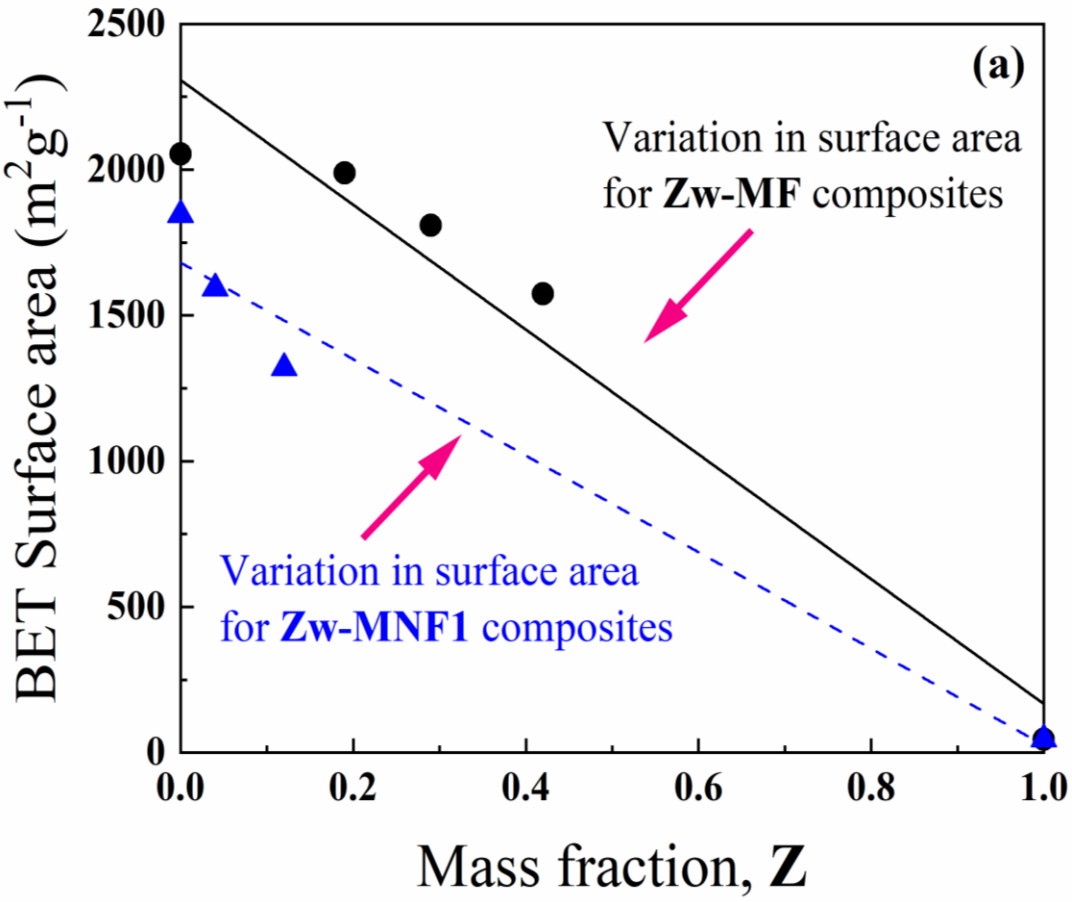

Figure 5.6a: Variation in surface area for Zw-MF and Zw-MNF1 composites with the mass fraction of ZnO

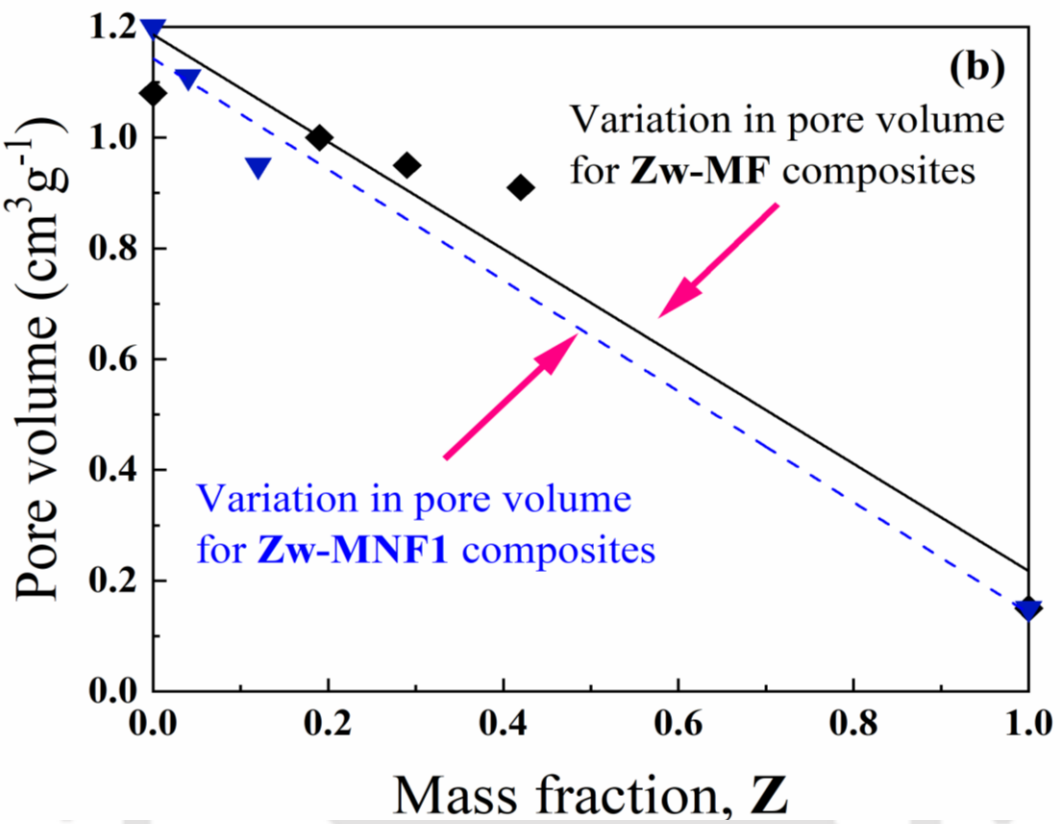

Figure 5.6b: Variation in pore volume for Zw-MF and Zw-MNF1 composites with the mass fraction of ZnO

5.4.6 TGA analysis

The thermal stability of Zw-MF and Zw-MNF1 composites were studied over the temperature range of 30-800 °C and is shown in **Figure 5.7**. ZnO nanoparticles are stable up to temperature of 800 °C. The total loss about 9 wt% due to loss of bound water and impurities like acetate groups (in the temperature range of 200-400 °C) present in the nanoparticles.[16] However, weight loss for Zw-MF and Zw-MNF1 composites are quite high. The TG trend for all the Zw-MF composites are similar to pure MF. The first loss in between 80-150 °C is due to removal of moisture from the frameworks. The second gradual loss (150- 350 °C) is due to release of

interrelated water associated with the metal trimers. The third major loss is owing to complete decay of organic linker BTC at the temperature range of 350-700 °C .[17] Similar kind of trend is observed for Z400-MNF1; although the weight loss in between 80-150 °C is slightly less as compare to pure **MNF1**. Similar kind of trend in the said temperature is observed for Fw-MF composites with increase in nanoparticle loading in the preceding section 4.3.4.

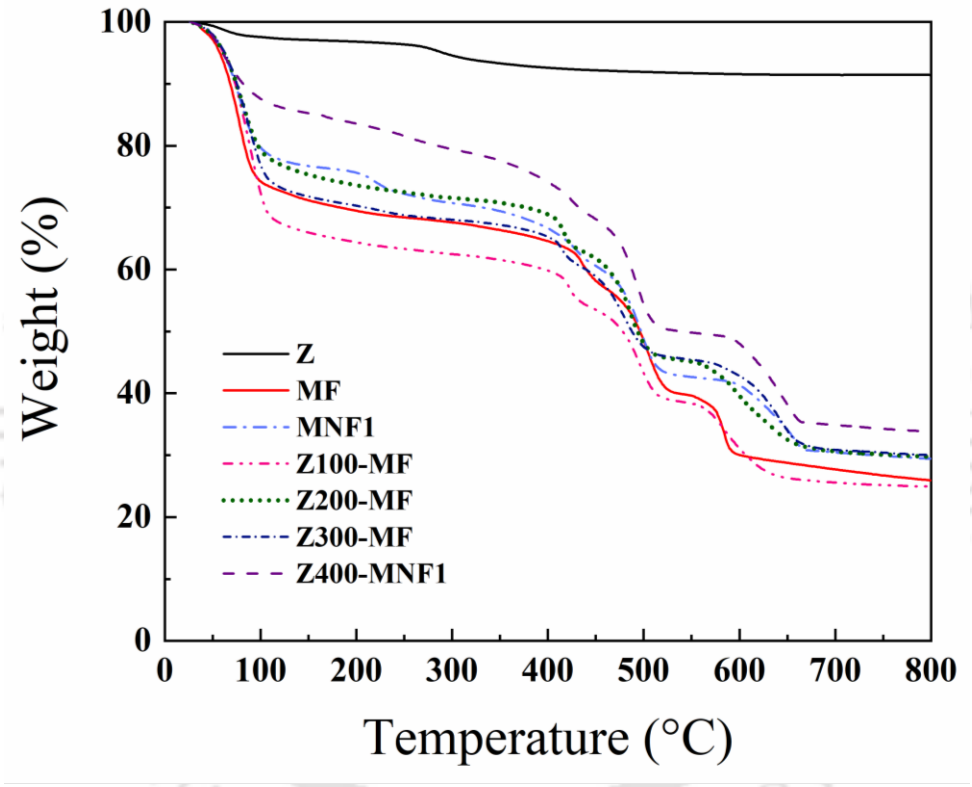

Figure 5.7: TGA curves of Zw-MF and Zw-MNF1 composites

5.4.7 DOX loading

The DOX loading capacities of pure Z, MF and MNF1 and its composites are shown in **Figure 5.8**. Pure MF has a DOX loading capacity of 107 mg/g, while loading capacity of Z is much

higher at 253 mg/g. It is interesting to note that the loading capacity of ZnO nanoparticles obtained in this work is significantly higher than that of pure Fe_3O_4 nanoparticles (110 mg/g).

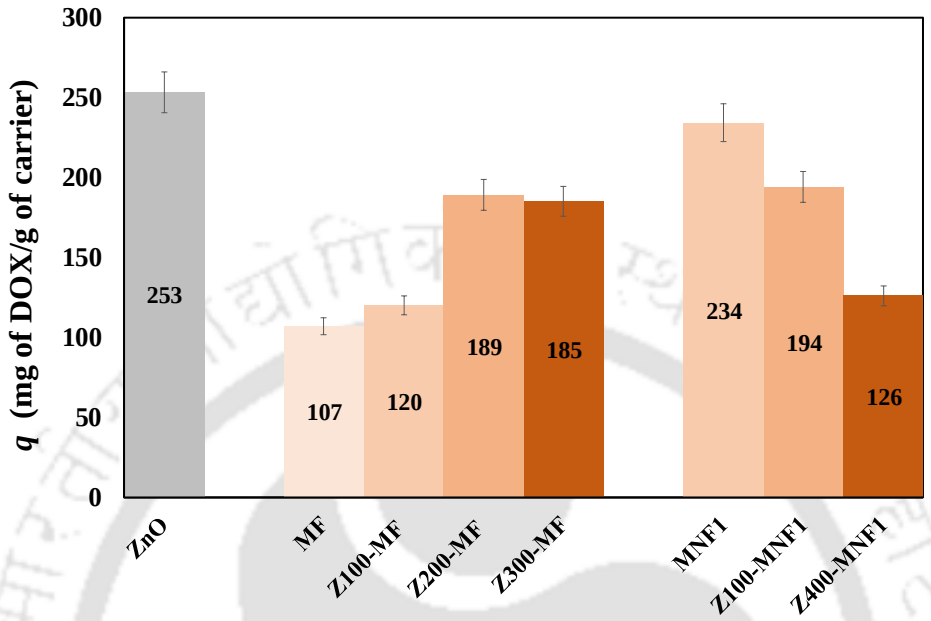

Figure: 5.8: DOX loading of Z, MF, MNF1, Zw-MF and Zw-MNF1 composites

The possible reason for such DOX loading difference lies in structural features of nanoparticles and the drug. It is well established that there are three potential metal binding sites available in DOX structure. One is the nitrogen atom in the sugar moiety and other two are the chelating sites of the quinone and the phenolic oxygens on the both sides of the anthracycline aromatic moiety [18,19] showed in **Figure 5.9**. In addition, due to low affinity of metal ions for nitrogen atom donor, two possible sites for binding in DOX structure are the two keto-phenolate functions.[18] Further, it is also well known fact that metal with divalent ions (M^{2+}; M refers to Zn, Fe, etc.) are more likely to conjugate with those keto-phenolate functions.[19] So, in case of ZnO nanoparticles Zn^{2+} ions are more likely to bind with keto-phenolate functions of DOX.[18] On other hand, Fe_3O_4 has both the Fe^{3+} and Fe^{2+} ions in the structure. Fe_3O_4 has the inverse

spinel structure Fe^{3+} [Fe^{3+} Fe^{2+}] O_4, with one Fe^{3+} per formula unit on tetrahedral sites and the remaining Fe^{3+} and Fe^{2+} randomly distributed on octahedral sites.[20, 21] Previous research in the literature indicated the formation of Fe^{2+} -DOX conjugate in case of iron oxide nanoparticles.[22] So, in case of Fe_3O_4 nanoparticles the less number of ions (only Fe^{2+}) per unit cell are conjugating with DOX; however, more Zn^{2+} ions are combined with DOX may be the reason for such difference in drug loading. Similar kind of DOX loading percentage was observed in previous literatures in case of Fe_3O_4[22, 23] and ZnO nanoparticles.[24]

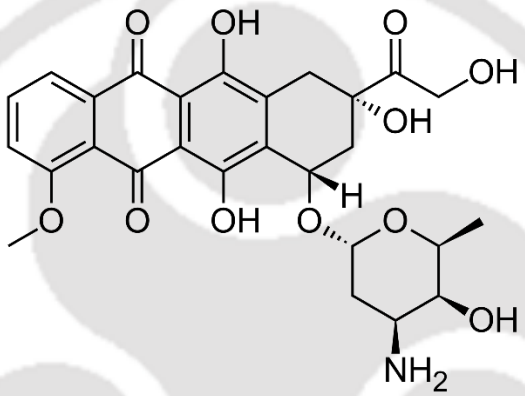

Figure 5.9: Structure of DOX

In case of composites, loading capacity increases with the amount of ZnO in the composite up to Z200-MF and decreases thereafter. The maximum loading capacity is 189 mg/g for Z200-MF. This increase is similar to that observed due to presence of Fe_3O_4 nanoparticles. It is worth noting that even in case of Fe_3O_4 composites a loading capacity of about 194 mg/g was obtained (with Fe_3O_4 fraction of x = 0.16), although the loading capacity of pure Fe_3O_4 nanoparticles was much lower than that on ZnO nanoparticles. Thus, it seems that the content of nanoparticles in the MIL-100(Fe) composites is more important than the chemical nature of the nanoparticles themselves. Presence of nanoparticles changes the particle morphology thereby significantly affecting the DOX adsorption characteristics.

Pure MNF1 shows a DOX loading capacity of 234 mg/g, slightly lower than the loading capacity of pure ZnO nanoparticles, but significantly higher than MF and all its composites (**Figure 5.8**). This behaviour is attributed to the presence of significantly higher mesopore volume in MNF1. It was previously demonstrated that DOX binding on to the MOF occurs due to the formation of coordination bonds between one or both deprotonated hydroxyl groups on the aglycone moiety of DOX (**Figure 5.9**) and the unsaturated Fe(III) metal centres.[25]

However, surprisingly in the case of MNF1 composites, the DOX loading capacity does not improve with the addition of ZnO nanoparticles, as expected. For example, even after addition of a small amount (4 wt %) of ZnO nanoparticles, the loading decreases to 194 mg/g. With increase in the ZnO content in the composite (12 wt %), the loading decreased even further to 126 mg/g for Z400-MNF1. Thus, it seems that if the pure MOF initially has high mesopore volume, addition of metal oxide nanoparticles does not enhance the DOX loading capacity. The ZnO nanoparticles block the adsorption sites within the mesopores of MNF1 resulting in this behavior. Similar results are observed for Fw-MNF1 composites (**Table 5.1**); with addition of Fe_3O_4 particles to MNF1, the DOX loading capacity decreased significantly.

Table 5.1: DOX loading capacity of Fw-MNF1 composites

Sr. No.	**Composites**	**Mass fraction of Fe_3O_4 (x)**	**q (mg g^{-1})**
1	MNF1	-------	234
2	F027-MNF1	0.01	267
3	F200-MNF1	0.06	150
4	F1000-MNF1	0.32	84

An interesting insight can also be obtained by comparing the loading on the composites against the loading on a simple physical mixture (q_{mix}) of the nanoparticles and MIL-100(Fe). It is calculated using

$$q_{mix} = x\, q_{ZnO} + \quad (1 - x)\, q_{MOF} \quad ---------- 5.1$$

where *x* is the mass fraction of ZnO in the composite, q_{ZnO} is the DOX loading on pure ZnO nanoparticles and q_{MOF} is the DOX loading on pure MIL-100(Fe) (i.e. either MF or MNF1). The values of q_{mix} calculated using Eq. (5.1) are given in Table 5.2.

Table 5.2: Surface area, pore volume and DOX loading capacities of various samples

Sample	**mass fraction of ZnO , *x***	**BET Surface area ($m^2\ g^{-1}$)**	**Total pore volume ($cm^3\ g^{-1}$)**	***q*** **(mg g^{-1})**	q_{mix} **(mg g^{-1})**
MF	0.0	2054	1.08	107	-
MNF1	0.0	1845	1.20	234	-
ZnO	1.0	46	0.15	253	-
Z100-MF	0.19	1989	1.00	120	135
Z200-MF	0.29	1809	0.95	189	149
Z300-MF	0.42	1574	0.91	185	168
Z100-MNF1	0.04	1593	1.11	194	235
Z400-MNF1	0.12	1320	0.95	126	236

In the case of MF composites, at low concentration of ZnO as in Z100-MF, the values of *q* and q_{mix} are close to one another. As *x* is increased, in case of Z200-MF, the value of *q* is higher than that of q_{mix}, i.e. the incorporation of ZnO results in significantly higher drug adsorption compared to simple physical mixing. The nanoparticles form an intricate part of the final structure of the composites manifesting in this behaviour. This difference starts to diminish as *x* is increased further, indicating the advantage of having nanoparticles in the structure starts to

decrease. As opposed to this behaviour, in case of Zw-MNF1 composites, q_{mix} was always higher than q indicating that incorporation of nanoparticles into the structure does not show any synergistic effect for loading of DOX on MNF1, on the other hand it is detrimental.

5.4.8 DOX release study

The specific DOX release capacity of various carriers are given in **Figure 5.10**. Initially, the release from ZnO nanoparticles is significantly faster (so-called burst-effect); almost 50 mg/g of DOX was released in first day and about 100 mg/g was released within 5 days. DOX release from MF, MNF1 and other composites do not exhibit the burst-effect, indicating stronger interaction of the drug with these carriers.

The composite Z100-MF, has a higher DOX loading capacity compared to that on **MF**; this results in higher amount of drug release (**Figure 5.10a**). In fact, the trend closely follows that on MNF1 (**Figure 5.10b**) which has significantly higher mesopore volume. The specific drug release capacities (q') of Z200-MF and Z300-MF were lower than Z100-MF, although they have higher DOX loading capacity; this indicates a synergistic effect of the incorporation of ZnO into MIL-100(Fe) resulting in strong interaction of DOX with the framework, and hence the slow release. On the other hand, the composite Z400-MNF1 has lower q' compared to MNF1, due to its lower drug loading capacity (**Figure 5.10b**).

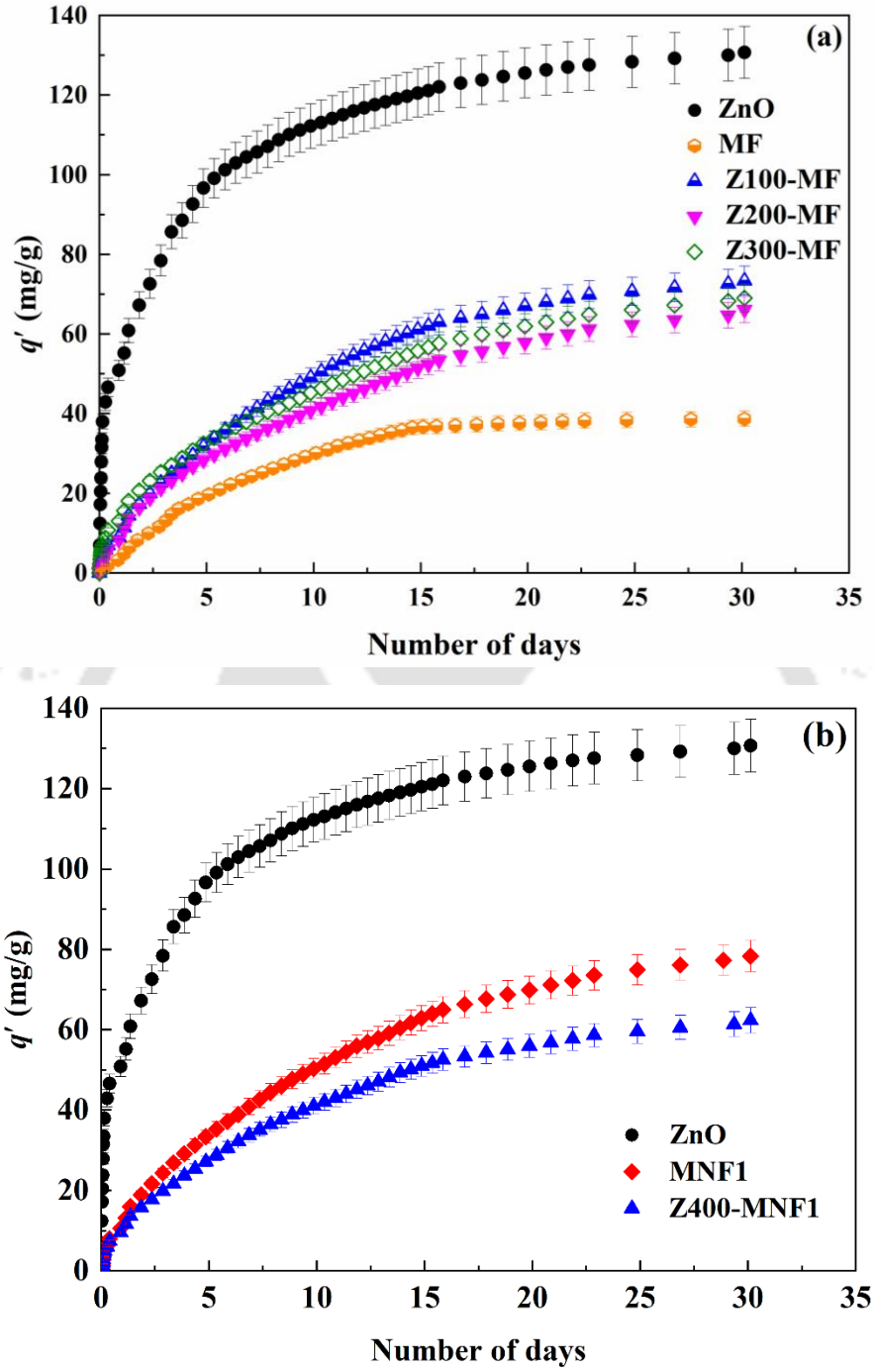

Figure 5.10: Specific drug released from (a) Z, MF and Zw-MF composites and (b) Z, MNF1 and Zw-MNF1 composites

5.5 Summary

In this chapter, ZnO incorporated MIL-100(Fe) composites (prepared by both HF and without HF route) were investigated as DOX carrier. All the composites were thoroughly characterized by different characterization techniques. The presence of ZnO in MOF structure were estimated by HRTEM and SAED analysis. It was observed from the literatures, that divalent metal ions like Zn^{2+}, Fe^{2+} might conjugate with keto-phenolate functional groups of DOX. Fe_3O_4 contained both Fe^{3+} and Fe^{2+} and only those Fe^{2+} ions only might conjugate with DOX. Thus, DOX loading capacity was higher for ZnO as compare to Fe_3O_4. The maximum loading capacity for composites was found for 189 mg/g for Z200-MF (with 0.29 fraction of NPs). In addition, the loading was not enhanced as compare to pure MNF1; as the MNF1 was initially mesoporous and addition of NPs blocked the active sites for adsorption. The DOX released profiles from the composites were well controlled over 25 days.

References

1. J.Shi, S. Hei, H. Liu, Y. Fu, F. Zhang, Y. Zhong and W. Zhu, *J. Chem*., 2013, **2013**, article 792827.
2. M. Pudukudy and Z. Yaakob, *J. Clust. Sci*., 2015, **26**, 1187–1201.
3. H. Rodríguez-Tobías, G. Morales, A. Olivas and D. Grande, *Macromol. Chem. Phys*., 2015, **216**, 1629-1637.
4. S. Gao, W.Yang, J. Xiao, B. Li and Q. Li, J. Mater. Sci. Technol., 2019, **35**, 610-614.
5. A. Quintana, A. Altube, E. García-Lecina, S. Suriñach, M. D. Baró, J. Sort, E. Pellicer and M. Guerrero, *J. Mater. Sci*., 2017, **52**, 13779-13789.
6. H. Yang, S-Q Ni, X. Jiang, W. Jiang and J. Zhan, *CrystEngComm*, 2012, **14**, 6023-6028.
7. Y. Chen, H. Ding and S. Sun, *Nanomaterials*, 2017, **7**, article 217.
8. S. Harish, M. Navaneethan, J. Archana, A. Silambarasan, S. Ponnusamy, C. Muthamizhchelvan and Y. Hayakawa, *Dalton Trans*., 2015, **44**, 10490-40498.
9. S. Bhatia, and N. Verma, *Mater. Res. Bull*., 2017, **95**, 468-476.
10. J-Y. Dong, W-H. Lin, Y-J. Hsu, D. S-H. Wong and S-Y. Lu, *CrystEngComm*, 2011, **13**, 6218-6222.
11. A. N. Kadam, D. P. Bhopate, V. V. Kondalkar, S. M. Majhi, C.D. Bathula, A-V Tran and S-W Lee, *J. Ind. Eng. Chem*., 2018, **61**, 78-86.
12. Y-K Seo, J. W. Yoon, J. S. Lee, Y. K. Hwang, C-H. Jun, J-S Chang, S. Wuttke, P. Bazin, A. Vimont, M. Daturi, S. Bourrelly, P. L. Llewellyn, P. Horcajada, C. Serre and G. Férey, *Adv. Mater*., 2012, **24**, 806–810.
13. G. Férey, C. Serre, C. Mellot-Draznieks, F. Millange, S. Surblé, J. Dutour and I. Margiolaki, *Angew. Chem. Int. Ed*., 2004, **43**, 6296–6301.

14. Y. Fang, J. Wen, G. Zeng, F. Jia, S. Zhang, Z. Peng and H. Zhang, *Chem. Eng. J*., 2018, **337**, 532-540.

15. J-Y. Dong, W-H. Lin, Y-J. Hsu, D. S-H. Wong and S-Y. Lu, *CrystEngComm*, 2011, **13**, 6218-6222.

16. M. F. Khan, A. H. Ansari, M. Hameedullah, E. Ahmad, F. M. Husain, Q. Zia, U. Baig, M. R. Zaheer,M. M. Alam, A. M. Khan, Z. A. AlOthman, I. Ahmad, G. M. Ashraf, and G. Aliev, *Sci. Rep*., 2016, **6**, 27689.

17. S. Huang, K-L. Yang, X-F. Liu, H. Pan, H. Zhang and S. Yang, *RSC Adv*., 2017, **7**, 5621-5627.

18. K. C. Barick, S. Nigam and D. Bahadur, *J. Mater. Chem*., 2010, **20**, 6446-6452.

19. S. A. Abraham, K. Edwards, G. Carlson, S. MacIntosh, L. D. Mayer, C. McKenzie, M. B. Bally, *Biochim. Biophys. Acta, Biomembr*., 2002, **1565**, 41-54.

20. S. K. Sahu, B. Huang, K. Lilova, B. F. Woodfield and A. Navrotsky, *Phys. Chem. Phys. Chem*., 2015, **17**, 22286-22295.

21. S. C. Abrahams and B. A. Calhoun, *Acta Cryst*., 1953, **6**, 105–106.

22. E. Munnier, S. Cohen-Jonathan, C. Linassier, L. Douziech-Eyrolles, H. Marchais, M. Soucé, K. Hervé, P. Dubois and I. Chourpa, *Int. J. Pharm*., 2008, **363**, 170-176.

23. S. Nigam, K.C. Barick and D. Bahadur, *J. Magn. Magn. Mater*., 2011, **323**, 237-243.

24. Y. Deng and H. Zhang, *Int. J Nanomed*., 2013, **8**,1835-1841.

25. R. Anand, F. Borghi, F. Manoli, I. Manet, V. Agostoni, P. Reschiglian, R. Gref, and S. Monti, J. *Phys. Chem. B*, 2014, **118**, 8532−8539.

Chapter 6

CeO_2 promoted MIL-100(Fe) for the controlled release of doxorubicin hydrochloride

CeO_2 promoted MIL-100(Fe) for the controlled release of doxorubicin hydrochloride

In this chapter, MIL-100(Fe) and its composites with CeO_2 nanoparticles i.e. CeO_2@MIL-100(Fe) are investigated as carriers for anticancer drug doxorubicin hydrochloride (DOX). As per the literature, the bare CeO_2 have much higher DOX loading as compare to pure Fe_3O_4. Therefore, CeO_2@MIL-100(Fe) is likely to have a higher DOX loading capacity compared to other MIL-100(Fe) composites. The synthesis of the composites was done in two routes viz. a conventional HF route (in the presence of HF as crystallizing agent) and another in the absence of HF. Details of synthesis procedures and results are discussed in this chapter.

6.1 Synthesis of pure MIL-100(Fe) and CeO_2

Synthesis procedures of MIL-100 (Fe) through HF route (referred as MF) and HF free route (referred as MNF1) were described in section 2.2.1. CeO_2 was prepared by precipitation of aqueous solution of cerium nitrate with dextran as a stabilizer [1, 2]. The detail description of CeO_2 nanoparticles synthesis is given in the preceding section 2.2.4 (chapter 2).

6.2 Synthesis of CeO_2@MIL-100(Fe) composites

The synthesis procedure for CeO_2@ MIL-100(Fe) (henceforth referred as Cw-MF or Cw-MNF1) composites was similar to that of ZnO@ MIL-100(Fe) (section 5.2 and section 5.3);

instead ZnO nanoparticles, w (g) of CeO_2 particles were introduced in the raw precursors. The purification steps for the composites are similar as for pure MF or MNF1 (section 2.2.1, chapter 2). Several composites with varying the 'w' amount of nanoparticles were synthesized following the procedure similar to described in the earlier section 5.2 and section 5.3 (chapter 5).

6.3 Results and discussion

6.3.1 TEM analysis

Figure 6.1 shows the TEM micrographs of as synthesized CeO_2 nanoparticles and its MOF composites. CeO_2 nanoparticles are in spherical shape in nature with size range of 3-5 nm (**Figure 6.1a**). Similar type of particle shape and size distribution was observed by Das et al. [3] **Figure 6.1b-6.1d** displays structural view of Cw-MF composites. One can observe that particles associated with high mass areas (darker areas) possess different shape and size i.e. needle or rod shaped. It leads to another observation that under acidic medium there are some microstructural changes occurred for CeO_2. To prove this point, CeO_2 was treated with HF, HNO_3 at 150 °C in hydrothermal condition in autoclave reactor. However, iron powder and BTC (raw materials for MIL-100(Fe) synthesis) were excluded in this process. The TEM image of these CeO_2-treated particles is shown in **Figure 6.1e**. these treated particles are in rod or needle shaped with the length of 20-50 nm and quite similar to observed in Cw-MF composites. The reason of that lies on dissolution of CeO_2 particles in acidic medium. Joret et al. [4] described that dissolution rate of CeO_2 in 7M HNO_3 at 111 °C is about 1.2 mg L^{-1} min^{-1}. Later, Lemont et al.[5] studied reduction-dissolution of CeO_2 particles in HCl solution.

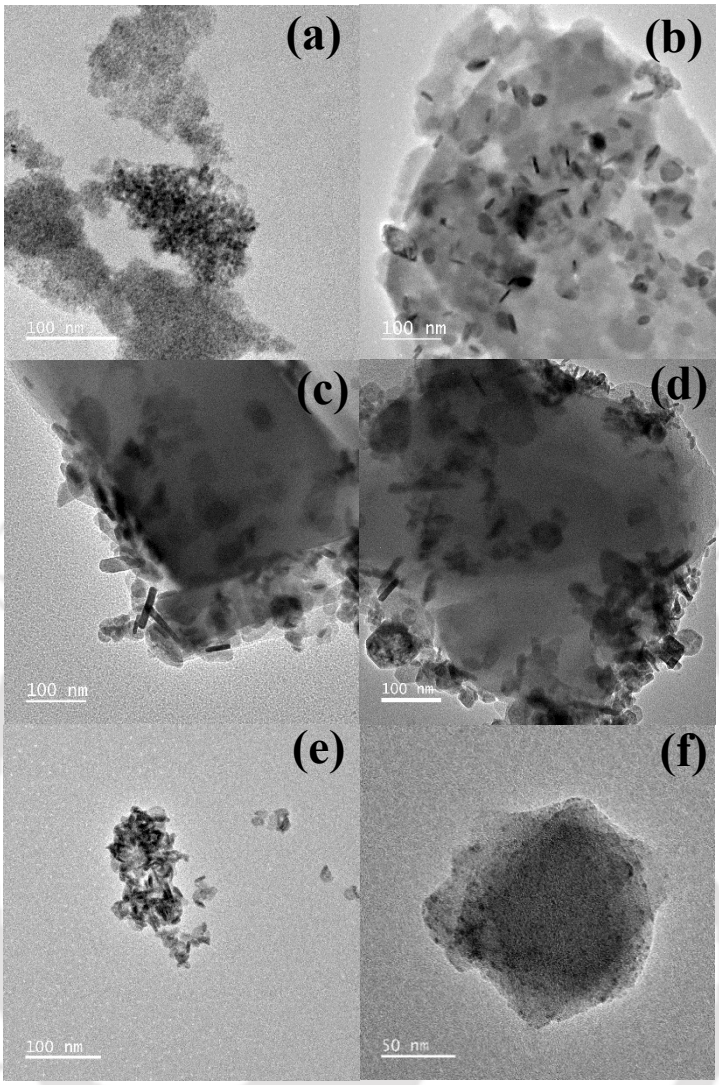

Figure 6.1: TEM micrographs of (a) CeO_2, (b) C100-MF, (c) C150-MF, (d) C300-MF (e) CeO2-treated, (f) C400-MNF1

In the present case of MOF synthesis HF and HNO_3 were used in reaction media. As HF is a hydrohalic acid like HCL, the dissolution-reduction of CeO_2 in MF precursors might be occurred and it can be represented by following reaction.[5]

$$CeO_2 + 4HF \rightarrow CeF_3 + 2H_2O + \frac{1}{2}F_2 \quad ---------(6.1)$$

So, the needle or rod shaped particles in **Figure 6.1b-6.1d** might be the appeared due to formation of cerium fluoride (CeF_3) and later further explained by XRD analysis. In other hand, in case of C500-MNF1 synthesis where no acid (HF or HNO_3) used in precursor, a well distribution of CeO_2 particles in MOF matrix is observed in **Figure 6.1f**.

6.3.2 XRD analysis

Figure 6.2 displays the XRD patterns for pure and CeO_2 promoted MIL-100(Fe) composites. Pure CeO_2 exhibits the peaks at peaks at 2θ of 28.5, 47.4 and 56.5° corresponds to the planes of (1 1 1), (2 2 0), (3 1 1) respectively. [2] In addition, some extra diffraction peaks are appeared in between 2θ of 25-65° for Cw-MF composites in **Figure 6.2a**. These peaks are appeared at 24.9, 27.8, 43.9, 45.1, 50.8, 52.9 and 64.8° resembles to (0 0 2), (1 1 1), (3 0 0), (1 1 3), (3 0 2), (2 2 1), (2 1 4) planes. These crystallographic planes are well matched with diffraction patterns of CeF_3 crystals (JCPDS card 08-0045).[6-8] Therefore, it is indeed clear that during Cw-MF composite synthesis CeO_2 nanoparticles are converted to CeF_3 and looked like as rod or needle shape. In case of C550-MNF1, no such extra peaks are observed relates to CeO_2 or CeF_3 in the **Figure 6.2b**.

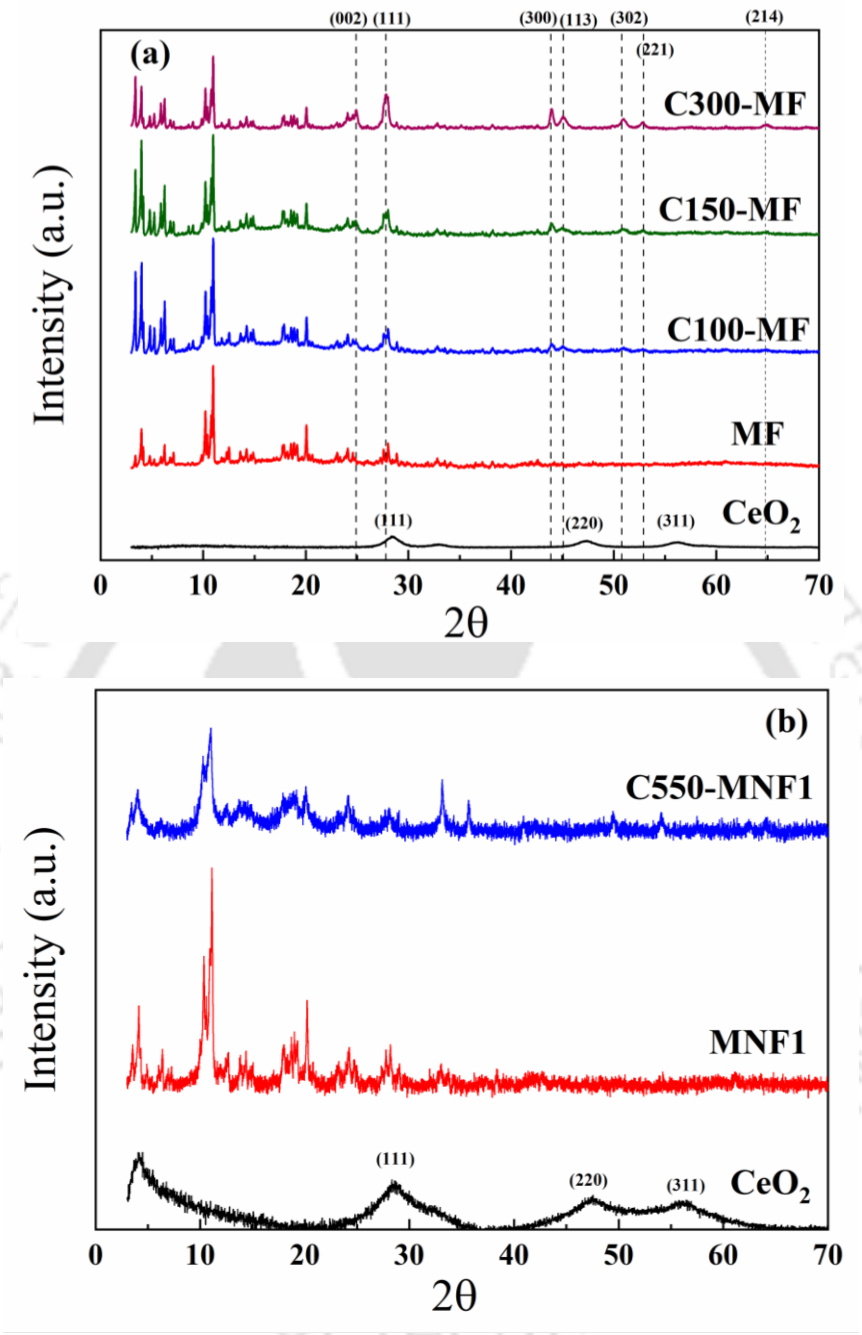

Figure 6.2: X-ray diffraction patterns of (a) CeO_2, MF and Cw-MF composites and (b) CeO_2, MNF1 and Cw-MNF1 composites

6.3.3 N_2 adsorption-desorption isotherms analysis

The adsorption-desorption isotherms of pure MOF and its nanocomposites are shown in **Figure 6.3**. Pure MF and Cw-MF composites exhibit type I isotherm. Similar observations were seen in case of Fe_3O_4 and ZnO based MF composites in section 4.3.5 and section 5.4.5 respectively. **Figure 6.3b** (inset) displays the isotherm of CeO_2 nanoparticles which relates the type IV nitrogen isotherm.[9] Isotherms of MNF1 and its composite C550-MNF1 (**Figure 6.3b**) also exhibit of type IV isotherm similar to Zw-MNF1 composites. The details of surface area and the total pore volume are given in **Table 6.1**.

Table 6.1: Surface area and pore volume details of the **Cw-MF** and **Cw-MNF1** composites

Sr. No.	Sample	Mass fraction CeO_2, *x*	Surface area ($m^2\ g^{-1}$)	Pore volume ($cm^3\ g^{-1}$)
1	MF	0.0	2054	1.08
2	MNF1	0.0	1845	1.2
3	CeO_2	1.0	5.6	0.02
4	C100-MF	0.08	1712	0.88
5	C150-MF	0.22	1701	0.86
6	C300-MF	0.42	1291	0.66
7	C550-MNF1	0.23	813	0.58

Pure CeO_2 has a surface area of 5.6 $m^2\ g^{-1}$ and pore volume of 0.02 $cm^3\ g^{-1}$ and it is relatively very low compare to pure MF and MNF1. The estimated surface area for CeO_2 obtained in this work is quite similar with earlier literature. [9]

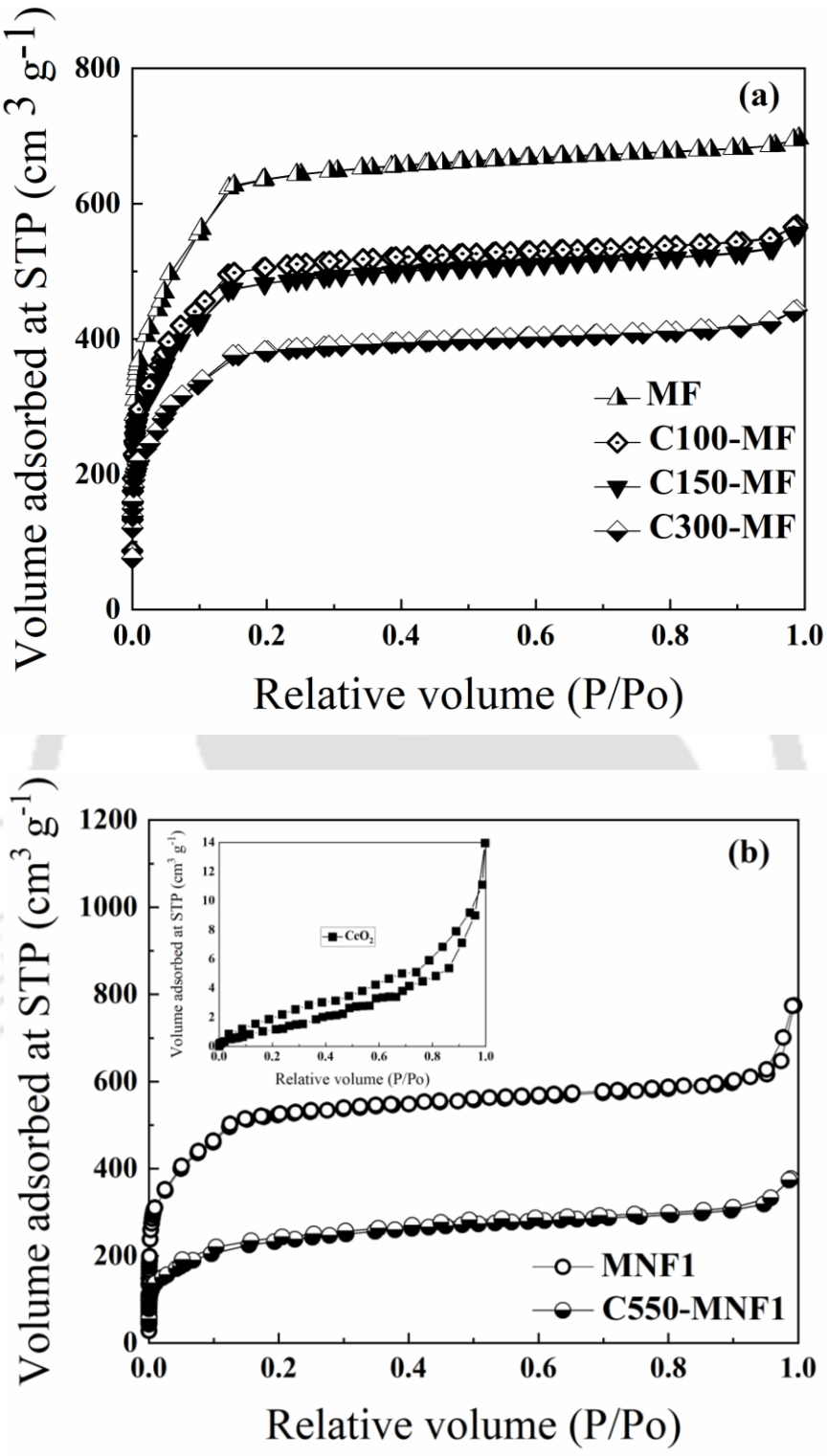

Figure 6.3: N_2 adsorption-desorption isotherms of (a) MF, Cw-MF and (b) CeO_2 (inset), MNF1, Cw-MNF1 composites

6.3.4 DOX loading

Pure CeO_2 has a loading capacity of 196 mg/g (in **Figure 6.4**) and it is in between the loading capacities of pure MF (107 mg/g) and MNF1 (234 mg/g) respectively. In case of the composites synthesis in HF route, the loading capacity is not much enhanced as compare to MF. The maximum loading capacity is 113 mg/g for C100-MF and almost equal to pure MF (107 mg/g); beyond that, the loading capacity decreases with increasing the nanoparticles. It is worth to mentioned that, the presence of CeF_3 (discussed in earlier section) instead of spherical CeO_2 in MF, might blocked the pores and thus decrease the DOX loading capacity.

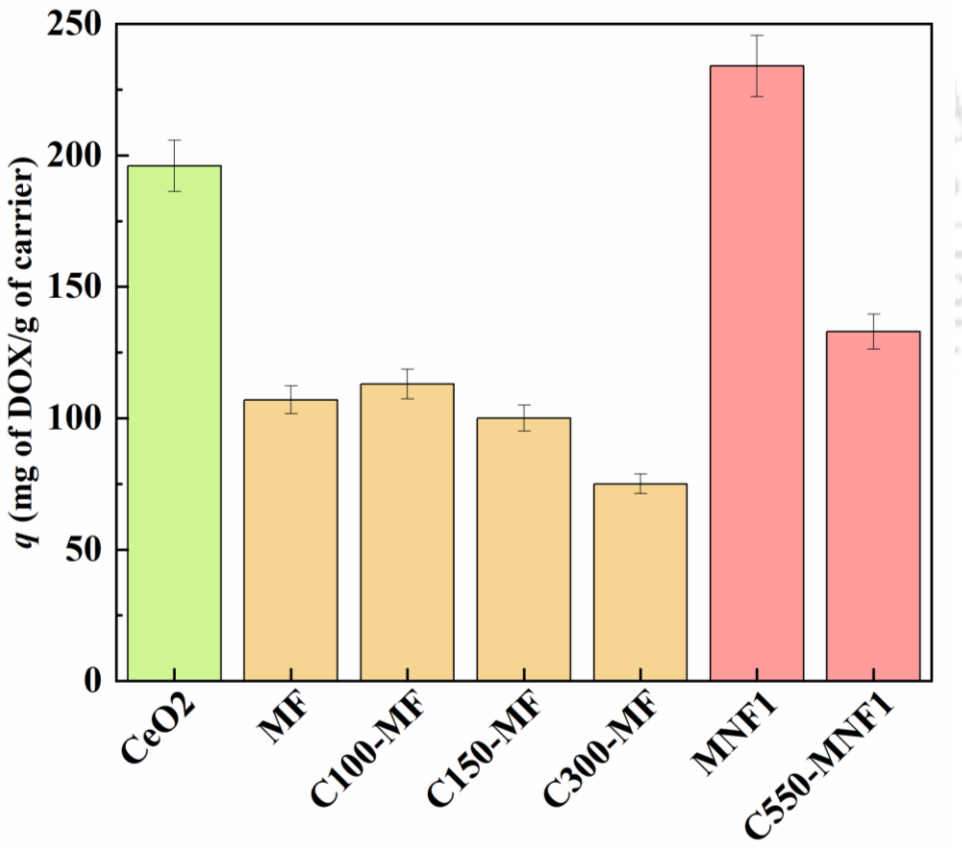

Figure 6.4: DOX loading of CeO_2, MF, MNF1 and its composites

In case of C550-MNF1, the loading capacity is dropped to133 mg/g as compare to pure MNF1(234 mg/g). Similar kind of results are observed for Fw-MNF1 and Zw-MNF1 composites as there seems to be no extra benefit of incorporating of nanoparticles in case of mesoporous MOFs.

6.3.5 DOX release study

The specific DOX release capacity of various carriers are given in **Figure 6.5**. The initial DOX release capacity from CeO_2 was too fast (so-called burst effect); almost 100 mg/g of DOX was released in first day. In addition, among the pure NPs, the initial DOX released capacity (for day 1) was found maximum for CeO_2 followed by ZnO (50 mg/g) and Fe_3O_4 (18 mg/g) respectively.

In case of Cw-MF composites, the specific DOX release patterns were more controlled compare to pCeO_2 NPs. The total amount of DOX released for C100-MF, C150-MF, and C300-MF were 51 mg/g, 55 mg/g and 49 mg/g respectively in a span of 20 days. These values are quite higher as compare to MF (37 mg/g in 20 days); although Cw-MF composites exhibit lower DOX loading capacity. The weaker interaction between DOX and the carriers (in presence of CeF_3) in the composites may responsible for this kind of release behaviour. On the other hand, DOX released from MNF1 and C550-MNF1 composite were ~69 mg/g and ~ 48 mg/g respectively. Composite C550-MNF1 have lower DOX loading capacity compare to MNF1 and thus, the released amount is lower. Similar kind of trends are observed for Z400-MNF1 in section 5.4.8.

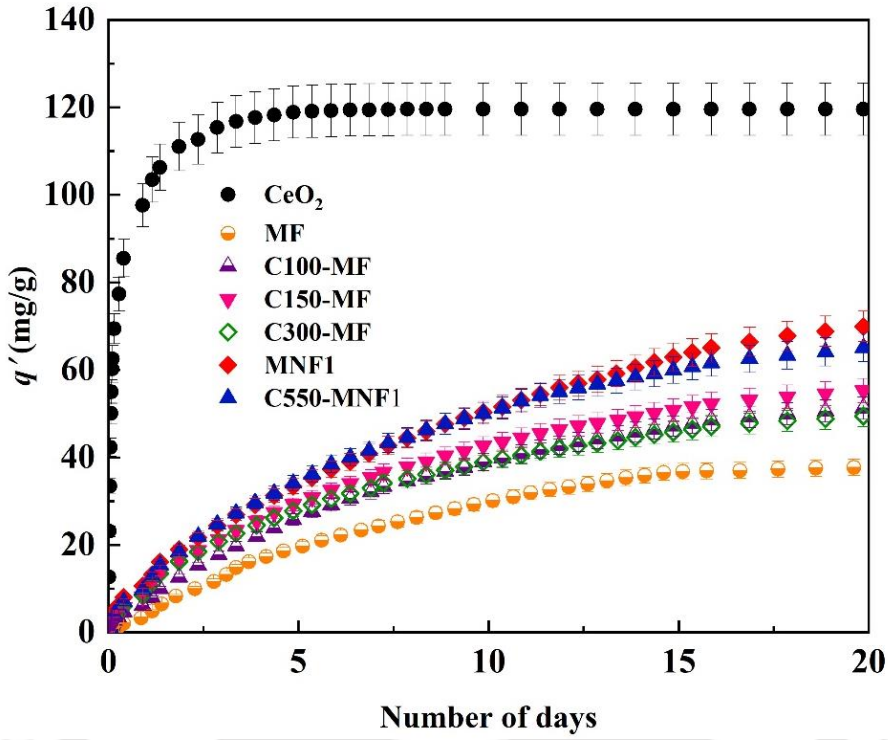

Figure 6.5: Specific drug released from CeO_2, MF, MNF1, Cw-MF and Cw-MNF1 composites

6.3.6. Comparison of DOX loading capacities between pure MIL-100 with different composites

The loading comparison between different synthesized carriers is shown in **Figure 6.6**. The DOX loading capacity for Z200-MF and F125-MF are quite similar and much higher than pure MF (107 mg/g). The incorporation of NPs (ZnO and Fe_3O_4) in the MIL-100 (in HF route) enhances the loading capacity. Both Z100-MNF1 and F125-MF have similar DOX loading capacity; although both have different contents of nanoparticles. DOX Loading is maximum for pure MNF1 owing to its higher mesopore volume.

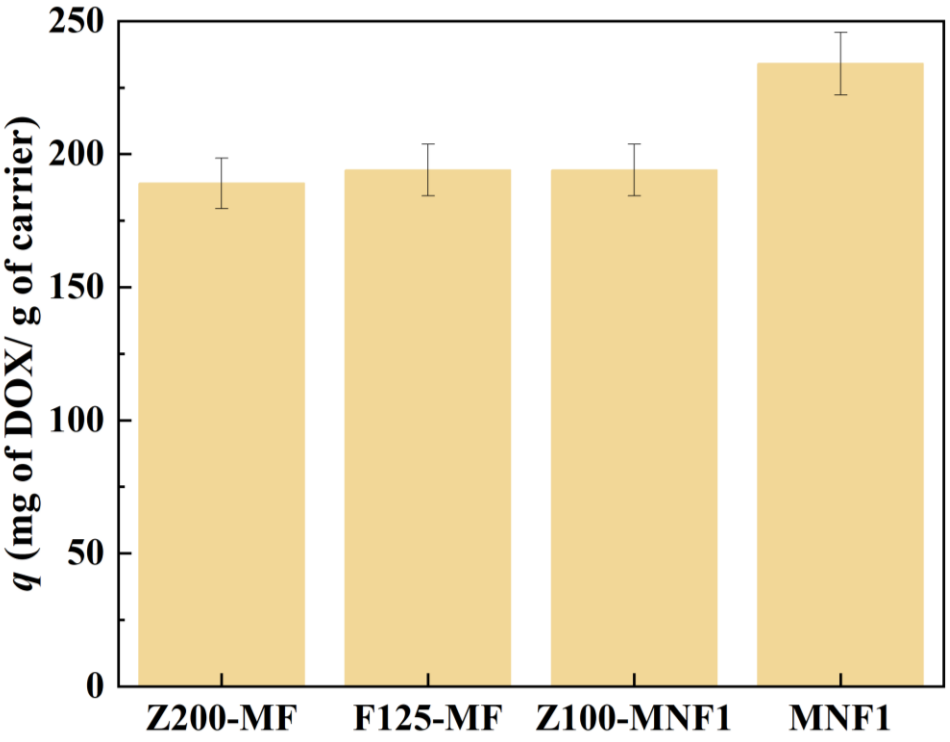

Figure 6.6: DOX loading comparison between Z200-MF, F125-MF, Z100-MNF1 and MNF1

6.3.7. Comparison of DOX release capacity between pure MIL-100 with different composites

In case of specific DOX release, maximum drug was released from MNF2 in first 20 days (77 mg/g) and followed by Z100-MF (67 mg/g) and C550-MNF1 (65 mg/g) respectively (**Figure 6.7**). The disordered and amorphous nature of MNF2 might have relatively weak interactions with DOX as compare to others carriers; thus ~48% of loaded DOX was released in first 20 days. In other hand, the drug released rate was slightly slow (51 mg/g) for F50-MF among the other carriers (**Figure 6.7**). The DOX loading capacity of F50-MF is significantly higher compare to others. Thus, the strong interactions between DOX with the carrier might be responsible for such slow release.

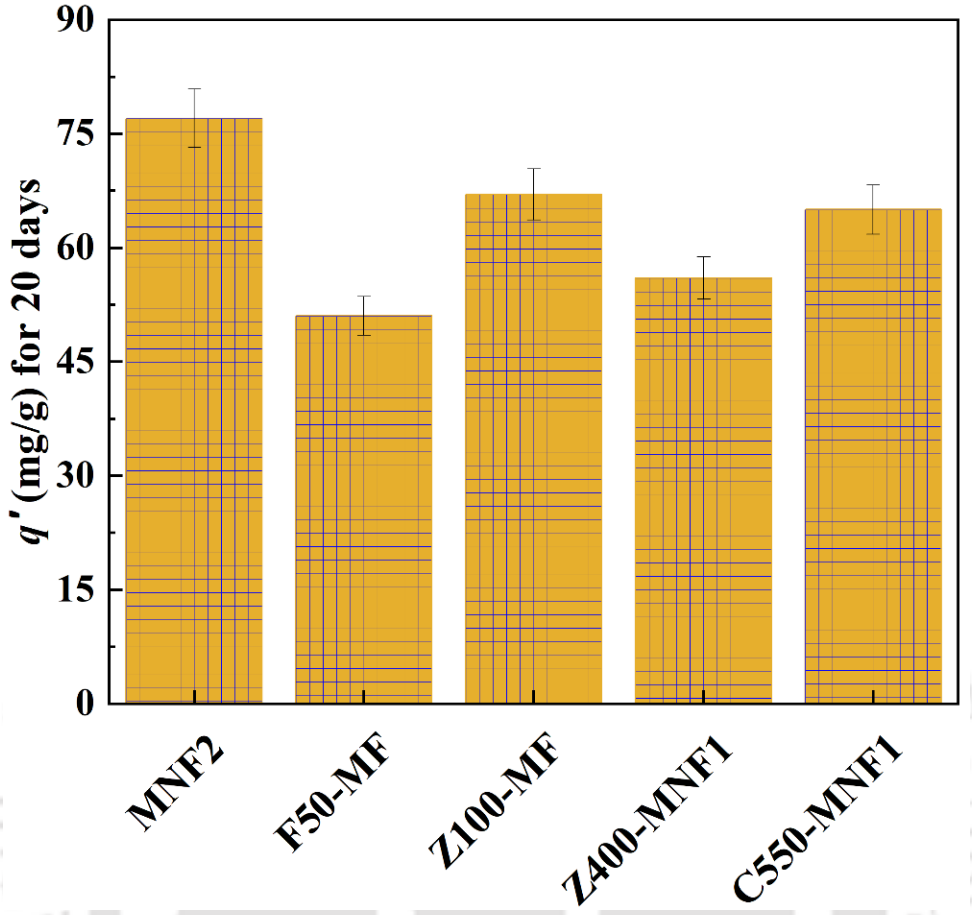

Figure 6.7: Comparison of specific release between MNF2, F50-MF, Z100-MF, Z400-MNF1 and C550-MNF1 (for 20 days)

6.3.8. Comparison with DOX loading content by different synthesized carriers with the literature

In this work, MIL-100(Fe) MOF and its various nanocomposites were synthesized for loading of anticancer drug doxorubicin hydrochloride (DOX). The loading performance of these carriers are compared with the literature and is shown in **Table 6.2**. The **Table 6.2** concludes

that the carriers synthesized in present study represents an improved choice compare to other reported materials.

Table 6.2: Comparison of DOX loading content of different carriers reported in literature with present study

Sr. No.	**Carriers**	**DOX Loading (mg/g)**	**Ref.**
01	MIL-100 (MOFs)	91	[10]
02	ZIF-8 (MOFs)	49	[11]
03	Phosphate-terminated magnetic mesoporous nanoparticles (pMMSNs)	69	[12]
04	Mesoporous silica coated superparamagnetic manganese ferrite ($MnFe_2O_4$)	113	[13]
05	Cisplatin crosslinked-NPs (Dex-SA-DOX-CISPLATIN)	139	[14]
06	ZnO-DOX@ZIF-8	112	[15]
07	Hyaluronic acid coated silica- supported mesoporous titania (MTNst)	183	[16]
08	BSA/DOX@ZIF-8	100	[17]
09	MIL-100 (MNF1)	234	Present study
10	MIL-100 (MNF2)	161	Present study
11	Fe3O4@MIL-100 (F125-MF)	194	Present study
12	ZnO@MIL-100 (Z200-MF)	189	Present study

6.4 Summary

In this chapter, an attempt was made to synthesis CeO_2@MIL-100(Fe) composites by HF and without HF route. In the presence of HF, spherical CeO_2 nanoparticles converted to CeF_3. It was confirmed by TEM and XRD analysis. Thus, DOX loading capacity was not further improved as compare to pure MOF or nanoparticles. Also, loading capacity was not enhanced in case of composite synthesis with mesoporous MNF1.In addition, loading performance of the different carriers are compared with the literature. It can be envisaged that the result of the current work relates well with the reported works.

References

1. E. Alpaslan, H. Yazici, N. H. Golshan, K. S. Ziemer and T. J. Webster, *ACS Biomater. Sci. Eng*., 2015, **1**, 1096-1103.
2. J. M. Perez, A. Asati, S. Nath and C. Kaittanis, *Small*, 2008, **4**, 552-556.
3. J. Das, Y-J. Choi, J. W. Han, A. M. M. T. Reza and J-H. Kim, *Sci. Rep*., 2017, **7**, 9513.
4. L. Joret, G. Cote and D. Bauer, *Hydrometallurgy*, 1997, **45**, 1-12.
5. F. Lemont and A. Barbier, *Hydrometallurgy*, 2019, **183**,193-198.
6. Z. L. Wang, Z. W. Quan, P. Y. Jia, C. K. Lin, Y. Luo, Y. Chen, J. Fang, W. Zhou, C. J. O'Connor and J. Lin, *Chem. Mater*.,2006, **18**, 2030-2037.
7. J. d. Castillo, A. C. Yanes, J. Méndez-Ramos, J. J. Velázquez and V. D. Rodríguez, *J. Sol-Gel Sci. Technol*., 2011, **60**, 170-176.
8. C. Li, F. Li, T. Li, T. Bai, L. Wang, Z. Shi and S. Feng, *Dalton Trans*., 2012, **41**, 4890-4895.
9. S. Kandasamy, B. Zhang, Z. He, H. Chen, H. Feng, Q. Wang, B. Wang, V. Ashokkumar, S. Siva, N. Bhuvanendran and M. Krishnamoorthi, *Energy*, 2020, **190**,116236.
10. P. Horcajada, T.Chalati, C. Serre, B. Gillet, C. Sebrie, T.Baati, J. Eubank, D.Heurtaux, P. Clayette, C. Kreuz, J. Chang, Y. Hwang, V. Marsaud, P. Bories, L. Cynober, S. Gil, G. Férey, P. Couvreur and R. Gref, *Nat. Mater*., 2010, **9**, 172-178.
11. I. B. Vasconcelos, T. G. da Silva, G. C. G. Militão, T. A. Soares, N. M. Rodrigues, M. O. Rodrigues, N. B. da Costa Jr., R. O. Freiree and S. A. Junior, *RSC Adv*., 2012, **2**, 9437-9442.
12. E. Che, L. Wan, Y. Zhang, Q. Zhao, X. Han, J. Li, J. Liu and S. Wang, *Asian J. Pharm. Sci.*, 2014, **9**, 317-323.

13. B. Sahoo, K. S. P. Devi, S. Dutta, T. K. Maiti, P. Pramanik and D. Dhara, *J. Colloid Interface Sci*., 2014, **431**, 31-41.

14. M. Li, Z. Tang, S. Lv, W. Song, H. Hong, X. Jing, Y. Zhang and X. Chen, *Biomaterials*, 2014, **35**, 3851-3864.

15. C. Zheng, Y. Wang, S. Z. F. Phua, W. Q. Lim and Y. Zhao, *ACS Biomater. Sci. Eng*., 2017, **3**, 2223-2229.

16. B. Gupta, B.K. Poudel, H. B. Ruttala, S. Regmi, S. Pathak, M. Gautam, S. G. Jin, J-H Jeong, H-G. Choi, S. K. Ku, C. S. Yong and J. O. Kim, *Acta Biomater*., 2018, **80**, 364-377.

17. Z. Liang, Z. Yang, H. Yuan, C. Wang, J. Qi, K. Liu, R. Cao and H. Zheng, *Dalton Trans*., 2018, **47**, 10223-10228.

Chapter 7

Conclusion and future scope of work

Chapter 7

Conclusions and Future scope of work

This chapter is divided into two sections. First section summarizes the main conclusions of the various chapters of this thesis and provides the inferences drawn from various work presented in this thesis. Second section is about suggestions towards the future scope.

7.1 Conclusion

The thesis is organized in seven chapters. **Chapter 1** addresses the state of the art, motivation, possible scope, and objectives of present work. The synthesis and characterization techniques of different MOFs and nanoparticles are described in **chapter 2**. The major conclusion from other chapters are given below.

Chapter 3

1. MIL-100 was successfully synthesized hydrothermally with and without HF. HF, a mineralizing agent plays an important role to develop crystal size and shape, surface area, mesopores volume, morphology in MIL-100(Fe); without HF, more mesopores are generated. The DOX loading capacity was maximum (234 mg/g of carrier) in case of HF free MIL-100(Fe) and it was 2.2-fold higher loading than MIL-100 prepared by conventional HF route.
2. In addition, both DOX loading and release patterns are significantly affected by the mesoporosity in case of MIL-100(Fe). Specific DOX loading capacity increases with

increase in mesopore volume; thus MIL-100(Fe) without HF (in case of MNF1) have the highest loading capacity.

3. In both microporous, MIL-00 (MF**)** and ordered mesoporous MIL-100 (MNF1) significant interactions of the DOX might occur with the carrier and hence the percentage of the drug released in lower. However, in disordered and amorphous MIL-100 (MNF2) these interactions are significantly lesser and allow for easy release of the drug.

Chapter 4

1. In case of nanoparticles MOF composites, the presence of nanoparticles in the MIL-100 frameworks were confirmed by the FETEM analysis. The presence of nanoparticles in MOF structure did not alter the framework property as characterized by other techniques.
2. The existence of Fe_3O_4 particles in MIL-100 enhanced the magnetic property; saturation magnetization of 12.2 emu/g was found for Fe_3O_4@MIL-100(Fe) composite with 0.37 mass fraction of nanoparticles.
3. The DOX loading capacity was increased with rise in nanoparticle content in the composites. But, at higher concentration of Fe_3O_4 in the composites, the loading capacity slightly decreases possibly due to agglomerated nanoparticles blocking the pore openings of the MOF.
4. The maximum DOX loading was found 194 mg/g (F125-MF) as opposed to 110 and 107 mg/g for pure Fe_3O_4 and MIL-100(Fe).

5. The drug release patterns of all the composites were well controlled and sustained for over 20 days without premature release of DOX; the incorporation of Fe_3O_4 nanoparticles into the composites did not significantly alter the release profiles but the total released amount of DOX increased due to their higher loading capacity.

Chapter 5

1. ZnO incorporated porous iron carboxylate MIL-100(Fe) composites (Zw-MF and Zw-MNF1) were successfully prepared by one pot *in situ* crystallization technique.
2. The DOX loading capacity on pure MF, MNF1 and ZnO were 107, 234 and 253 mg/g respectively. This value increases upon addition of ZnO to MF and it was observed that Z200-MF with about 29% ZnO, has a loading capacity of 189 mg/g; at higher ZnO content in the composites, the loading capacity decreases, possibly due to blocking of access to the adsorption sites by the nanoparticles. On the other hand, the loading capacity decreases, upon addition of even 4 wt% ZnO to the mesoporous MNF1; there seems to be no additional advantage of incorporating nanoparticles, if the MOF is already mesoporous.
3. In addition, the DOX loading capacity ZnO nanoparticles (253 mg/g) more than two times that of Fe_3O_4 nanoparticles. However, the maximum DOX loading of composites formed from both these nanoparticles is almost equal, indicating that their presence changes the morphology of MIL-100(Fe), which in turn affects adsorption of DOX. The chemical nature may of the nanoparticles themselves may have little role in this enhancement. The study provides interesting insights into advantage of addition of

nanoparticles to MIL-100(Fe) and its effect on the DOX loading capacity and subsequent release.

4. The drug release patterns of the composites do not exhibit the so-called burst effect and were well controlled for over 25 days. The specific drug release of Z200-MF is slower than that of Z100-MF due to stronger interaction of DOX with the framework.

Chapter 6

1. CeO_2@MIL-100(Fe) composites were synthesized by two routes viz. a conventional HF route (in the presence of HF as crystallizing agent) and another in the absence of HF.
2. In case of HF synthesis route, the CeO_2 was transformed to CeF_3 and it was confirmed by FETEM, XRD analysis. The resultant MF and its composites significantly differ in DOX loading capacity and release rates.
3. The DOX loading capacity of pure CeO_2 was 196 mg/g.
4. In case of Cw-MF composites the maximum DOX loading was observed for C100-MF (113 mg/g) with about 8% of CeO_2 in the MOF precursor. At higher CeO_2 concentration, the loading capacity decreased, perhaps due to blocking of preferential adsorption sites by rod or needle-shaped CeF_3.
5. In the other hand, synthesis by HF free route, structural conversion of CeO_2 to CeF_3 was not seen much and it was further confirmed by different characterization techniques. Although, composite prepared by this method did not provide any additional advantage in DOX loading as MNF1 is mesoporous.
6. The DOX loading capacity of different carriers from this study are comparable with the reported literatures.

7.2 Future scope of work

Few research areas for future work are presented as follows:

1. In the present study, iron based MIL-100(Fe) metal-organic framework was used anticancer drug delivery. Apart from this MOF, other MOFs like MIL-101(Fe), MIL-127(Fe), PCN-333(Fe) can be used and developed for doxorubicin delivery.
2. In this work, doxorubicin hydrochloride (DOX) is used as a model drug. The synthesized carriers can be tested for other commercially available anticancer drugs like Cisplatin, Docetaxel, 5-Fluorouracil, Epirubicin, Curcumin, Paclitaxel etc.
3. In this study, DOX is loaded in to pure MIL-100(Fe) and its various nanoparticle based composites. Further, these DOX loaded carriers can be encapsulated by a suitable lipid layer or a polymer coating to improve chemical and colloidal stability for administration.
4. In vitro cytotoxicity study of the prepared carriers can be explored in the various cells like MCF-7 human breast carcinoma and HeLa cells.
5. Fe_3O_4@MIL-100(Fe) and ZnO@MIL-100(Fe) composites can be further explored in the field of removal of organophosphates, other toxic substances in water and dye degradation under visible and UV light irradiation.
6. The fate and renal clearance of various nanoparticle-MOF composites can be further explored.
7. Study and development of metal-organic frameworks based microrobots for the application in the field of environmental remediation, targeted drug delivery and nanosurgery etc.

Appendix A: Calibration Curves for UV-Vis spectroscopy

DOX concentrations in different media (water and PBS) are determined by first preparing a calibration curve in UV-Visible spectrophotometer. Calibration curves are prepared for different concentrations of DOX in water and PBS at the wavelength of 480 nm.

Figure A1 presents the obtained calibration curve for DOX loading experiments. It can be observed that the absorbance varied linearly with variation in DOX concentration. Similarly, for release experiments, a different calibration curve (Figure A2) is prepared in PBS solution (release media, pH 7.4).

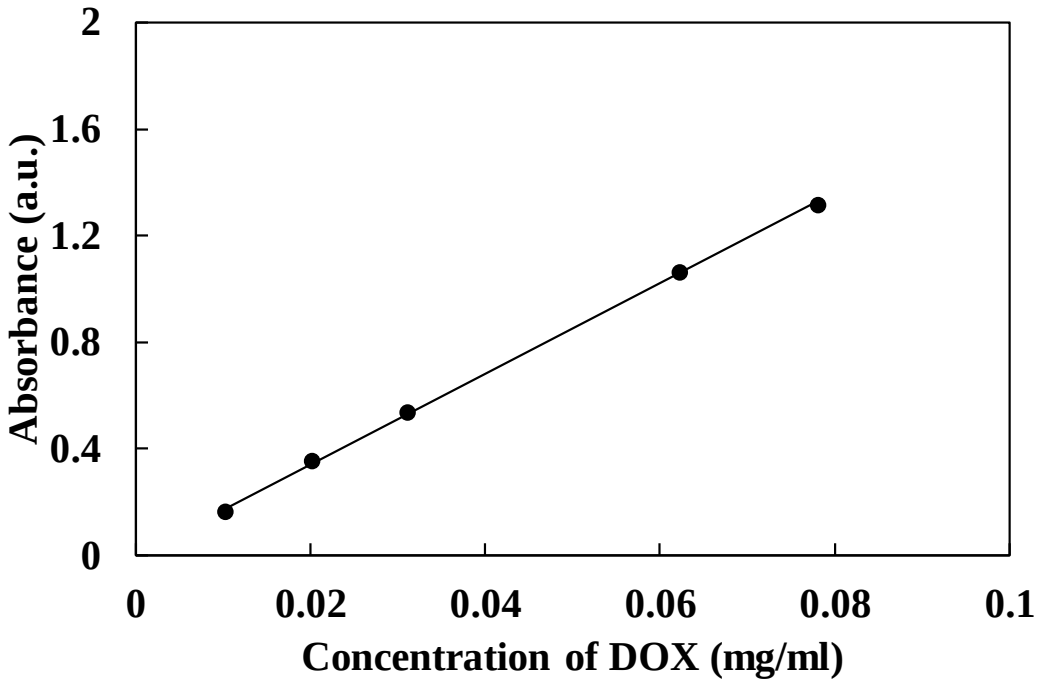

Figure A1: DOX calibration curve in water

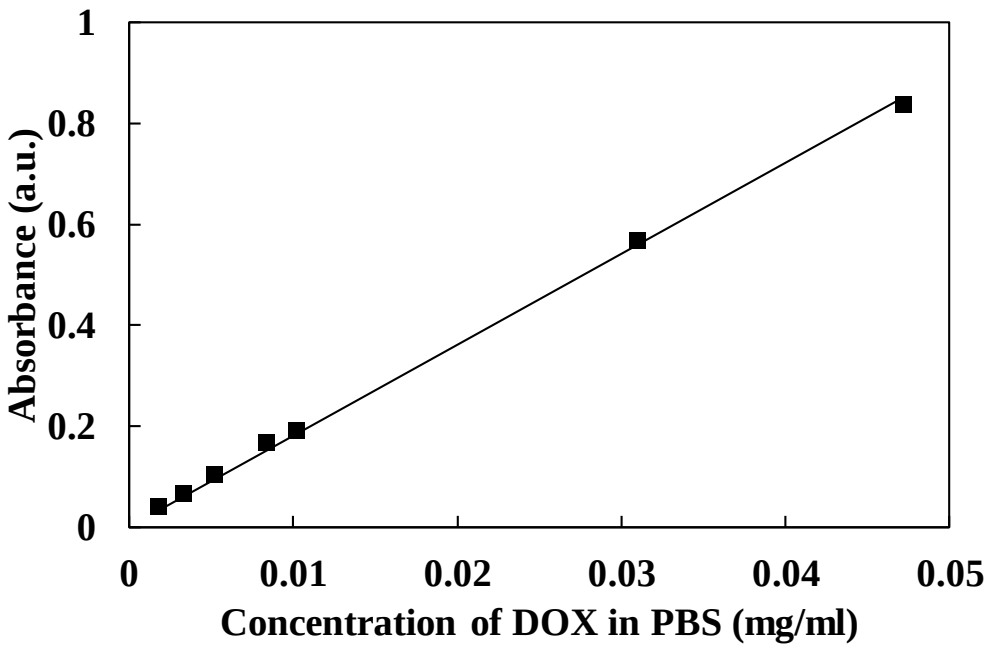

Figure A2: DOX calibration curve in PBS (pH 7.4)

Appendix B: Error Analysis

Error analysis is necessary as it infers to the accuracy of calculations and reliability of reported data. Although experiments are carried out with utmost care, yet due to measurement errors, the data obtained or calculated may not be accurate. There are different types of errors viz. absolute error, relative error, systematic error and random error. Absolute error refers to the difference between the measured or inferred value of a quantity and its actual value. Relative error is the ratio of the error to the best value of the quantity. Systematic errors are the results of faulty assumptions and measuring techniques whereas random errors result from variation in the precision of measuring parameters and the slight variations that occur in successive measurements under nearly identical conditions.

Error measurements for loading and release experiments

Error calculations were also done for the DOX concentration in each loading and release experiments. An error of ± 5% was taken into consideration for each data.